Optical Antennas: Nanoscale Radiation Engineering and Enhanced Light-Matter Interaction

Von der Fakultät Mathematik und Physik
der Universität Stuttgart zur Erlangung der Würde
eines Doktors der Naturwissenschaften (Dr. rer. nat.)
genehmigte Abhandlung

vorgelegt von

Daniel Drégely
aus Regensburg

Hauptberichter:	Prof. Dr. H. Giessen
Mitberichter:	Prof. Dr. P. Michler
	Prof. Dr. C. Sönnichsen
Tag der mündlichen Prüfung:	13.02.2014

4. Physikalisches Institut der Universität Stuttgart
2013

Daniel Drégely: *Optical Antennas: Nanoscale Radiation Engineering and Enhanced Light-Matter Interaction*, 2013

To my family.

ABSTRACT

This thesis studies optical nanoantennas from the near-infrared to the mid-infrared region. Nanoantennas are key components in the emerging field of nanophotonics. They exhibit strong interaction with the optical radiation field because of the excitation of plasmonic resonance, which leads to high near-field intensities, deep subwavelength energy confinement, and strongly enhanced radiation. This thesis addresses the key questions of how these properties can be used to enhance light-matter interaction and how to engineer optical radiation on the nanoscale by tailoring the antenna geometries.

We demonstrate that radiofrequency antenna geometries can be scaled to the optical regime by experimental realization of optical Yagi-Uda nanoantennas. A Yagi-Uda antenna has unidirectional radiation properties, which means light incident from one direction is efficiently confined to a deep subwavelength volume while that incident from the other directions is not. We assess the near-field of a planar plasmonic Yagi-Uda nanoantenna with scanning near-field optical microscopy. We record phase and amplitude in order to identify the optical modes and demonstrate directional receiving of light at $\lambda = 1064$ nm. We then fabricate three-dimensional Yagi-Uda nanoantenna arrays, which exhibit very high directivities out of the substrate plane. Since the antenna array is completely embedded in a dielectric matrix, scanning near-field optical microscopy cannot be used for optical characterization. Instead, we use Fourier transform infrared spectroscopy combined with near-field simulations to study the directional antenna array, which receives out of plane radiation at $\lambda = 1.5$ μm. Furthermore, we show by simulation how to use our nanoantenna array for beamsteering.

In order to solve the challenge of mapping the near-field intensity of three-dimensional nanoantennas, we develop a novel field-mapping technique based on surface enhanced vibrational spectroscopy. The high

near-field intensities generated by plasmonic structures are used to enhance vibrational transitions in molecules, which occur in the infrared spectral region. We position molecules at specific locations close to plasmonic antennas, which are designed to be in resonance with the vibrational band around 4.4 μm, and measure the extinction spectrum of the coupled antenna-molecule system. We observe that the measured vibrational signal scales with the local near-field intensity, which is applied to map the plasmonic near-field intensity. This method maps the field in the infrared region and provides subwavelength resolution. We finally demonstrate that our technique is able to assess near-field intensities of plasmonic structures with three-dimensional complexity.

Furthermore, we demonstrate for the first time optical power transfer by nanoantennas. We realize in experiment a wireless point-to-point link between a transmitter and a receiver nanoantenna at $\lambda = 785$ nm. By fluorescence microscopy, we measure the radiation pattern and show that the transmission of the wireless link follows the inverse square power law of free space propagation. This enables low-loss power transfer across large distances at the nanoscale. In addition, we experimentally demonstrate beamsteering over a broad angular range by adjusting the wavefront of the incident optical field on the transmitter. In our experiment we show that the transmitter can address different receivers by effective beamsteering. The low-loss power transfer combined with the beamsteering functionality comprises a significant advancement compared to state-of-the-art waveguide connections. Our reconfigurable nanoantenna link may lead to technology breakthrough in information transfer between nanoscale devices and objects.

ZUSAMMENFASSUNG

Die vorliegende Arbeit befasst sich mit optischen Nanoantennen im nahinfraroten und im mittel-infraroten Spektralbereich. Nanoantennen sind Schlüsselkomponenten im Forschungsgebiet der Nanophotonik. Aufgrund der Anregung von plasmonischen Resonanzen zeigen sie eine starke

Wechselwirkung mit dem optischen Strahlungsfeld. Diese Anregung führt zu hohen Nahfeld-Intensitäten, Energiebündelung in den Subwellenlängenbereich und stark verstärkten Abstrahlungsintensitäten. Die vorliegende Arbeit befasst sich mit der Kernfrage, wie sich diese Eigenschaften durch geeignete Antennengeometrien nutzbar machen lassen, um die Licht-Materie-Wechselwirkung zu verstärken und die Strahlungscharakteristiken auf der Nanometer-Skala zu kontrollieren.

Zunächst zeigen wir anhand einer planaren optischen Yagi-Uda Nanoantenne, dass sich Antennengeometrien und deren Eigenschaften aus dem Radiofrequenzbereich in den optischen Frequenzbereich skalieren lassen. Eine Yagi-Uda Antenne hat unidirektionale Strahlungseigenschaften. Dies bedeutet, dass auf die Antenne treffende Strahlung aus einer bestimmten Vorzugsrichtung effizient in den Subwellenlängenbereich fokussiert wird, während diese Effizienz für Strahlung aus anderen Richtungen nicht erreicht wird. Wir messen die Nahfeldverteilung von planaren plasmonischen Yagi-Uda Nanoantennen mit optischer Rasternahfeldmikroskopie. Durch die Messung von Phase und Amplitude der Nahfeldverteilung werden zum einen die optischen Moden identifiziert und zum anderen wird das direktionale Empfangen bei einer Wellenlänge von $\lambda = 1064$ nm gezeigt. Danach zeigen wir mit dreidimensionalen Yagi-Uda Nanoantennenfeldern sehr hohe direktive Empfangs- und Sendeeigenschaften entlang der Substratnormalen. Da das Antennenfeld komplett in einer dielektrischen Umgebung eingebettet ist, kann die optische Charakterisierung nicht mit optischer Rasternahfeldmikroskopie erfolgen. Wir verwenden daher Fourier-Transform-Infrarotspektroskopie in Kombination mit Nahfeld-Simulationen, um die direktionalen Empfangseigenschaften von einfallender Strahlung entlang der Substratnormalen bei einer Wellenlänge von $\lambda = 1.5$ µm nachzuweisen. Wir zeigen außerdem, wie die Abstrahlungsrichtung mit unserem Nanoantennenfeld kontrolliert werden kann.

Um elektrische Nahfelder von dreidimensionalen Nanoantennen-Strukturen zu messen, entwickeln wir eine neue Methode, die auf oberflächenverstärkter Vibrationsspektroskopie beruht. Die von Nanoantennen generierten hohen Nahfeldintensitäten werden verwendet, um Vibrati-

onsübergänge in Molekülen, die im Infraroten stattfinden, zu verstärken. Dazu positionieren wir Moleküle in der Umgebung von plasmonischen Antennen, die in Resonanz mit dem Vibrationsübergang bei 4.4 μm sind, und messen das Extinktionsspektrum des gekoppelten Systems. Wir beobachten, dass das gemessene Vibrationssignal mit der lokalen Nahfeldintensität skaliert, und vermessen durch nanometergenaue Positionierung der Moleküle die plasmonische Nahfeldintensität. Diese Methode hat sub-wellenlängen Auflösung und ermöglicht es Nahfeldintensitäten im infraroten Spektralbereich zu bestimmen. Wir zeigen schließlich, dass unsere Technik es ermöglicht, Nahfeldintensitäten von dreidimensionalen plasmonischen Nanostrukturen zu vermessen.

Schließlich zeigen wir zum ersten Mal Signalübertragung bei optischen Frequenzen mit plasmonischen Nanoantennen. Wir realisieren eine optische Punkt-zu-Punkt Richtfunkstrecke zwischen einer Übertragungs- und einer Empfangsantenne bei einer Wellenlänge von $\lambda = 785$ nm. Mit Fluoreszenz-Mikroskopie messen wir die direktive Abstrahlungscharakteristik der Übertragungsantenne und zeigen im Speziellen, dass die Übertragungseffizienz zwischen beiden Nanoantennen identisch mit der Übertragungseffizienz der Wellenausbreitung im freien Raum ist. Diese verlustarme Signalübertragung ermöglicht es über große Distanzen auf der Nanometer-Skala zu kommunizieren. Außerdem zeigen wir experimentell, wie die Abstrahlungsrichtung durch Phasenkontrolle über einen großen Bereich eingestellt werden kann. Dadurch senden wir ein optisches Signal zu verschiedenen Empfangsantennen. Diese Flexibilität in Kombination mit der verlustarmen Signalübertragung ist ein entscheidender Vorteil im Vergleich zu optischen Wellenleiter-Verbindungen. Unsere rekonfigurierbare Richtfunkstrecke basierend auf plasmonischen Nanoantennen eröffnet neue Möglichkeiten in der Informationsübertragung mit optischen Frequenzen zu und von nanometergroßen Objekten.

PUBLICATIONS

FULL LIST OF PUBLICATIONS

IN SCIENTIFIC JOURNALS:

[1] M. Hentschel, D. Dregely, R. Vogelgesang, H. Giessen, and N. Liu, *Plasmonic oligomers: the role of individual particles in collective behavior*, ACS Nano **5**, 2042-2050 (2011).

[2] D. Dregely, R. Taubert, J. Dorfmüller, R. Vogelgesang, K. Kern, and H. Giessen, *3D optical Yagi-Uda nanoantenna array*, Nature Communications **2**, 267 (2011).

[3] R. Ameling, D. Dregely, and H. Giessen, *Strong coupling of localized and surface plasmons to microcavity modes*, Optics Letters **36**, 2218-2220 (2011).

[4] J. Dorfmüller, D. Dregely, M. Esslinger, W. Khunsin, R. Vogelgesang, K. Kern, and H. Giessen, *Near-field dynamics of optical Yagi-Uda nanoantennas*, Nano Letters **11**, 2819-2824 (2011).

[5] A. Tittl, P. Mai, R. Taubert, D. Dregely, N. Liu, and H. Giessen, *Palladium-based plasmonic perfect absorber in the visible wavelength range and its application to hydrogen sensing*, Nano Letters **11**, 4366-4369 (2011).

[6] D. Dregely, M. Hentschel, and H. Giessen, *Excitation and tuning of higher-order Fano resonances in plasmonic oligomer clusters*, ACS Nano **5**, 8202-8211 (2011).

[7] R. Taubert, D. Dregely, T. Stroucken, A. Christ, and H. Giessen, *Octave-wide photonic band gap in three-dimensional plasmonic Bragg structures and limitations of radiative coupling*, Nature Communications **3**, 691 (2012).

[8] D. Dregely, K. Lindfors, J. Dorfmüller, M. Hentschel, M. Becker, J. Wrachtrup, M. Lippitz, R. Vogelgesang, and H. Giessen, *Plasmonic antennas, positioning, and coupling of individual quantum systems*, Physica Status Solidi (b) **249**, 666-677 (2012).

[9] S. Lobanov, T. Weiss, D. Dregely, H. Giessen, N. Gippius, and S. Tikhodeev, *Emission properties of an oscillating point dipole from a gold Yagi-Uda nanoantenna array*, Physical Review B **85**, 155137 (2012).

[10] M. Schäferling, D. Dregely, M. Hentschel, and H. Giessen, *Tailoring enhanced optical chirality: design principles for chiral plasmonic nanostructures*, Physical Review X **2**, 031010 (2012).

[11] K. Beha, H. Fedder, M. Wolfer, M. C. Becker, P. Siyushev, M. Jamali, A. Batalov, C. Hinz, J. Hees, L. Kirste, H. Obloh, E. Gheeraert, B. Naydenov, I. Jakobi, F. Dolde, S. Pezzagna, D. Twittchen, M. Markham, D. Dregely, H. Giessen, J. Meijer, F. Jelezko, C. E. Nebel, R. Bratschitsch, A. Leitenstorfer, and J. Wrachtrup, *Diamond nanophotonics*, Beilstein Journal of Nanotechnology **3**, 895-908 (2012).

[12] J. Y. Chin, T. Steinle, T. Wehlus, D. Dregely, T. Weiss, V. I. Belotelov, B. Stritzker, and H. Giessen, *Nonreciprocal plasmonics enables giant enhancement of thin-film Faraday rotation*, Nature Communications **4**, 1599 (2013).

[13] D. Dregely, F. Neubrech, H. Duan, and H. Giessen, *Vibrational near-field mapping of planar and buried three-dimensional plasmonic nanostructures*, Nature Communications **4**, 2237 (2013).

[14] L. E. Kreilkamp, V. I. Belotelov, J. Y. Chin, S. Neutzner, D. Dregely, T. Wehlus, I. A. Akimov, M. Bayer, B. Stritzker, and H. Giessen, *Waveguide-plasmon polaritons enhance transverse magneto-optical Kerr effect*, Physical Review X **3**, 041019 (2013).

[15] D. Dregely, K. Lindfors, M. Lippitz, and H. Giessen, *Optical wireless nanoantenna link*, submitted (2014).

BOOK CHAPTER:

[1] D. Dregely, J. Dorfmüller, M. Hentschel, and H. Giessen, *Fabrication, characterization and applications of optical antenna arrays*, in Optical Antennas, M. Agio and A. Alù eds. (Cambridge University Press, 2013), pp. 256-276.

TALKS & POSTERS (OWN CONTRIBUTIONS):

Invited

[1] D. Dregely, *Optical antennas for radiation engineering at the nanoscale and enhanced light-matter interaction*, Seminar of the Data Storage Institute (A*STAR), Singapore (2013).

Contributed at international conferences

[1] D. Dregely, R. Taubert, and H. Giessen, *3D optical Yagi-Uda nanoantenna array*, DPG Spring Meeting, Regensburg, Germany, Talk O 44.1 (2010).

[2] D. Dregely, R. Taubert, and H. Giessen, *3D optical Yagi-Uda nanoantenna array*, CLEO: QELS - Fundamental Science, San Jose, USA, Talk QMH5 (2010).

[3] D. Dregely, R. Taubert, and H. Giessen, *3D optical Yagi-Uda nanoantenna array*, Metamaterials'2010, Karlsruhe, Germany, Talk (2010).

[4] D. Dregely, M. Schäferling, and H. Giessen, *Spiral Optical Nanoantenna*, DPG Spring Meeting, Dresden, Germany, Talk O 50.3 (2011).

[5] D. Dregely, K. Lindfors, J. Dorfmüller, M. Hentschel, M. Becker, J. Wrachtrup, M. Lippitz, R. Vogelgesang, and H. Giessen, *Coupling of quantum emitters to plasmonic nanoantennas*, 4th International Workshop on Positioning of Single Nanostructures - Single Quantum Devices, Lake Como, Italy, Talk (2011).

[6] R. Ameling, D. Dregely, and H. Giessen, *Strong coupling of localized and surface plasmons to microcavity modes*, Metamaterials'2011, Barcelona, Spain, Poster (2011).

[7] D. Dregely, F. Neubrech, H. Duan, and H. Giessen, *Quantitative mapping of plasmonic near-fields using infrared far-field vibrational spectroscopy*, Nanometa 2013, Seefeld, Austria, Talk (2013).

[8] D. Dregely, F. Neubrech, H. Duan, and H. Giessen, *Quantitative mapping of plasmonic near-field intensity using infrared far-field vibrational spectroscopy*, DPG Spring Meeting, Regensburg, Germany, Talk O 7.2 (2013).

[9] D. Dregely, K. Lindfors, M. Lippitz, and H. Giessen, *Experimental realization of an optical point-to-point connection with nanoantennas*, DPG Spring Meeting, Regensburg, Germany, Talk O 7.4 (2013).

[10] D. Dregely, F. Neubrech, H. Duan, and H. Giessen, *Quantitative mapping of plasmonic near-fields using infrared far-field vibrational spectroscopy*, META'13, Sharjah, UAE, Talk (2013).

[11] D. Dregely, F. Neubrech, H. Duan, and H. Giessen, *Direct mapping of plasmonic near-fields using infrared far-field vibrational spectroscopy*, CLEO/Europe - IQEC, Munich, Germany, Poster II-P.11 WED (2013).

[12] D. Dregely, K. Lindfors, M. Lippitz, and H. Giessen, *Optical phased array nanoantenna link*, CLEO/Europe - IQEC, Munich, Germany, Talk II-2.4 WED (2013).

[13] D. Dregely, F. Neubrech, H. Duan, and H. Giessen, *Quantitative mapping of plasmonic near-fields using infrared far-field vibrational spectroscopy*, 6th International Conference on Surface Plasmon Photonics, Ottawa, Canada, Talk Mo-27-C-3 (2013).

[14] D. Dregely, K. Lindfors, M. Lippitz, and H. Giessen, *Optical phased array nanoantenna link*, 6th International Conference on Surface Plasmon Photonics, Ottawa, Canada, Poster Tu-28-P-27 (2013).

[15] D. Dregely, F. Neubrech, H. Duan, and H. Giessen, *Quantitative mapping of plasmonic near-fields using infrared far-field vibrational spectroscopy*, CLEO: QELS - Fundamental Science, San Jose, USA, Talk QTu1B.4 (2013).

[16] D. Dregely, F. Neubrech, H. Duan, and H. Giessen, *Direct mapping of plasmonic near-field intensity using infrared far-field vibrational spectroscopy*, ICMAT, Singapore, Talk ICMAT13-A-1574 (2013).

[17] D. Dregely, K. Lindfors, M. Lippitz, and H. Giessen, *Optical phased array nanoantenna link*, ICMAT, Singapore, Poster ICMAT13-A-1575 (2013).

[18] D. Dregely, K. Lindfors, M. Lippitz, and H. Giessen, *Steerable nanoantenna link*, KFN Statusworkshop, Bad Herrenalb, Germany, Talk (2013).

TALKS & POSTERS (CO-AUTHORED):

[1] R. Taubert, R. Ameling, L. Langguth, D. Dregely, and H. Giessen, *Bragg Plasmonics*, DPG Spring Meeting, Regensburg, Germany, Talk O 15.29 (2010).

[2] M. Becker, D. Dregely, H. Fedder, F. Jelezko, H. Giessen, and J. Wrachtrup, *Tailoring the Single Photon Emission from Nitrogen-Vacancy Centres using Metallic Structures*, DPG Spring Meeting, Dresden, Germany, Poster O 15.29 (2011).

[3] M. Schäferling, D. Dregely, T. Weiss, and H. Giessen, *Quantifying Chirality in 2D and 3D Metallic Metamaterials*, DPG Spring Meeting, Dresden, Germany, Talk O 76.2 (2011).

[4] J. Dorfmüller, D. Dregely, M. Esslinger, W. Khunsin, R. Vogelgesang, K. Kern, and H. Giessen, *Near-Field Imaging of Directive Optical Yagi-Uda Nanoantennas*, DPG Spring Meeting, Dresden, Germany, Talk O 28.2 (2011).

[5] S.V. Lobanov, T. Weiss, D. Dregely, H. Giessen, N.A. Gippius, and S.G. Tikhodeev, *Emission of an oscillating point dipole from a gold Yagi-Uda nanoantenna array*, 11th International Conference on Physics of Light-Matter Coupling in Nanostructures, Berlin, Germany, Talk (2011).

[6] S.V. Lobanov, T. Weiss, D. Dregely, H. Giessen, N.A. Gippius, and S.G. Tikhodeev, *Interaction of a point emitter with a gold Yagi-Uda nanoantenna array*, 19th International Symposium on Nanostructures: Physics and Technology, Ekaterinburg, Russia, Talk (2011).

[7] M. Hentschel, N. Liu, D. Dregely, and H. Giessen, *Plasmonic oligomers: The role of individual particles in collective behavior*, CLEO: QELS - Fundamental Science, Baltimore, USA, Invited Talk QFA5 (2011).

[8] M. Schäferling, D. Dregely, M. Hentschel, T. Weiss, and H. Giessen, *Spatially resolved enhancement of chirality in planar and 3D chiral plasmonic nanostructures*, Fourth International Workshop on Theoretical and Computational Nano-Photonics (TaCoNa), Bad Honnef, Germany, Poster (2011).

[9] M. Schäferling, D. Dregely, M. Hentschel, and H. Giessen. *Spatially resolved enhancement of chirality in planar and 3D chiral metamaterials*, Metamaterials'2011, Barcelona, Spain, Talk (2011).

[10] H. Giessen, N. Liu, M. L. Tang, M. Hentschel, R. Taubert, A. Radke, D. Dregely, A. Tittl, M. Mesch, and A. P. Alivisatos, *Complex and 3D plasmonics: Coupling, sensing, and chirality*, ICONN, Perth, Australia, Plenary Talk (2012).

[11] M. Schäferling, M. Hentschel, D. Dregely, and H. Giessen, *Local Enhancement of Optical Chirality in Planar and 3D Plasmonic Nanostructures*, DPG Spring Meeting, Berlin, Germany, Talk O 85.2 (2012).

[12] A. Tittl, P. Mai, R. Taubert, D. Dregely, J. Dorfmüller, C. Kremers, D. Chigrin, and H. Giessen, *Palladium-Based Plasmonic Hydrogen-Sensing: Perfect Absorbers and Antenna-Enhanced Geometries*, META'12, Paris, France, Talk (2012).

[13] A. Tittl, P. Mai, R. Taubert, D. Dregely, J. Dorfmüller, C. Kremers, D. Chigrin, and H. Giessen, *Palladium-Based Plasmonic Hydrogen-Sensing: Perfect Absorbers and Antenna-Enhanced Geometries*, MRS Spring Meeting, San Francisco, USA, Talk (2012).

[14] M. Schäferling, M. Hentschel, D. Dregely, and Harald Giessen, *Local Enhancement of Optical Chirality in Plasmonic Nanostructures*, 8th Workshop on Numerical Methods for Optical Nano Structures, Zurich, Switzerland, Talk (2012).

[15] S.V. Lobanov, T. Weiss, D. Dregely, H. Giessen, N.A. Gippius, and S.G. Tikhodeev, *Control of quantum dots emission via an ensemble of optical Yagi-Uda nanoantennas*, XII All-Russian Workshop: Wave phenomena in heterogeneous environments, Moscow, Russia, Poster (2012).

[16] S. Gupta, J. W. Rinne, T. C. Galvin, K. A. Arpin, D. Dregely, H. Giessen, J. G. Eden, P. Wiltzius, and P. V. Braun, *Design and Fabrication of Helical Structures via Proximity-field Nano-Patterning (PnP) for Application as Chiral Metamaterials*, CLEO: QELS - Fundamental Science, San Jose, USA, Talk CF2A.4 (2012).

[17] M. Schäferling, D. Dregely, M. Hentschel, X. Yin, J. Dorfmüller, and H. Giessen, *Local enhancement of optical chirality in plasmonic nanostructures*, 12th International Conference on Near-field Optics and Related Techniques (NFO), San Sebastian, Spain, Poster (2012).

[18] M. Schäferling, M. Hentschel, D. Dregely, X. Yin, and H. Giessen. *Design of Plasmonic Nanostructures for Chiral Sensing*. Fifth International Workshop on Theoretical and Computational Nano-Photonics (TaCoNa), Bad Honnef, Germany (2012).

[19] J. Y. Chin, T. Steinle, T. Wehlus, D. Dregely, T. Weiss, V. I. Belotelov, B. Stritzker, and H. Giessen, *Nonreciprocal plasmonics: thin film Faraday rotator*, Nanometa, Seefeld, Austria, Invited Talk (2013).

[20] L. E. Kreilkamp, V. I. Belotelov, I. A. Akimov, M. Bayer, T. Wehlus, B. Stritzker, J. Chin, S. Neutzner, D. Dregely, and H. Giessen, *Hybrid waveguide-particle-plasmon-polaritons enhance transverse magneto-optical Kerr effect*, DPG Spring Meeting, Regensburg, Germany, Talk O 19.2 (2013).

[21] J. Chin, T. Steinle, T. Wehlus, T. Weiss, D. Dregely, V. Belotelov, B. Stritzker, and H. Giessen, *Nonreciprocal Plasmonics: Thin Film Faraday Rotator*, DPG Spring Meeting, Regensburg, Germany, Talk O 19.12 (2013).

[22] J. Y. Chin, T. Steinle, T. Wehlus, D. Dregely, T. Weiss, V. I. Belotelov, B. Stritzker, and H. Giessen, *Nonreciprocal plasmonics: thin film Faraday rotator*, Meta'13, Sharjah, UAE, Talk (2013).

[23] F. Neubrech, D. Dregely, H. Giessen, and A. Pucci, *Probing near-fields of metallic nanoantennas*, Seminar Kirchhoff Institute for Physics, Heidelberg, Germany, Talk (2013).

[24] J. Y. Chin, T. Steinle, T. Wehlus, D. Dregely, T. Weiss, V. I. Belotelov, B. Stritzker, and H. Giessen, *Nonreciprocal plasmonics: Giant enhancement of thin film Faraday rotation*, 6th International Conference on Surface Plasmon Photonics, Canada, Talk (2013).

[25] J. Y. Chin, L. E. Kreilkamp, V. I. Belotelov, S. Neutzner, D. Dregely, T. Wehlus, I. A. Akimov, B. Stritzker, M. Bayer, and H. Giessen, *Plasmonically Enhanced Transverse Magneto-Optical Kerr Effect*, CLEO: QELS - Fundamental Science, San Jose, USA, Talk (2013).

[26] K. Lindfors, D. Dregely, M. Lippitz, and H. Giessen, *Steerable plasmonic point-to-point nanoantenna link*, CLEO: QELS - Fundamental Science, San Jose, USA, Postdeadline Talk QTh5B.9 (2013).

[27] J. Y. Chin, T. Steinle, T. Wehlus, D. Dregely, T. Weiss, V. I. Belotelov, B. Stritzker, and H. Giessen, *Nonreciprocal Plasmonics Enhancing Thin Film Faraday Rotation*, ICMAT, Singapore, Talk (2013).

[28] F. Neubrech, D. Dregely, J. Zhao, and H. Giessen, *Nanoantenna-enhanced mid-IR vibration spectroscopy with single molecular layer sensitivity*, IRMMW-THz, Mainz, Germany, Talk (2013).

CONTENTS

LIST OF FIGURES

LIST OF TABLES

ACRONYMS

2D	two-dimensional
3D	three-dimensional
AFM	atomic force microscopy
APD	avalanche photo diode
aSNOM	apertureless scanning near-field optical microscopy
CCD	charged coupled device
CL	cathodoluminescence
CST	CST - Computer Simulation Technology
EBL	electron beam lithography
EELS	electron energy loss spectroscopy
EIA	electromagnetically induced absorption

EIT	electromagnetically induced transparency
FTIR	Fourier transform infrared
FWHM	full width at half maximum
HOMO	highest occupied molecular orbital
HSQ	hydrogen silsesquioxane
IR	infrared
IRRAS	infrared reflection absorption spectroscopy
LUMO	lowest unoccupied molecular orbital
MIBK	Methyl isobutyl ketone
NA	numerical aperture
NEP	N-Ethyl-2-pyrrolidone
ODT	octadecanethiol
PEEM	photoemission electron microscopy
PMMA	polymethylmethacrylat
PSF	point-spread function
RF	radiofrequency
SAM	self-assembled monolayer
SEIRA	surface-enhanced infrared absorption
SEM	scanning electron microscopy
SERS	surface-enhanced Raman scattering
SNOM	scanning near-field optical microscopy
TEM	transmission electron microscopy

TERS	tip-enhanced Raman spectroscopy
THz	terahertz
TPL	two-photon luminescence

1

INTRODUCTION

When light with a certain frequency impinges on metallic nanoparticles, a collective oscillation of the conduction electrons will be excited. On the one hand, this is associated with a very high near-field intensity in a sub-wavelength volume close to the particles. On the other hand, the far-field scattering and absorption cross-sections of the nanoparticles become tremendously enhanced. Consequently, metallic nanostructures are able to interact with light efficiently at the nanoscale, deeply below the diffraction limit. The related research area is termed *plasmonics*. Besides the resonant properties of metal nanoparticles, the field of plasmonics also studies charge-density waves on metal surfaces, which propagate in one or two dimensions and provide sub-wavelength confinement in the other dimensions. The research on plasmonics has developed rapidly over the past years and holds promising applications in the future technology realm of nanooptics [1–7].

One of the most promising research topics in plasmonics is *optical antennas*. More than half a century ago, in the year 1959, `Richard Feynman` gave the renowned talk *There's Plenty of Room at the Bottom* at the annual meeting of the American Physical Society at Caltech [8]. He spoke about *"the problem of manipulating and controlling things on a small scale"* and inspired scientific ideas, which contributed to the birth of the entire field of nanotechnology a few decades later. In terms of manipulating light at the nanoscale Feynman envisioned [8]:

"Consider, for example, a piece of material in which we make little coils and condensers (or their solid state analogs) 1,000 or 10,000 angstroms in a circuit, one right next to the other, over a large area, with little antennas sticking out at the other end—a whole series of circuits. Is it possible, for example, to emit light from a whole set of antennas, like we emit radio waves from an organized set

of antennas to beam the radio programs to Europe? The same thing would be to beam the light out in a definite direction with very high intensity. (Perhaps such a beam is not very useful technically or economically.)"

The technologies, which Feynman fancied, came into existence after four to five decades. They were materialized largely because of the advances in nanofabrication, which were predicted in Feynman's talk as well in remarkable details. Notably, some of these visionary concepts were demonstrated only very recently; some are still the vital topics in the contemporary research efforts on nanocircuitry [9, 10], optical antennas [11–14], etc. The emergence of optical antennas is triggered by the development of near-field optics and its quest for deep sub-wavelength resolution [15]. Near-field optics originated from the idea of `Edward Synge`, in 1928, to use colloidal gold particles in order to break the diffraction limit in optical microscopy [16]. The first optical near-field measurement was published in 1984 by `Dieter W. Pohl` [17]. In 1985, `Wessel` attributed the term *optical antenna* to a gold nanoparticle, which supports surface plasmon resonances [18]. Shortly afterwards, this idea was experimentally demonstrated by `Dieter W. Pohl` and `Ulrich Fischer` [19]. Later on, in 1997, `Grober et al.` published a paper where they proposed an optical Bow-Tie antenna as near-field probe to achieve higher spatial resolution and demonstrated the proof-of-principle by a measurement using microwave radiation [20]. In 1999, `Pohl` gave an inspiring talk entitled *"Near-field optics seen as an antenna problem"* [21] in which he drew analogies from antenna concepts in the radiofrequency (RF) regime to the resonant properties supported by metallic nanoantennas in the optical frequency regime. Since then a lot of research effort has been invested in developing antennas in the optical regime by shrinking the size of conventional RF antennas and the field of *optical nanoantenna* emerged. Some of the antenna structures among those being researched are dipole [11, 22] and monopole antennas [23–26], patch antennas [27, 28], Yagi-Uda [29–35] and log-periodic antennas [36–39], Bow-Tie antennas [40–42], spiral antennas [43–47], etc. They have proved useful in applications such as fluorescence enhance-

ment, redirecting light of single photon sources, nanoscale photodetection, non-linear frequency mixing, and ultra-sensitive biosensing. Despite some differences between optical nanoantennas and their RF counterparts [48–50], it has been shown that most RF concepts remain applicable in the optical regime [24, 27, 51].

Over the past decade, nanotechnology and the research on optical antennas have progressed tremendously. Nevertheless, the technological and economic relevance of these nanoscale devices are to be proved. There is still a long way to go for the applications of optical nanoantennas to be realized and the technologies based on nanooptics to mature.

In this thesis, we present several novel concepts of optical nanoantennas and their applications. We start with an introduction to the fundamental theory and the terminologies used throughout this thesis, and, next to it, a chapter on the methods of nanofabrication, numerical simulations, and optical characterization that are employed throughout this thesis.

In the following chapter we engineer the optical radiation using Yagi-Uda nanoantennas. Previously, similar geometries were demonstrated to transmit directionally radiation. Here, we focus on the receiving properties of the antennas and realize high directivities, which make optical Yagi-Uda nanoantennas promising components for antenna links [52]. In the first part of the chapter we investigate the near-field receiving mechanism of the Yagi-Uda antennas. By using apertureless scanning near-field optical microscopy (aSNOM), we are able to image the amplitude and the phase of the fields around the antenna. The result allows us to study the plasmonic modes at $\lambda = 1064$ nm in the resonant nanoantenna. The directivity is studied by illuminating the antenna from two opposite directions and characterizing the difference of the measured near-field intensity. This work is an important step toward an accurate and versatile characterization of optical antennas. In the second part of this chapter we present a three-dimensional (3D) optical Yagi-Uda nanoantenna array, which operates in the optical frequency regime around $\lambda = 1.5$ μm. One of the key issues with optical nanoantennas is either to direct effectively the radiation of a local source to radiation in the third

dimension, which is perpendicular to the plane of the antenna array, or to receive light from this third dimension and to confine it to a deep sub-wavelength volume. Our antenna array can emit and detect light in the third dimension and shows a high directivity (i.e. a narrow beam width), thanks to the design of the array.

One key property of plasmonic antennas is the deep sub-wavelength confinement of electromagnetic energy, which results in high near-field intensities. Recently, plasmonic near-field enhancement has been utilized to increase light-matter interaction. For instance, matters such as quantum emitters or molecules are coupled to plasmonic structures. Antennas with different structural geometries were employed to enhance the coupling and to boost the signal, which is related to the near-field distribution. Assessing plasmonic near-field intensities in the infrared (IR) and terahertz (THz) region is important for the design of novel plasmonic structures and for the optimization of the coupling of plasmonic structures to molecular vibrations to detect and to identify trace substances. We present a versatile and diffraction unlimited technique to map plasmonic near-fields in the infrared. We position molecules with a 10 nm accuracy in the vicinity of plasmonic antennas and quantify the near-field intensity via the resonant excitation of the molecular vibrations. We measure the signal in the far-field with conventional Fourier transform infrared (FTIR) spectroscopy. Our method can be applied to resonant plasmonic structures from the near-IR region to the THz region. This technique is also applicable to complex 3D plasmonic structures, which are often embedded in a dielectric matrix and cannot be investigated by state-of-the-art methods, such as scanning near-field optical microscopy (SNOM). The presented method is an entirely new approach to measure plasmonic near-field intensities in the infrared region. Its implementation is simple and brings along new possibilities.

In the last part of this thesis, we report on the first experimental realization of a wireless point-to-point antenna link. Optical power transfer between two plasmonics nanoantennas with 38 λ distance is observed. Additionally, we demonstrate how to steer this link over a very broad angular range of 29° and how to link different emitters and receivers,

using a phase shifting technique. The antenna link has a working wavelength of $\lambda = 785$ nm. It enables high-bandwidth communication at the nanoscale. We show that a nanoantenna link does not suffer from high losses compared to the plasmonic waveguide connections. This feature implies potential devices with low-loss on-chip and chip-to-chip high-speed data communication. The beamsteering functionality is analogous to phased array radar technology in RF and provides a flexible spatial control of the antenna radiation. Furthermore, the transmitter antenna has a footprint of only 850×50 nm^2, which is favorable for high integration density in future photonic circuits.

2

THEORY

This chapter describes the theoretical background of the thesis. First, starting from *Maxwell's equations*, the fundamentals of electrodynamics are introduced. Then, the *angular spectrum representation* of electromagnetic fields is derived, which is used in this thesis to calculate the fields in a high-numerical aperture (NA) objective. The next section discusses *Green's function formalism*. It allows to calculate the electromagnetic fields radiated from an arbitrary current source in a specific geometry. We use it to calculate the electric field of a point dipole source, which gives the typical *dipole field*. It will be used later in this thesis to model the radiation pattern of optical plasmonic antennas. The second part of the chapter introduces *plasmonics*, which is the research on nanooptics involving metallic nanostructures. To understand their intriguing properties we introduce the *Drude model*, which describes the dielectric properties of noble metals at optical frequencies. It is shown that plasmonic structures, termed *optical antennas*, exhibit a resonant behavior when they interact with light and the scattering and absorption of light as well as the optical near field is enhanced. This resonance is called *particle plasmon resonance* or *localized surface plasmon resonance*. The resonant wavelength can be tuned throughout the optical spectral region making optical antennas key elements in a plethora of applications, such as biosensing, nonlinear frequency generation, single photon devices or photonic circuits based on nanodetectors, nanolasers, and nanosale optical transmission. The last section is devoted to the basic theory of RF antenna arrays.

2.1 FUNDAMENTALS OF ELECTROMAGNETIC THEORY

2.1.1 *Maxwell's equations and electromagnetic wave propagation*

Electromagnetic radiation including light propagation is described with Maxwell's equations, presented here in their macroscopic form:

$$\begin{aligned} \nabla \cdot \mathbf{D} &= \rho, \\ \nabla \times \mathbf{H} &= \mathbf{j} + \frac{\partial \mathbf{D}}{\partial t}, \\ \nabla \cdot \mathbf{B} &= 0, \\ \nabla \times \mathbf{E} &= -\frac{\partial \mathbf{B}}{\partial t}. \end{aligned} \tag{1}$$

E, **D**, **H**, and **B** denote the electric field, the electric displacement field, the magnetic field, and the magnetic induction, respectively. **j** is the current density and ρ the electric charge density. This set of equations only describes the fields generated by currents and charges. It does not describe the interaction of the electromagnetic fields with the matter in which the currents and charges are generated. The electromagnetic properties of matter are described in terms of macroscopic polarization **P** and magnetization **M** following

$$\begin{aligned} \mathbf{D} &= \epsilon_0 \mathbf{E} + \mathbf{P}, \\ \mathbf{B} &= \mu_0 \mathbf{H} + \mathbf{M}, \end{aligned} \tag{2}$$

with ϵ_0 and μ_0 being the permittivity and the permeability of vacuum, respectively.

The *constitutive equations* are the necessary relations to describe the material response under the influence of an electromagnetic field. Considering a linear medium, they become

$$\begin{aligned} \mathbf{D}(\mathbf{k}, \omega) &= \epsilon_0 \epsilon(\mathbf{k}, \omega) \mathbf{E}(\mathbf{k}, \omega), \\ \mathbf{B}(\mathbf{k}, \omega) &= \mu_0 \mu(\mathbf{k}, \omega) \mathbf{H}(\mathbf{k}, \omega), \end{aligned} \tag{3}$$

where $\epsilon(\mathbf{k}, \omega)$ and $\mu(\mathbf{k}, \omega)$ are the dispersive electric permittivity and magnetic permeability, respectively. Usually the magnetization of materials at optical frequencies is negligible and μ in Equation 3 becomes

1. The light-matter interaction is dominated by the response of the matter to the external electric field, which for a linear medium induces a polarization $\mathbf{P}$ following

$$\mathbf{P}(\mathbf{k},\omega) = \epsilon_0 \chi(\mathbf{k},\omega)\mathbf{E}(\mathbf{k},\omega). \tag{4}$$

Substituting Equation 4 into Equation 2 and comparing it to Equation 3 gives an expression between the dielectric function ϵ and the susceptibility χ:

$$\epsilon(\mathbf{k},\omega) = 1 + \chi(\mathbf{k},\omega). \tag{5}$$

The propagation of an electromagnetic wave generated by a current source in a non-dispersive, linear and isotropic medium is described by the wave equation derived from Maxwell's equations and the constitutive relations

$$\nabla \times \nabla \times \mathbf{E} + \epsilon_0 \epsilon \mu_0 \mu \frac{\partial^2 \mathbf{E}}{\partial t^2} = -\mu_0 \mu \frac{\partial \mathbf{j}}{\partial t}. \tag{6}$$

In a linear, homogeneous, isotropic and source-free medium, the ansatz of a harmonic monochromatic plane wave $\mathbf{E}(\mathbf{r}) = \mathbf{E}_0 e^{i(\mathbf{kr}-\omega t)}$ is made. As a result Equation 6 becomes the homogeneous Helmholtz equation:

$$(\nabla^2 + k^2)\mathbf{E}(\mathbf{r}) = 0, \tag{7}$$

with k being the wavenumber $k = n\frac{\omega}{c}$ in the medium with refractive index $n = \sqrt{\mu\epsilon}$.

2.1.2 *Angular spectrum representation of optical fields*

In Section 6.2 we will use the *angular spectrum representation* to calculate the electromagnetic vectorial field in the focus of a high-NA objective and to determine the spatial resolution of our imaging system. In general it allows to analyze the propagation of fields. A short introduction to the formalism is presented here.

An electric field $\mathbf{E}(x,y,z)$ in a plane $z = \text{const.}$ can be expressed with its Fourier transform $\hat{\mathbf{E}}$ in this plane:

$$\mathbf{E}(x,y,z) = \iint_{-\infty}^{\infty} \hat{\mathbf{E}}(k_x,k_y,z) e^{i(k_x x + k_y y)} dk_x dk_y. \tag{8}$$

Substituting Equation 8 into the source-free Helmholtz equation (Equation 7) it turns out that the spectrum $\hat{\mathbf{E}}(k_x, k_y, z)$ evolves along the z-direction as

$$\hat{\mathbf{E}}(k_x, k_y, z) = \hat{\mathbf{E}}(k_x, k_y, 0) e^{\pm i k_z z}$$
$$\text{with} \quad k_z = \sqrt{k^2 - k_x^2 - k_y^2}. \tag{9}$$

We obtain two waves as solution, where the $+$ $(-)$ sign represents a wave propagating into the half space $z > 0$ ($z < 0$). We additionally have to assume $\mathfrak{Im}(k_z) > 0$, which ensures that the solutions do not diverge for $z \to \pm\infty$. Combining Equation 9 with Equation 8 yields an expression of the electric field at any arbitrarily chosen plane $z = \text{const.}$, which is the *angular spectrum representation*:

$$\mathbf{E}(x, y, z) = \iint_{-\infty}^{\infty} \hat{\mathbf{E}}(k_x, k_y, 0) e^{i(k_x x + k_y y \pm k_z z)} dk_x dk_y. \tag{10}$$

The magnetic field $\mathbf{H}$ can be calculated following the same approach or from Equation 10 using Maxwell's equations.

2.1.3 *Green's function for the electric field in a homogeneous environment*

The electromagnetic fields in an arbitrary environment generated by the charge and current sources can be calculated using the *Green's function*. In its general form, the Green's function $\overline{\mathbf{G}}(\mathbf{r}, \mathbf{r}')$ is the response at a point $\mathbf{r}$ of an unit point source at $\mathbf{r}'$ described by the following relation [53]

$$\Gamma \overline{\mathbf{G}}(\mathbf{r}, \mathbf{r}') = \bar{\mathbf{I}} \delta(\mathbf{r} - \mathbf{r}'), \tag{11}$$

where Γ is a linear operator and $\bar{\mathbf{I}}$ is the identity matrix.

Assuming harmonic time dependence and a non-magnetic media the wave equation (Equation 6) can be written in the operator form

$$\Gamma \mathbf{E}(\mathbf{r}) = i\omega\mu_0 \mathbf{j}(\mathbf{r}), \tag{12}$$

where $\Gamma = \nabla \times \nabla \times -k^2$. We can multiply Equation 11 with the current density $\mathbf{j}(\mathbf{r})$ and integrate it over the volume of the source V. This

gives an integral expression of the current source, which is substituted in Equation 12. The electric field $\mathbf{E}(\mathbf{r})$ can than be solved as [53]

$$\mathbf{E}(\mathbf{r}) = \mathbf{E}_0(\mathbf{r}) + i\omega\mu_0 \int_V \overline{\mathbf{G}}(\mathbf{r}, \mathbf{r}')\mathbf{j}(\mathbf{r}')dV', \tag{13}$$

where the homogeneous solution $\mathbf{E}_0(\mathbf{r})$ has been added. With the Green's function for the operator Γ we can calculate the electric field generated by a current source at any point outside the source. The expression for a homogeneous medium reads as [53]

$$\overline{\mathbf{G}}(\mathbf{r}, \mathbf{r}') = \frac{e^{ikR}}{4\pi R k^2}\left[\frac{ikR-1}{R^2}(\bar{\mathbf{I}} - 3\hat{\mathbf{R}}\otimes\hat{\mathbf{R}}) + k^2(\bar{\mathbf{I}} - \hat{\mathbf{R}}\otimes\hat{\mathbf{R}})\right], \tag{14}$$

with R being the absolute value of $\mathbf{R} = \mathbf{r} - \mathbf{r}'$ and $\hat{\mathbf{R}}\otimes\hat{\mathbf{R}}$ being the outer product of the unit vector along $\mathbf{R}$. This is the central result of this section and will be used in Section 6.2 to calculate the scattering response of plasmonic dipole antennas. In the following section we will use this expression to determine the fields of a single Hertzian dipole.

2.1.4 *Electric field of an electric dipole*

An oscillating electric point dipole generates propagating electromagnetic fields, which we will determine in this section. The current density of a dipole oscillating with frequency ω at $\mathbf{r}_0$ is

$$\mathbf{j}(\mathbf{r}) = \frac{d}{dt}\mathbf{p}(t)\delta(\mathbf{r} - \mathbf{r}_0) = -i\omega\mathbf{p}\delta(\mathbf{r} - \mathbf{r}_0). \tag{15}$$

The Green's function formalism discussed in the previous section allows to directly calculate the electric field of the dipole. By introducing the current density from Equation 15 into Equation 13 and using the expression for the Green's function from Equation 14 we obtain the expression for the electric field generated by the dipole

$$\mathbf{E}_{dip}(\mathbf{r}) = \frac{e^{ikR}}{4\pi\epsilon_0}\left[\frac{k^2}{R}\cdot(\mathbf{p} - \hat{\mathbf{R}}\cdot(\hat{\mathbf{R}}\cdot\mathbf{p})) + \left(\frac{1}{R^3} - \frac{ik}{R^2}\right)(3\hat{\mathbf{R}}\cdot(\hat{\mathbf{R}}\cdot\mathbf{p}) - \mathbf{p})\right], \tag{16}$$

where R is the absolute value of $\mathbf{R} = \mathbf{r} - \mathbf{r}_0$ and $\hat{\mathbf{R}}$ the unit vector along $\mathbf{R}$.

Three different regions of the electric field are identified, which scale with $1/(kR)^3$,$1/(kR)^2$ and $1/kR$. They are termed *near-field*, *intermediate-field* and *far-field* regions, respectively. In the near-field region the electric

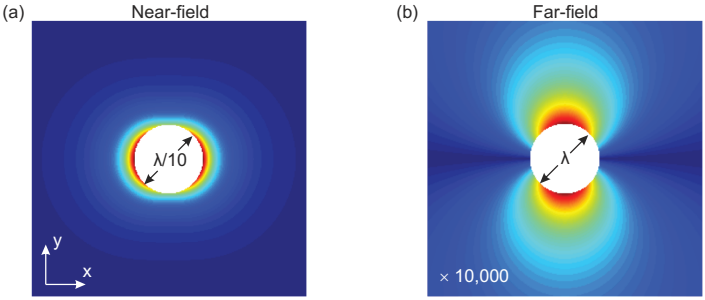

Figure 1: The dipole fields $|\mathbf{E}_{dip}|$ in the near-field (a) and far-field regions (b) are shown for a dipole moment oriented along the x-direction. The far-field stretches out along the y-direction in contrary to the field close to the dipole, which is elongated along the x-direction. Adapted from [53].

field is elongated along the direction of the dipole moment, as shown in Figure 1 (a). Far away from the dipole source ($r \gg \lambda$), the field spreads out perpendicularly to the orientation of the dipole moment [Figure 1 (b)] and the polarization of the electric field vector $\mathbf{E}_{dip}$ is perpendicular to the wavevector $\mathbf{k}$.

2.2 PLASMONICS

One solution of Maxwell's equation at a metal-dielectric interface are charge density waves, which propagate on the metal surface with strong confinement [54–60]. They are termed *surface plasmons* and constitute one part of the field of plasmonics [5, 61, 62], as to be distinguished from *localized surface plasmons* or, in other words, *particle plasmons*, which occur in metal nanostructures. They allow confinement of incident optical fields to the nanoscale associated with high near-field intensities [63–70]. They additionally enhance the radiation from sub-wavelength sources [27, 51, 71–73]. In analogy to the RF domain such particles are called optical

antennas [12–14, 48, 74–78]. They have led to breakthroughs in enhanced nonlinear frequency conversion [11, 79], ultra-sensitive sensing down to the single molecule level [80–82], emission enhancement and radiation engineering of single photons [41, 83–87], and enhanced photo-detection at the nanoscale [88, 89]. One of the envisioned applications of plasmonics is optical on-chip circuitry [90] with nanoscale footprint, which combines photonics with integrated electronics [2] for the uses in high-speed computing and high-bandwidth communication. This will be discussed in detail in Chapter 6. In this thesis we deal exclusively with *particle plasmons*. Here we give a short introduction of the optical properties of metal nanoparticles.

2.2.1 *The Drude model*

The dielectric function of metals in the optical frequency region can be described by the *Drude model*. It assumes an unbound electron plasma, which is displaced against a fixed background of positive ion cores by an external field, leading to electric polarization. Electrostatic interactions between the electrons and the influence of the lattice potential are not taken into account. Major deviations from this model occur in the visible spectral region due to interband transitions in noble metals. In the near-infrared and infrared region the interband transitions are not excited and the Drude model gives an accurate description of the optical properties of noble metals.

The motion of the electron plasma is described by

$$m\ddot{\mathbf{r}} + m\gamma\dot{\mathbf{r}} = -e\mathbf{E}, \tag{17}$$

where γ is the collision frequency, which takes into account collisions of the electron with other electrons and ions. By assuming a time-harmonic incident field $\mathbf{E}(t) = \mathbf{E}_0 e^{-i\omega t}$ we can solve the differential equation and express the electric polarization $\mathbf{P} = -ne\mathbf{r}$ where n is the electron density as [91]

$$\mathbf{P} = -\frac{ne^2}{m(\omega^2 + i\gamma\omega)}\mathbf{E}. \tag{18}$$

With the relation

$$\mathbf{P} = \epsilon_0 \chi \mathbf{E} = \epsilon_0 (\epsilon - 1)\mathbf{E}, \tag{19}$$

the complex dielectric function $\epsilon(\omega)$ in the Drude model becomes

$$\epsilon(\omega) = 1 - \frac{\omega_p^2}{\omega^2 + i\omega\gamma} = 1 - \frac{\omega_p^2}{\omega^2 + \gamma^2} + i\frac{\omega_p^2 \gamma}{\omega(\omega^2 + \gamma^2)}, \tag{20}$$

where $\omega_p = \sqrt{\frac{ne^2}{\epsilon_0 m}}$ is the *plasma frequency*. In Figure 2 we plot the measured real and imaginary parts of $\epsilon(\omega)$ of gold as a function of frequency (circles, taken from [92]). In the imaginary part (upper panel)

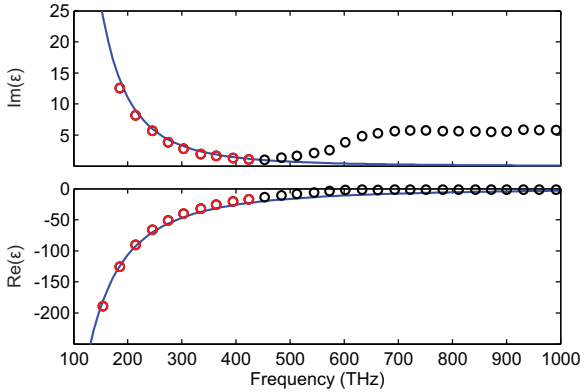

Figure 2: Imaginary (upper panel) and real part (lower panel) of the dielectric function of gold are plotted. Experimental data (circles, taken from [92])ey are fitted with the Drude model (blue curves) in the region where interband transitions are not affecting the absorption (red circles).

the increased absorption for frequencies higher than 440 THz is due to the onset of the interband transitions from the 5d band to the 6sp band around 440 Thz and 580 Thz [93]. The experimental data therefore deviate from the Drude model (blue curve), which is only fitted to the region indicated by the red circles. The fitted values for the plasma frequency ω_p and the collision frequency γ are 2074 THz and 20.78 THz, respectively.

2.2.2 *Optical antennas: Resonant metallic nanoparticles*

In the last decade, resonant metallic nanoparticles, termed optical antennas or nanoantennas [12, 14, 76, 78, 94, 95], attracted a lot of interest because of their unique optical properties and their potential for applications [3, 13, 62, 96]. Nanofabrication techniques, such as electron-beam lithography, ion-beam milling, and self-assembly, as well as sophisticated characterization techniques, such as near-field microscopy and fluorescence microscopy have been used to study these nanostructures. Here, we discuss the origin of resonances occurring in metallic nanoantennas in the quasistatic approximation. These resonances are called *localized surface plasmons* and can be excited via an incident light field. We will see that the spectral position of the resonance is tunable from the visible to the infrared region for noble metal particles.

2.2.2.1 *Electrostatic approximation*

For particles with a characteristic size a much smaller compared to the incident wavelength

$$a \ll \lambda, \tag{21}$$

the optical properties can be treated in the *quasistatic approximation* where the phase of the incident field does not vary across the particle. For larger particles, the quasistatic approximation is not valid anymore and a rigorous electromagnetic theory is required. Such a theory was developed for spherical particles by `Gustav Mie` in a seminal paper 1908 [97] and is treated in a variety of text books [98, 99]. In this thesis we focus on metallic nanoparticles, which fulfill the condition in Equation 21 and therefore treat their optical response in the quasistatic approximation. In this case the electric field can be calculated from a potential Φ via $\mathbf{E} = -\nabla\Phi$. We use Maxwell's equation (Equation 1) in a charge-density free environment to write down the *Laplace equation*

$$\nabla^2\Phi = 0. \tag{22}$$

For spherical particles and an incident electric field along the z-axis, $\mathbf{E} = E_0\hat{\mathbf{z}}$, the problem is symmetric along the azimuthal direction (see

Figure 3). The solution to the Laplace equation for the potential in-

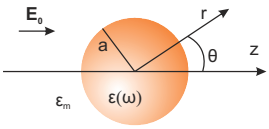

Figure 3: Sketch of a metallic sphere placed in a homogeneous environment under the influence of an electrostatic field. Adapted from [91].

side and outside the sphere is written in terms of Legendre polynomials $P_n(\cos\theta)$ [100]:

$$\Phi_{in} = \sum_{n=0}^{\infty} A_n r^n P_n(\cos\theta), \tag{23}$$

$$\Phi_{out} = \sum_{n=0}^{\infty} \left(B_n r^n + C_n r^{-n-1} \right) P_n(\cos\theta). \tag{24}$$

The coefficients A_n, B_n, and C_n are determined by the boundary conditions. From Maxwell's equations one infers that at the surface of the sphere, $E_{\parallel}$ and $D_{\perp}$ have to be continuous. For $r \to \infty$, the potential has to generate the field without the influence of the sphere. With these boundary conditions the potentials evaluate to [100]

$$\Phi_{in} = -\frac{3\epsilon_m}{\epsilon + 2\epsilon_m} E_0 r \cos\theta, \tag{25}$$

$$\Phi_{out} = -E_0 r \cos\theta + \frac{\epsilon - \epsilon_m}{\epsilon + 2\epsilon_m} E_0 a^3 \frac{\cos\theta}{r^2}, \tag{26}$$

with ϵ and ϵ_m being the dielectric functions of the metal sphere and the dielectric environment, respectively. The potential inside the sphere is the potential of the incident field modified by the dielectric properties. It is more interesting to interpret the outside potential, which is the sum of the potential of the incident field and that of a static point dipole in the center of the particle. We can write Equation 26 as

$$\Phi_{out} = -E_0 r \cos\theta + \frac{\mathbf{p} \cdot \mathbf{r}}{4\pi\epsilon_0 \epsilon_m r^3}, \tag{27}$$

where we defined the dipole moment $\mathbf{p}$ as

$$\mathbf{p} = 4\pi\epsilon_0\epsilon_m a^3 \frac{\epsilon - \epsilon_m}{\epsilon + 2\epsilon_m}\mathbf{E}_0. \tag{28}$$

With Equation 28 we find the polarizability α via $\mathbf{p} = \epsilon_0\epsilon_m\alpha\mathbf{E}_0$, which becomes [91]

$$\alpha = 4\pi a^3 \frac{\epsilon - \epsilon_m}{\epsilon + 2\epsilon_m}. \tag{29}$$

The electric field outside the sphere is calculated by $\mathbf{E}_{out} = -\nabla\Phi_{out}$, which yields

$$\mathbf{E}_{out} = -\nabla\Phi_{out} = \mathbf{E}_0 + \frac{3\hat{\mathbf{r}}(\hat{\mathbf{r}}\cdot\mathbf{p}) - \mathbf{p}}{4\pi\epsilon_0\epsilon_m}\frac{1}{r^3}. \tag{30}$$

The second term in Equation 30 is equal to the term in Equation 16, which scales with $1/r^3$ and corresponds to the near-field. It is plotted in Figure 1 (a). Leaving electrostatics and assuming time-varying plane-wave excitation

$$\mathbf{E}(\mathbf{r}, t) = \mathbf{E}_0 e^{-i\omega t}, \tag{31}$$

an oscillating dipole moment at the center of the sphere

$$\mathbf{p}(t) = \epsilon_0\epsilon_m\alpha\mathbf{E}_0 e^{-i\omega t}, \tag{32}$$

is induced, where α is the frequency dependent polarizability in Equation 29. The radiated electric field of this dipole (see Equation 16) is the scattered field.

2.2.2.2 *Particle plasmon resonance in metallic nanoparticles*

For dielectrics the polarizability varies slowly with a frequency change. In contrast, the real part of the dielectric function of metals, which can be described by the Drude model, is negative below the plasma frequency and allows for the *Fröhlich condition* where the polarizability is resonantly enhanced [91]

$$\mathfrak{Re}\left[\epsilon(\omega)\right] = -2\epsilon_m. \tag{33}$$

For a Drude metal this condition is fulfilled when $\omega = \omega_p/\sqrt{3}$. Absorption in the metal ($\mathfrak{Im}\left[\epsilon(\omega)\right] \neq 0$) limits the magnitude of α. The

physical origin of the resonance is a collective excitation of the conduction electrons associated with a resonantly enhanced dipole moment and scattered dipole fields described by Equation 28 and Equation 30. It is termed *particle plasmon resonance* or *localized surface plasmon resonance*. From Equation 29 one infers that the radius a of the particle has influence on only the strength of the resonance but not the spectral position. The spectral position of the resonance is solely determined by the dielectric function of the metal and the environment. However, this is only true for very small particles, which can be treated in the quasistatic approximation. For larger particles retardation is not negligible anymore, which leads to a size dependence [98, 101]. We will see later that it is possible to tune the plasmon resonance by changing the shape of the particle.

The resonantly enhanced polarizability at the plasmon resonance comes along with a resonant enhancement of the scattered and absorbed power by the nanoparticle. By calculating the Poynting vector (see Equation 44) the scattering C_{sca} and the absorption C_{abs} cross sections of small particles can be expressed as [91, 98]

$$\begin{aligned} C_{abs} &= k\,\mathfrak{Im}(\alpha) \propto a^3, \\ C_{sca} &= \frac{k^4}{6\pi}|\alpha|^2 \propto a^6, \\ C_{ext} &= C_{sca} + C_{abs}, \end{aligned} \tag{34}$$

with C_{ext} being the extinction cross section. The size of the particle with respect to the incident wavelength a/λ plays a decisive role if the scattering or the absorption is the dominant process. The ratio of C_{sca} and C_{abs} is proportional to $(a/\lambda)^3$. For smaller particles the absorption is dominating and for larger particles the scattering. The orange curve in Figure 4 (a) shows the extinction cross section of a small spherical particle where typical Drude parameters for a metal have been used. It is also shown that an increase of the collision frequency γ leads to a broadening of the resonance and a reduction of the maximum cross section associated with a decrease of the quality factor of the resonance $Q = \omega/\Delta\omega$. Using metals with a lower loss is therefore beneficial in plasmonics, such

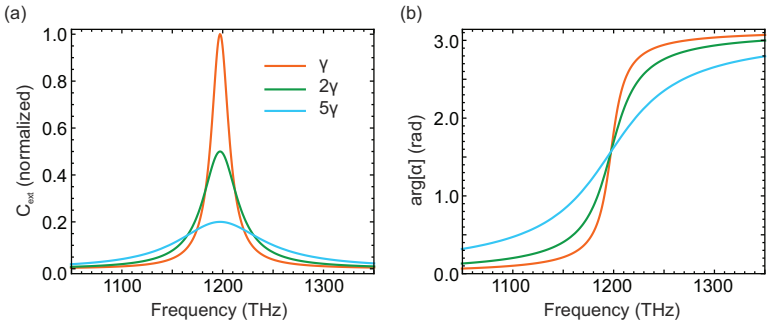

Figure 4: (a) The extinction cross section of a small spherical nanoparticle is plotted. The dielectric function of a Drude metal with $\omega_p = 2074$ THz and $\gamma = 20.78$ THz is used. An increase of the collision frequency γ leads to a damping of the resonance. Similar response is observed in the phase of the polarizability α in (b). At resonance the induced dipole moment is $90°$ out of phase with the incident field.

as using silver instead of gold or using single crystalline metal instead an evaporated one [102, 103]. Recently, it has also been shown that the thickness of the adhesion layer of chromium or titanium below the plasmonic structure has a nonnegligible impact on the scattering performance of the nanostructures [104]. This has to be considered when using top-down fabrication methods, which usually require an adhesion layer (see Section 3.2).

In Figure 4 (b) the phase of the polarizability α for the different collision frequencies is plotted. The extinction cross section as well as the associated phase as a function of frequency shows similar behavior as the amplitude and phase of a damped harmonic oscillator, which is driven by an external force. The question arises if the model of a damped harmonic oscillator can be used to describe the optical responses of small plasmonic particles. The restoring force results from the displacement of the negatively charged electron cloud with respect to the fixed positive metal ions in the finite sized particle when an external electric field is applied. By adding a term of the restoring force to Equation 17 one obtains the equation of motion of the driven damped harmonic oscillator.

This simple model has been used in several works to describe the optical response of plasmonic structures [105] and is especially insightful to describe the coupling between multiple plasmonic resonators [106–109] or even the nonlinear optical response of plasmonic nanostructures [110–112].

2.2.2.3 *Spectral tuning of the particle plasmon resonance*

As we saw in the previous section, the spectral position of resonant light scattering of small spherical particles does not depend on the particle size in the electrostatic approximation. The quasistatic approximation can also be applied to ellipsoid particles. In this case the spectral position of resonant light scattering changes when the aspect ratio of the nanoparticle is changed.

An ellipsoid is described by the equation

$$\frac{x^2}{a_x^2} + \frac{y^2}{a_y^2} + \frac{z^2}{a_z^2} = 1, \tag{35}$$

where $a_i (i = x, y, z)$ is the semiaxis along coordinate i. For such particles the Laplace equation can be solved analytically in ellipsoidal coordinates and the polarizability for incident light polarized along the coordinate axis i becomes [98]

$$\alpha_i = 4\pi a_x a_y a_z \frac{\epsilon - \epsilon_m}{3\epsilon_m + 3L_i(\epsilon - \epsilon_m)}. \tag{36}$$

L_i accounts for the ellipsoidal shape of the particle via

$$L_i = \frac{a_x a_y a_z}{2} \int_0^\infty \frac{dq}{(a_i^2 + q)\sqrt{(a_x^2 + q)\left(a_y^2 + q\right)(a_z^2 + q)}}. \tag{37}$$

The resonance condition in Equation 33 is now modified due to the geometrical shape, which in this case becomes

$$\mathfrak{Re}(\epsilon) = \epsilon_m \left(1 - \frac{1}{L_i}\right). \tag{38}$$

Consequently, the resonances can be tuned by changing the shape of the particle. We will limit our analysis here to the change of a_z, leaving a_x

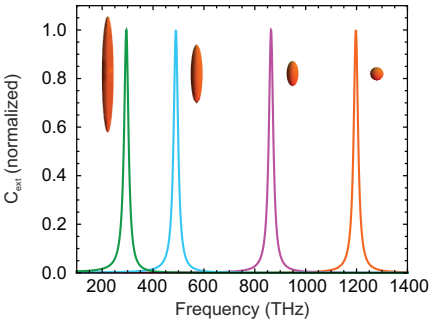

Figure 5: The extinction cross sections of ellipsoidal particles are plotted for the polarization along the long-axis of the particles (z-axis). Compared to a sphere (orange curve) the resonance is red-shifting for increasing aspect ratio $a_z/a_{x,y}$. The insets next to the curves show the respective ellipsoids with aspect ratio $1, 2, 5$ and 10.

and a_y fixed, so that the particle becomes elongated along the z-direction with a circular cross section (prolate spheroid). In Figure 5 we plot the extinction cross section of ellipsoidal particles where the polarization is along the long-axis of the particle.

2.2.3 *Plasmon damping*

As briefly mentioned in the previous section, the spectral response of a particle plasmon resonance can be described with the equation of motion of a damped harmonic oscillator. We stay in this picture to analyze the spectral width of the damped system. The temporal evolution of the amplitude of a damped harmonic oscillator is

$$A(t) = A_0 e^{-t/T} e^{-i\omega_0 t}. \tag{39}$$

The oscillation with eigenfrequency ω_0 is plotted in Figure 6 (a) for two different values of the decay times T. In the spectral domain the

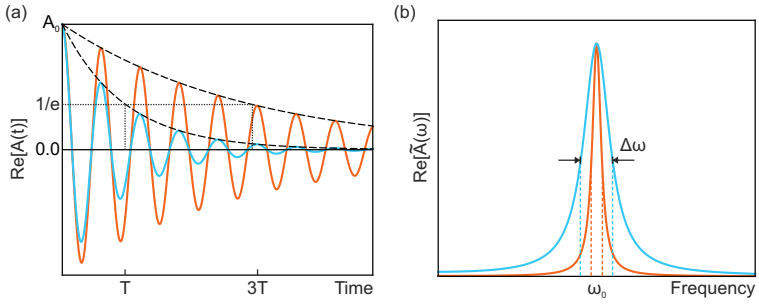

Figure 6: (a) Oscillation of a damped harmonic oscillator for two different values of the decay times T. (b) Normalized amplitude in the spectral domain for the two damped oscillations of (a). $\Delta\omega$ is the FWHM of the resonance. Adapted from [113].

Fourier transformation yields a Lorentzian lineshape of the spectral amplitude [113]

$$\mathfrak{Re}\left[\tilde{A}(\omega)\right] = \mathfrak{Re}\left\{\mathfrak{F}[A(t)]\right\} = \frac{A_0}{\sqrt{2\pi}} \frac{1/T}{1/T^2 + (\omega - \omega_0)^2}. \tag{40}$$

This amplitude is shown in Figure 6 (b) where the FWHM $\Delta\omega$ is seen to depend on the decay time and thus also on the damping of the oscillation. Such a dependency is expressed in the following relation

$$\Delta\omega = \frac{2}{T}. \tag{41}$$

A broad spectrum stems from a strong damping of the oscillating system. In a plasmonic system the damping may originate from different physical effects, which have different time scales [114]. The total dephasing time is denoted T_2 and can be divided into an inelastic decay time T_1 associated with energy loss and an elastic dephasing time T^*, which accounts for loss of coherence when electrons are scattered by other electrons, phonons in the lattice, holes, or scattered at the surface [114]. The total dephasing time then becomes [114, 115]

$$\frac{1}{T_2} = \frac{1}{2T_1} + \frac{1}{T^*}. \tag{42}$$

In plasmonic systems, T_2 is on the order of 10 fs. The inelastic decay can be further split into a radiative part and a non-radiative part from which we can define the radiative efficiency [115]

$$\eta_{ant} = \frac{1/T_{1,r}}{1/T_{1,r} + 1/T_{1,nr}}. \tag{43}$$

This formula of the radiative efficiency of resonant plasmonic structures (antennas) is similar to the quantum efficiency defined for fluorescent dye molecules in Equation 90. Here, in the case of plasmonic antennas, the non-radiative energy loss is due to the intraband and interband excitations [91, 115]. Shifting the plasmon resonance red, the interband contribution becomes weaker (see Figure 2). The red-shift can be achieved, as we have seen previously, with elongated particles with high aspect ratio (Figure 5). Keeping the particle volume small at the same time results in suppression of the radiative decay. Under these conditions a significant increase of the plasmon decay time is achieved [115]. This is beneficial for sensing applications where high-Q resonators and subwavelength field confinement are necessary [69]. As a further step, we will see in Chapter 5 that the coupling of a bright and a dark plasmonic resonator can lead to very narrow spectral linewidths associated with high near-field intensities, which is highly interesting to be used in sensing [116].

2.3 THEORY OF RADIOFREQUENCY ANTENNA ARRAYS

Here, we will briefly review concepts of antenna arrays. They are used for a plethora of applications, such as TV and radio broadcasting, cellular network, and satellite communication. Antenna arrays provide directional emission and reception.

An intriguing concept is beamsteering, which can be achieved by phasing the antenna array in a specific fashion, generally termed as *phased arrays*. The phased arrays allow to emit radiation into variable directions without changing the geometry of the array. The radiation direction is altered by tuning the phase of the feeding current in the individual antenna elements.

Bringing the concept of phased array to the optical frequency region and to the nanoscale resolves the challenge of long-distant signal transmission and reception and, at the same time, of efficient signal transfer to and from nanoscale components, such as integrated electronics. The realization of beamsteering will have important applications in on-chip and chip-to-chip communication in future integrated optical systems.

The introduction to RF antenna arrays is based on my book chapter on optical antenna arrays (Ref. [78]).

2.3.1 *Shaping the radiation pattern with a linear chain of emitters*

The emitted or received intensity by an antenna or an antenna array as a function of the direction of the transmitted or incident wave is defined as its *radiation pattern*. The radiation patterns of transmission and reception are the same. Therefore, we will discuss only the emission pattern in the following. The electromagnetic fields can be calculated using the Green's function and the current distribution (see Equation 13). From the electromagnetic fields the time-averaged *Poynting vector* is obtained as

$$\langle \mathbf{S} \rangle = \frac{1}{2} \mathfrak{Re}(\mathbf{E} \times \mathbf{H}^*), \tag{44}$$

which gives the time-averaged radiated power P in a certain direction specified by the spherical angles ϕ and θ

$$P(\phi, \theta) = \langle \mathbf{S}(\phi, \theta) \rangle \cdot d\mathbf{A}. \tag{45}$$

This is a very general approach to calculate the radiation pattern. But if an antenna has a complicated current distribution or if there are multiple radiation sources, it will be a cumbersome task to carry out such a calculation. For antenna arrays with periodic configuration a significant simplification can be applied by introducing the array factor. The general emission pattern can then be calculated from the emission pattern of the individual antenna element and the array factor, which reduces the complexity tremendously.

As an example, we consider an N-element array of dipoles [see Figure 7 (a)]. We assume that the amplitude of the currents in the individual elements and the distance a between them are uniform across the array. Also sketched is the radiated field pattern of a single dipole source oscillating out of plane. It generates an isotropic emission in the plane of the array. Let us consider a phase difference of α between the neighboring

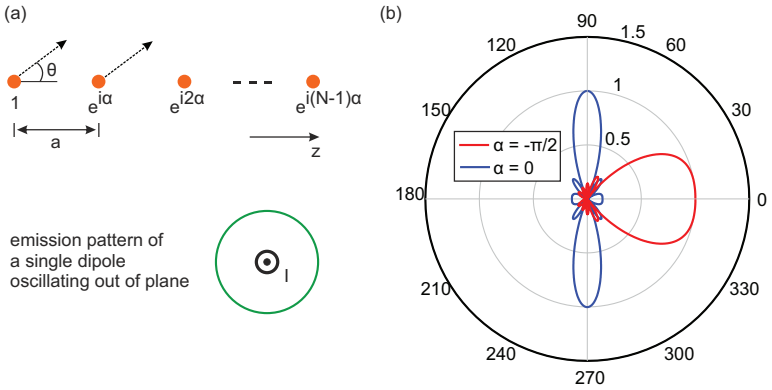

Figure 7: (a) Array of N point dipoles with a distance a between adjacent elements and which oscillate with a phase difference α. θ is the direction of observation (upper panel). The current is oscillating out of plane, which results in an isotropic radiation in the plane of the array (lower panel). (b) Normalized emission patterns of a 10-array with distance $a = \lambda/4$ with the phase shift $\alpha = -\pi/2$ (red curve) and no phase shift (blue curve). Adapted from [78].

elements. The total field in the direction θ is

$$\mathbf{E}(\theta) = \mathbf{E}_0(\theta)(1 + e^{ika\cos\theta + i\alpha} + e^{ik2a\cos\theta + i2\alpha} + \dots + e^{ik(N-1)a\cos\theta + i(N-1)\alpha}) \tag{46}$$

where the exponential term accounts for the phase shift due to the spatial position and the phase difference and k is the wavenumber. $\mathbf{E}_0(\theta)$ is the radiated field of an individual dipole antenna. In Figure 7 (b) it is shown that an induced phase shift can change the emission direction from perpendicular to the array axis to parallel to the array axis.

The second factor in Equation 46 is the radiation pattern of isotropically radiating elements. It is called *array factor* $\Delta(\theta)$ and accounts for properties of the array geometry. It can be expressed as [117]:

$$\begin{aligned}\Delta(\theta) &= 1 + e^{i\Psi} + e^{2i\Psi} + \ldots + e^{i(N-1)\Psi} = \sum_{n=0}^{N-1} e^{in\Psi} \\ &= \frac{1 - e^{iN\Psi}}{1 - e^{i\Psi}},\end{aligned} \tag{47}$$

where $\Psi = ka\cos\theta + \alpha$ is the sum of the phase difference caused by the difference in the radiation paths from the antenna elements to the far-field and the phase difference α between adjacent antenna elements.

As a consequence the overall field pattern of an antenna array $\Gamma(\theta)$ can be written as the product of the individual element pattern $\delta(\theta)$ and the array factor $\Delta(\theta)$

$$\Gamma(\theta) = \Delta(\theta) \times \delta(\theta) \tag{48}$$

We have therefore a control on the radiation pattern by changing the spacing between adjacent elements or, more conveniently, by changing α, the phase difference between them.

In Figure 8 we investigate the case when the single antenna element is a dipole, which oscillates in the plane of the array. While the array factor for this excitation is the same as in the out of plane case (Figure 7), the emission pattern of the individual element is not isotropic anymore but the dipole radiates along the array axis as shown in the lower part of Figure 8 (a). The emission patterns for $\alpha = -\pi/2$ in Figure 8 (b) and Figure 7 (b) resemble each other. When changing the phase gradually from $\alpha = -\pi/2$ to $\alpha = 0$, the emission along the $\theta = 90°$ direction does not become stronger as one expects from the array factor Δ because the element pattern δ forbids the emission along this direction. The overall radiation becomes weaker because the main lobes of array factor and element pattern point in perpendicular directions.

A maximum of the array factor occurs when $\Psi = ka\cos\theta + \alpha = 0$. For example, to achieve maximum radiation along the chain ($\theta = 0°$) for a fixed distance $a = \lambda/4$, the following phase shift α has to be induced:

$$\Psi = ka\cos\theta + \alpha|_{\theta=0°} = ka + \alpha = 0 \quad \rightarrow \quad \alpha = -\pi/2 \tag{49}$$

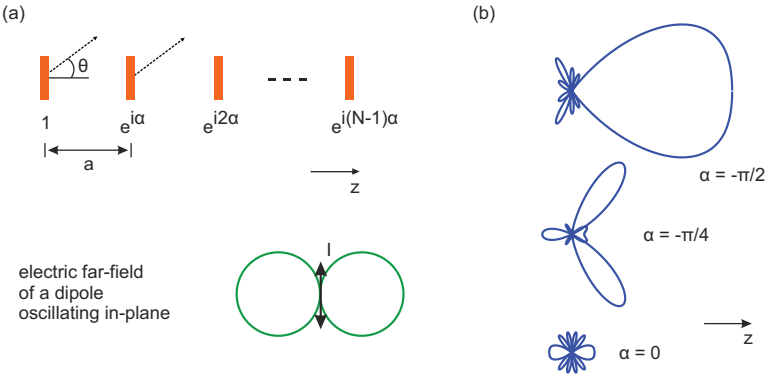

Figure 8: (a) Array of N dipoles with a distance a between adjacent elements oscillating with a phase difference α. The direction of observation is θ. The current I oscillating in-plane radiates an electric field pattern as sketched in the lower part. (b) Emission pattern for a 10 dipole array with a distance $a = \lambda/4$. When changing the phase from $\alpha = -\pi/2$ to $\alpha = 0$ the emission pattern nearly disappears as can be calculated from the product of the array factor with the element pattern. Adapted from [78].

In general, directing the beam in a certain direction can be achieved by fulfilling the condition [118]:

$$\Psi = ka\cos\theta + \alpha|_{\theta=\theta_0} = ka\cos\theta_0 + \alpha = 0 \tag{50}$$

This derivation of the array factor is only valid for uniform spacing between the elements and equal amplitudes of currents in the antenna elements. An example that is not covered is the Yagi-Uda antenna, which is shown in Figure 9. A Yagi-Uda antenna does not have equal amplitudes of currents in the antenna elements with a constant phase shift. It is a linear array of dipoles with different lengths, where only one element, the feed element, is excited by a current source. Due to mutual coupling, currents in the other elements are generated with a defined phase controlled by the lengths and the inter-dipole distances [119]. Nevertheless, the high directivity of a Yagi-Uda antenna stems from the phase difference in the individual elements. The right phase difference leads

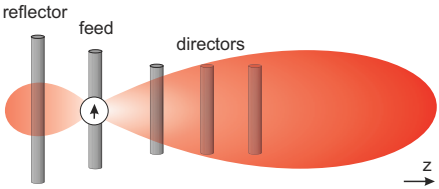

Figure 9: Schematic of a Yagi-Uda antenna. Only the feed element is excited and mutual coupling between the differently sized elements leads to a phase difference, which results in constructive interference along the z-direction.

to constructive interference along the antenna similar to what happens for the linear array with appropriate phasing.

2.3.2 *Phased two-dimensional antenna arrays*

We now investigate two-dimensional (2D) antenna arrays, which provide higher variability in shaping the radiation and receiving pattern. We want to point out that with increasing complexity of the array, engineering an appropriate feeding circuit becomes complicated in the RF regime. In the optical frequency regime where antennas are on the nanoscale, feeding a complex antenna array will be a real challenge. Here, we focus on the radiation pattern with the assumption that we are able to induce phase gradients along the x- and the y-direction.

We consider a rectangular grid of point sources shown in Figure 10 (a) where a, b and α, β are the distances and phase differences along the x, y-direction. The array factor then becomes:

$$\begin{aligned} \Delta(\phi,\theta) &= \sum_{n=0}^{N-1}\left[\sum_{m=0}^{M-1} e^{im\Psi_x}\right] e^{in\Psi_y}, \\ \text{with} \quad \Psi_x &= ka\sin\theta\cos\phi + \alpha, \\ \text{and} \quad \Psi_y &= kb\sin\theta\sin\phi + \beta. \end{aligned} \tag{51}$$

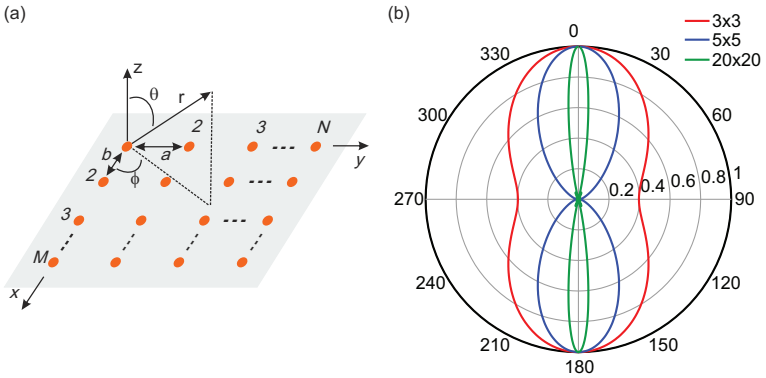

Figure 10: (a) Planar rectangular array of ideal dipoles. (b) Normalized radiated fields for a 3×3 (red curve), 5×5 (blue curve) and 20×20 array (green curve). The distance is fixed as $\lambda/4$ in x- and y-direction. Adapted from [78].

For uniform distances a and b, the maximum radiation in the direction θ_0 and ϕ_0 can be adjusted by imposing the following phase shifts

$$\alpha = -ka \sin\theta_0 \cos\phi_0,$$
$$\beta = -kb \sin\theta_0 \sin\phi_0. \tag{52}$$

Figure 11 shows the radiation properties of a square array (when distance between the elements is $\lambda/4$), where the elements are excited with phase shifts in the x- and y-direction according to Equation 52. We have shown only the pattern of the array factor when each element is an isotropic point source. For different elements, such as a dipole antennas, the total field can be easily obtained by multiplying the element pattern with the array factor as shown for the linear antenna array in Equation 48.

2.3.3 *Enhancing the directivity*

An antenna array can be used to enhance the directivity. Figure 10 (b) compares the radiation patterns of a 3×3 array (red curve), a 5×5 array

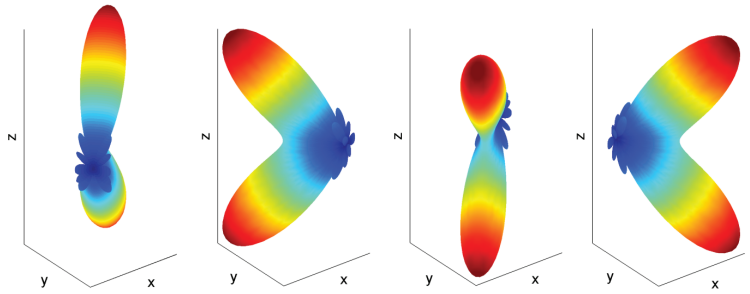

Figure 11: Three-dimensional radiation patterns of a planar 10×10 phased array. The distance between adjacent emitters in both directions is $\lambda/4$: (a) phase-shift in x/y-direction $-\pi/4$, (b) phase-shift in x-direction $\pi/4$, phase-shift in y-direction $-\pi/4$, (c) phase-shift in x/y-direction $\pi/4$, (d) phase-shift in x-direction $-\pi/4$, phase-shift in y-direction $\pi/4$. Adapted from [78].

(blue curve), and a 20×20 array (green curve). With more radiation elements, the main lobe of the radiation pattern becomes narrower. In order to quantify the radiation in a certain direction, the quantity of directivity D is introduced

$$D(\phi, \theta) = 4\pi \frac{P(\phi, \theta)}{\int P(\phi, \theta) d\Omega} \tag{53}$$

which is the power $P(\phi, \theta)$ emitted in a given direction divided by the emitted power of an isotropic point source with same total radiated power. This thesis deals with single optical nanoantennas as well as optical nanoantenna arrays, with which high directivities and beamsteering in the optical frequency regime is demonstrated.

3

METHODS

A short overview is given here on the procedures used to design, fabricate, and measure optical antennas. The optical response of the plasmonic nanostructures in this thesis is numerically evaluated with CST - Computer Simulation Technology (CST). The fabrication is done in cleanroom facilities using electron beam lithography (EBL). For the optical characterization of the structures FTIR spectroscopy is used which works from the visible to the far-infrared region and will be shortly introduced here.

3.1 NUMERICAL CALCULATIONS

Maxwell's equations have to be solved in order to compute the spectral response of our plasmonic nanoantennas. Going beyond simple shapes, such as spheres or ellipsoids, a numerical evaluation on a mesh grid is necessary. This is implemented in the commercially available CST[1] which is used for the design of the nanoantennas. The structure is defined in a graphical user interface where an automated mesh generation is performed. An adaptive meshing routine and the tetrahedral mesh allow for accurate discretization of the actual geometry, especially at the boundaries of the structure. The discretized problem is then solved numerically where the accuracy is given by the resolution of the mesh. We use throughout this thesis the *frequency domain solver* which allows for periodic boundary conditions as well as far-field calculations of the cross sections. A time-harmonic field is assumed while the equation system is solved for different frequency samples which are usually chosen automatically by the solver until the convergence criterion is met.

1 CST AG, Germany

3.2 NANOFABRICATION

All the nanostructures investigated in this thesis were fabricated using EBL. Different EBL processes can be categorized in two types depending on the resist that is used.

The first uses the positive resist which is the standard resist used in this thesis to fabricate the gold nanoantennas. The individual processing steps are shown in Figure 12. The actual resist we use is polymethylmethacrylat (PMMA) which is a polymer dissolved at different chain lengths in chlorobenzene. The chain length determines the sensitivity of the resist upon electron exposure. A thin layer of PMMA is spin-coated on top of a substrate. The concentration of PMMA in the solvent and the spinning speed are used to control the thickness of the polymer-layer. Usually, 950K PMMA at a concentration of 1.5% is spin-coated (5 s at

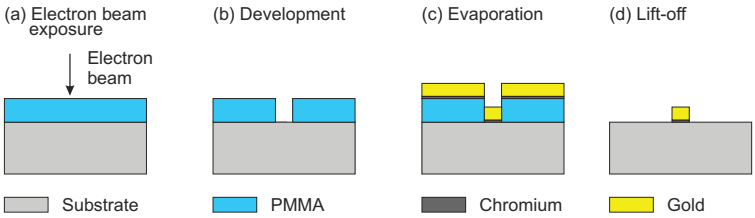

Figure 12: The individual steps to fabricate plasmonic nanostructures with EBL are shown. The exposure (a) is followed by (b) development. (c) A thin adhesion layer of chromium is evaporated before the gold. (d) Final lift-off dissolves the unexposed resist with gold on top and the nanostructure is obtained.

3000 rpm and 30 s at 8000 rpm), which results in a 60 nm thick smooth layer. The sample is baked afterward at 160°C for 5 min. A mask is defined in this layer after the development and before the evaporation of the metal. In order to facilitate the lift-off, a 200K PMMA at 3.5% can be spin-coated below the 950K PMMA layer, which gives a 140 nm thick layer. This layer is more sensitive to electron exposure and yields an undercut after development. In order to avoid charging of the sample

during exposure, the conductive polymer *Espacer 300Z* is spin-coated for 60 s at 5000 rpm. Connecting the sample surface with the sample holder of the EBL machine avoids unwanted charging of the sample.

For the exposure, the electron acceleration is usually set to 20 kV and different apertures of 10 μm and 20 μm are used, which yield a writing current of around 40 pA and 120 pA, respectively. The area dose is typically set to 325 $\mu C/cm^2$. Before exposure, the focus of the electron-beam has to be adjusted. The best way to adjust the focus is by *burning* a spot, which means that a high dose is applied at one location. This yields the point-spread function (PSF) of the system which has to be optimized. When writing with a high-resolution the beam can be scanned over an area of 100×100 μm^2 without moving the sample stage. This area is called a *write-field*. The deflection of the beam has to be aligned to the coordinate system of the laser interferometer stage where the sample is mounted. This is done by moving the stage by about 40 μm from the center to three different corners of the write-field and deflecting the beam back to the center which can be then adjusted by the user.

After exposure the *Espacer* is removed by dipping the sample into water for a few seconds. The sample is then developed in Methyl isobutyl ketone (MIBK) (diluted 1:3 in propanol) a certain amount of time depending on the thickness of the PMMA layer (90 s for a 200 nm thickness). The development yields the pattern in the resist and the sample is ready to be loaded in an evaporation machine. There, a thin adhesion layer of Chromium (typically 2 nm) is evaporated followed by the deposition of gold. The final step is the lift-off where the extra gold is removed and the final structure is obtained. Lift-off is usually done in warm (65°C) N-Ethyl-2-pyrrolidone (NEP) for 2 hours. Subsequent rinsing in acetone and propanol guarantees that all the extra gold is washed away from the sample surface.

The second type of EBL process uses the negative resist. In contrast to the positive resist, it yields a *negative* mask after development. This means that instead of the exposed area the rest is removed. In this thesis we use two different kinds of negative resist, hydrogen silsesquiox-

ane (HSQ)[2] and ARN[3]. They are used to define nanosized vibrational or fluorescent probes positioned at defined locations in the vicinity of plasmonic nanoantennas. Details of the fabrication of these samples are given in Chapter 5 and Chapter 6. The positioning is done in a second EBL step, where an accurate alignment is crucial. This procedure is also used to fabricate 3D antenna structures in a layer-by-layer process which is discussed as follows.

The layer-by-layer stacking procedure is shown in Figure 13. The fabrication of each layer follows the process described before. In the first layer, gold alignment marks are fabricated in addition to the antenna structures. *PC403* is spin-coated as a spacer layer (5 s at 2000 rpm and 20 s at 4000 rpm). At least three gold crosses with the size of several tens of micrometers are positioned around the write-field and, for the sake of fine alignment, at least three smaller markers (size of around 1 µm) are fabricated in the corners of the write-field. The larger gold

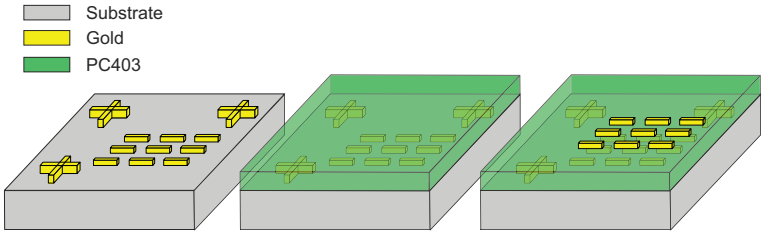

Figure 13: The layer-by-layer fabrication steps to obtain 3D nanostructures are shown. After the first layer, the spacer layer (PC403) is spin-coated, which serves as the sample surface for the second layer. Alignment markers from the first layer are used to align the coordinate system of the first and second layer. 10 nm positioning accuracy of the second layer with respect to the first layer can be achieved with this technique.

crosses serve for a rough alignment of the sample coordinate system to the stage coordinate system, correcting for translation and rotation. After this first alignment step, the stage can be moved to the coordinates of

2 Dow Corning, USA
3 Allresist GmbH, Germany

the write-field. By scanning the write-field markers without moving the stage but deflecting the beam, the beam coordinate system is aligned to the sample coordinate system. This procedure allows a positioning accuracy of around 10 nm and is repeated until the final layer number is reached. Spacer layers are deposited between the adjacent layers of EBL structures. In a multi-layer structure with thick spacer layers, such as the one realized in [120], the scattering signal from the electrons by the deeply buried markers might be too weak for the alignment procedure when fabricating the top layers. Therefore, the alignment markers can be repeated in each layer, although the systematic errors add up from layer to layer.

3.3 FTIR SPECTROSCOPY

Spectra of transmittance and reflectance are measured using a FTIR spectrometer (Bruker Vertex 80[4]). It is equipped with a microscope (Hyperion), which allows to measure areas with the size of the write-fields or even smaller areas. The microscope has a 15× Cassegrain objective with a 0.4 NA and two knife-edge apertures define the measured areas. Spectra can be taken from the visible to the far-infrared region by using different detectors (Si photodiode, InGaAs photodiode, and nitrogen-cooled MCT detector). The mirrors in the interferometer are scanned with kHz frequencies. In the visible and near-infrared region a tungsten lamp is used as a light source and in the far-infrared a thermal light-source (globar) is used. A linear polarizer is inserted into the beam path to control the incident polarization. The spectrum taken on the write-field is divided by a reference spectrum which is acquired next to the field or on a gold mirror, yielding the transmittance or the reflectance spectrum, respectively.

4 Bruker Optik GmbH, Germany

4

DIRECTIONAL RECEIVING OF LIGHT WITH YAGI-UDA NANOANTENNAS

4.1 INTRODUCTION

An interesting antenna geometry is the *Yagi-Uda* antenna (Figure 14) due to its directive properties [119]. It is unidirectional, which means that the emitted radiation has a strong preference of one direction. This is because of constructive interference in one direction and destructive interference in the other directions. The interferences are achieved by arraying dipoles of different lengths with sub-wavelength distance. The mutual coupling between the elements determines the phase distribution across the elements, which results in a directional radiation pattern. The antenna contains one active element, usually one long element and several shorter elements. The shorter elements are termed directors, the active element is the feed element, and the long element is the reflector. The feed element is in resonance with the radiation field. In terms of the circuit theory, the directors are blue detuned and couple capacitively to the radiation field and the reflector is red detuned and couples inductively. They therefore exhibit a negative and a positive phase shift of the current, respectively.

Bringing this antenna geometry to the optical regime is an intriguing idea because plasmonic modes will be excited inside the antenna. The plasmonic modes will be confined in a deep sub-wavelength volume and can thus enhance the light-matter interaction dictated by the directive properties of the radiation pattern [29–32]. This is shown in Figure 14 (b). The Yagi-Uda geometry is easy to fabricate using conventional EBL fabrication technique. For achieving directive radiation at optical frequencies, the challenge is to drive exclusively the feed element so that the Yagi-Uda antenna works. Recently, directive radiation from

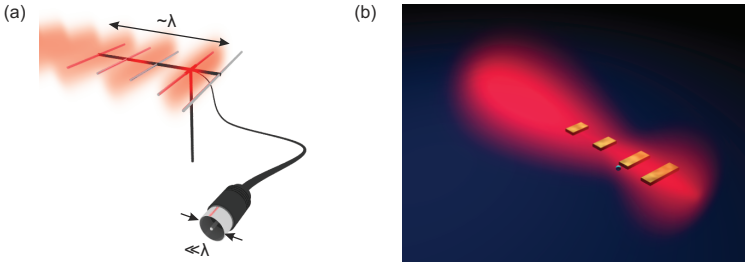

Figure 14: Yagi-Uda antennas in the RF regime (a) and in the optical frequency range (b). Consisting of multiple dipoles of different lengths, the Yagi-Uda antennas can achieve directional radiation or receiving. The feeding point at the resonant antenna element (feed element) is deeply sub-wavelength, which enables enhanced light-matter interaction of nanoscopic objects and the realization of directive single photon sources in the optical regime. Adapted from [121].

optical Yagi-Uda nanoantennas was demonstrated by controlling the incident polarization [33], positioning a single quantum dot at the feeding point [85], or using the electron beam in cathodoluminescence (CL) to excite only the feed element [34]. These experimental studies investigated the transmitting properties of optical Yagi-Uda nanoantennas.

In this chapter, we want to focus on the receiving properties of single 2D optical Yagi-Uda antennas and 3D optical Yagi-Uda nanoantenna arrays. Parts of the concepts presented here about the 3D Yagi-Uda nanoantenna arrays have been investigated during my diploma thesis [122]. However, with the experimental data of the planar 2D Yagi-Uda nanoantenna obtained during my PhD thesis, we are able to understand the complete picture of the receiving process in the 3D geometry. In addition, new experimental data and analysis on 3D Yagi-Uda antenna array are also presented in this chapter.

The presented results are based on our publications of Ref. [123] and Ref. [124].

4.2 2D SINGLE YAGI-UDA NANOANTENNAS

A planar optical Yagi-Uda antenna is a promising geometry for in-plane directional receiving applications such as signal reception in a plasmonic nanoantenna link which we will elaborate on in Chapter 6. We want to analyze here the receiving properties and the supported antenna modes when the structure is excited from the far-field under certain directions. We use aSNOM, which allows us to assess the phase and the amplitude of the electric field distribution close to the antenna. Figure 15 (a) shows the schematic of the measurement principle. A SEM micrograph of the

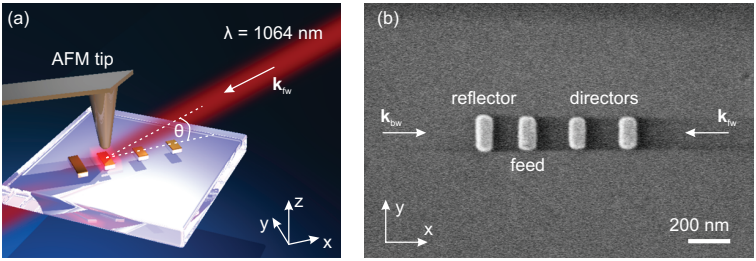

Figure 15: (a) Schematic of the near-field measurement on optical Yagi-Uda antennas. The incident light ($\lambda = 1064$ nm) has an angle of $\theta = 20°$ with respect to the surface of the substrate. The optical near-field signal is picked up by an AFM tip and scattered into the far-field. (b) SEM micrograph of the planar optical Yagi-Uda antenna. Only small length deviations between the reflector, the feed, and the directors lead to optimal directivity. $\mathbf{k}_{fw}$ and $\mathbf{k}_{bw}$ are the wavevectors impinging from the side of the directors (forward direction) or reflectors (backward direction), respectively.

optical Yagi-Uda nanoantenna is shown in Figure 15 (b), which has been fabricated using standard EBL process (see Section 3.2). The antenna consists of a resonant feed element, which is positioned between a slightly longer reflector and two slightly shorter directors. The arrows in Figure 15 (b) indicate the wavevectors $\mathbf{k}_{fw}$ for forward (from the director side) incident radiation and $\mathbf{k}_{bw}$ for backward (from the reflector side) incident radiation. The height of the structure is 30 nm and the nominal

width of the elements is 80 nm, with a nominal length of 229 nm, 198 nm and 168 nm for the reflector, feed and directors, respectively. In this case the antenna is resonant at the incident wavelength $\lambda = 1064$ nm. The distance between the feed element and the reflector is 210 nm and the distances between the other elements are 270 nm. We fabricate antennas with different sizes by changing the length of all elements in 10 nm steps.

We excite the antenna structure, which is fabricated on a glass substrate ($n = 1.46$) from the air side with an angle of $\theta = 20^\circ$ between the substrate surface and the incident beam. The incident light is polarized along the long-axis of the antenna elements (y-polarization). An AFM-tip close to the antenna structure picks up the vertical near-field component and scatters it back to the far-field where the detector is placed [66, 125, 126]. The tip radius is typically around 10 nm, which defines the imaging resolution. Raster-scanning the tip over the whole antenna structure gives a complete near-field map. Mixing the back-scattered signal with a reference beam allows in addition to the amplitude measurement also the phase measurement of the electric near-field.

We use numerical simulations to design the Yagi-Uda nanoantenna and to support our experimental findings. We take into account the substrate as well as the oblique incidence in the aSNOM setup. The material properties of gold are described by the Drude model using the parameters $\omega_{pl} = 1.37 \times 10^{16}$ rad/s, $\gamma = 1.2 \times 10^{14}$ rad/s.

4.2.1 *Radiation pattern of planar Yagi-Uda antennas on a glass substrate*

The far-field of a dipole emitter close to the interface of two media is mostly emitted into the optically denser medium [53]. For optical Yagi-Uda antennas the forward/backward ratio is maintained even though the main lobe is deflected into the glass substrate [85]. Since we have only access to the upper half-space of air in our experimental setup [see Figure 15 (a)], we have to make sure that the directive properties of the Yagi-Uda nanoantenna are preserved in the air halfspace and can hence be measured with aSNOM. We therefore determine the radiation

pattern of our optical Yagi-Uda antenna. In numerical simulations we excite the feed element with a dipole emitter at $\lambda = 1064$ and extract the phase and the amplitude of the current densities in the individual antenna elements. It allows us to calculate the far-field response by replacing the antenna elements with single dipoles with the respective phase and amplitude distributions on top of a dielectric half-space with $n = 1.5$ [53].

In Figure 16 (a) we show the vertical cut (xz-plane) of the calculated emission pattern for the Yagi-Uda antenna oriented along the x-direction. Most of the radiation goes into the glass substrate but a directive radiation pattern is maintained in air. In Figure 16 (b) we plot the 3D radiation pattern in the air half-space illustrating a directive emission along the antenna axis into the direction of the directors (positive x-direction). The cone with an opening angle of 140° indicates the accessible wavevectors in our experiment decided by the oblique incident light. We expect to observe the same receiving pattern as in the transmitting mode. We check this assumption in numerical simulations where we simulate plane waves incident onto the Yagi-Uda nanoantenna from directions on the cone. We calculate the receiving pattern by extracting the electrical near-field at the position where the dipole emitter is in the transmitting mode [blue dots in panel (c)]. We observe very good agreement between the receiving pattern and the conical cut of the emission pattern (red curve). Both show strong directivity in the forward direction. Therefore, we expect to observe the directivity of the optical Yagi-Uda antenna by measuring a strong near-field enhancement at the feed-element for incident light from the director side.

4.2.2 *Optical near-field measurement of planar Yagi-Uda nanoantennas*

We investigate the near-field distributions of optical Yagi-Uda nanoantennas. We tune their resonance by changing the size of the individual elements. Figure 17 shows the near-field amplitude for a Yagi-Uda antenna resonant to the incident wavelength $\lambda = 1064$ nm (center), compared to a blue-detuned (left) and a red-detuned (right) antenna. We

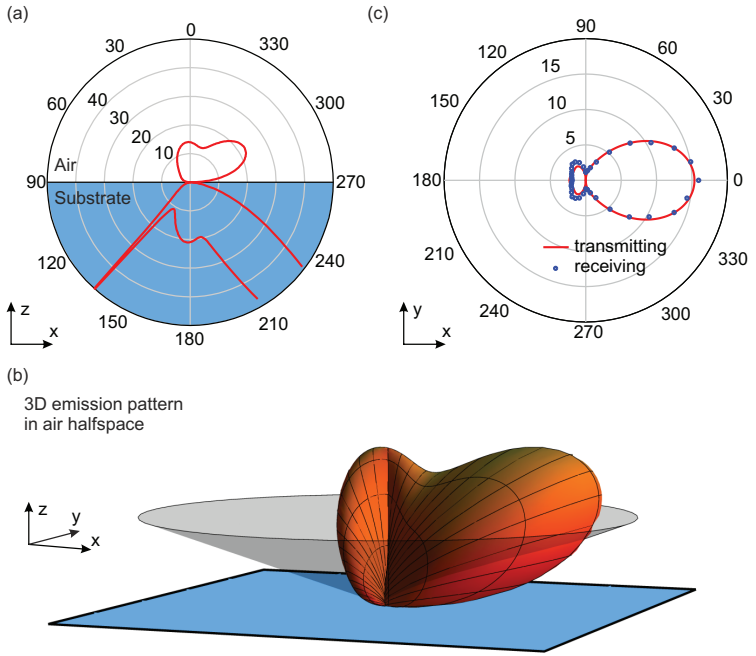

Figure 16: Calculated emission pattern of the planar Yagi-Uda nanoantenna on a glass substrate. (a) Sideview showing the radiation pattern in the upper (air) and lower (glass) half-spaces (xz-plane). (b) 3D radiation pattern in the air half-space where the cone indicates the incident wavevectors in the aSNOM setup ($\theta = 20°$). (c) Calculated emission pattern (red) compared to receiving pattern (blue) for the accessible wavevectors on the surface of the cone as shown in (b). The receiving pattern is obtained by calculating the near-field enhancement at the feed element (load) as a function of the incident angle. It demonstrates higher directivity for the positive x-direction. Adapted from [123].

excite the antennas from the forward direction inducing a phase retardation of the plasmon oscillation from the directors to the reflector. Despite the small length variations of only 10 nm, a pronounced difference in the near-field amplitude is observed. For the blue detuned antenna, the reflector shows a strong near-field response besides the feed element. In the case of the resonant antenna, the near-field enhancement occurs

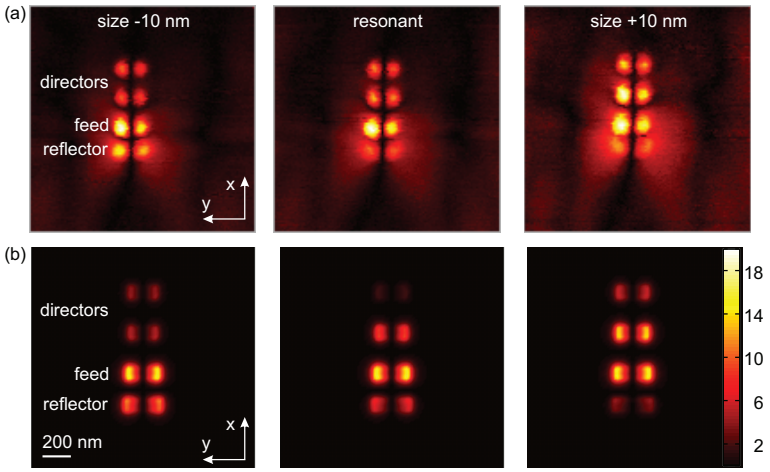

Figure 17: (a) Amplitude measurements of the near-field distribution around Yagi-Uda nanoantennas for forward incident light when blue detuned (left), in resonance (center), and red detuned (right). A field-concentration to the feed-element is observed when the antenna is in resonance with the incident wave from the forward direction. (b) Corresponding simulations of the electric-field amplitude on the plane 5 nm above the antenna.

solely at the feed element. Increasing the size of the antenna further shifts the confined near-field to the first director. One might suggest that this is purely due to the individual plasmon oscillations tuned in resonance with the fixed incident wavelength, i.e., either the reflector, the feed or the directors are in resonance by increasing the antenna size. But in the case of the resonant antenna and better visible in the case of the red detuned antenna, the first director is brighter than the second director even though they are equal in length. It indicates that there is a strong mutual coupling between the elements besides the direct far-field excitation. This observation is supported by near-field simulations from which we can extract the near-field amplitude.

In order to investigate the near-field coupling further, we plot in Figure 18 the phase of the near-field distributions for the resonant antenna

and the detuned antennas, where we change the lengths of the elements by 30 nm. The retardation from element to element due to the oblique

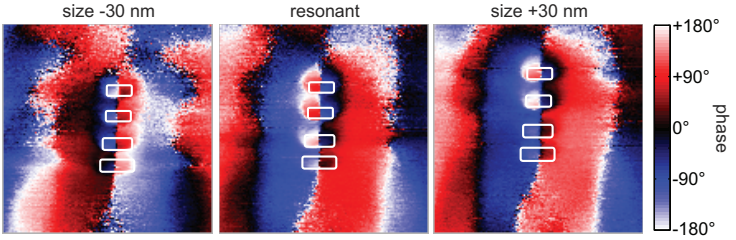

Figure 18: The phase distributions of blue-detuned (left), resonant (center) and red-detuned (right) optical Yagi-Uda antennas are shown for forward incident light. In the resonant case, a phase difference of the feed element compared with the directors and the reflector is observed. For the other two cases the feed element is in phase with the directors (blue detuned antenna) and with the reflector (red detuned antenna), respectively.

incidence is subtracted. The phase images therefore give us the information how the individual elements couple to the surrounding electric field not including the retarded phase of the incident light. For the smaller antenna (size -30 nm) the two directors are in phase with each other and as well with the feed element. The longer reflector is ahead of them in phase. For this blue detuned antenna with respect to the incident wavelength $\lambda = 1064$ nm the short directors and feed element couple capacitively to the surrounding field whereas the reflector has already picked up some phase since its plasmon resonance frequency is closer to $\lambda = 1064$ nm. In the resonant antenna, both directors are oscillating in phase but are retarded with respect to the feed element. The feed element has itself a phase retardance compared to the reflector. The phase difference between the directors and the reflector reaches nearly 180°, while the feed element has a phase in between the two. Hence, the feed element is in resonance with the surrounding field and the director (reflector) couple capacitively (inductively). For the larger red detuned antenna ($+30$ nm), the reflector and the feed element oscillate in phase

leading the current oscillation in the directors. Similar as in the case of the amplitude measurements, these observations might suggest that simply the length tuning of the individual elements through the resonance leads to these phase distributions and hence near-field concentration at the feed element. However, we will see in the next section that illuminating the sample from the backward direction leads to a complete different near-field response. Such a difference proves that the field distributions do not simply result from the far-field excitation of uncoupled elements.

4.2.3 *Directional receiving with optical Yagi-Uda antennas*

We have seen in the previous section that for the resonant antenna light incident from the forward direction is concentrated to the feed element (see Figure 17). This is associated with a phase retardation of the plasmon oscillation from the reflector to the directors. We now turn our optical Yagi-Uda nanoantenna by 180° so that we illuminate the antenna from the backward direction. Figure 19 shows a comparison between the near-field amplitudes for forward and backward incident light. The forward and the backward incidences result in completely different near-field amplitudes. Therefore, the field distributions cannot be explained with purely length tuning of the different elements. The difference in the excitation phase due to the opposite illumination directions and mutual coupling between the elements is the reason for the different near-field responses. Upon forward illumination, the scattered fields from the directors and the reflector add up constructively at the feed element. This turns into a destructive interference for backward incident light, suppressing the resonance of the feed element. The differences between the near-field distributions for forward and backward illuminations of the same structure is a clear proof of the antenna directionality. Our experimental observations are in good agreement with numerical simulations, which we plot in the bottom row of Figure 19. Overall the near-field intensity is more homogeneously distributed among all elements for backward incident light.

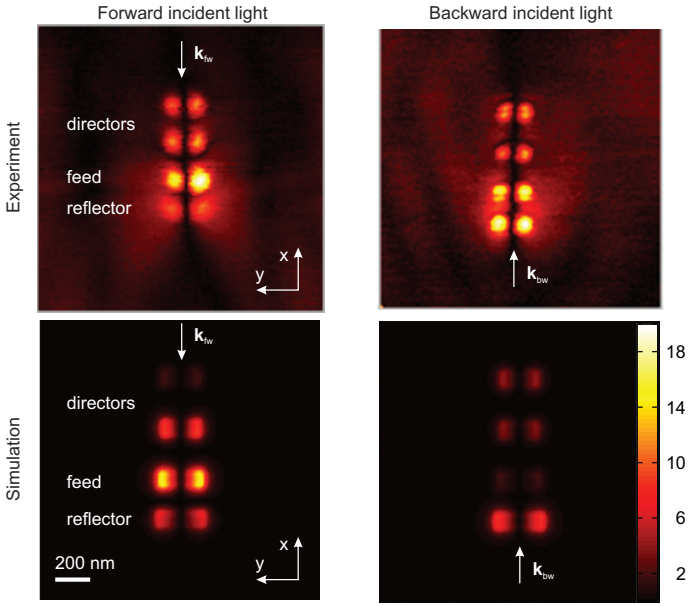

Figure 19: The top row shows the experimental near-field distribution of the resonant optical Yagi-Uda antennas for forward (left) and backward (right) incident light. The energy is confined to the feed element for forward incident light. The bottom row is the respective simulated near-field distribution confirming the directional receiving of optical Yagi-Uda nanoantennas due to higher near-field concentration at the feed element for forward incident light.

In experiment, we have tuned the size of the antennas in and out of resonance for a given incident wavelength, as shown in Figure 17. In simulations, we can analyze the spectral properties for a fixed antenna size. We calculate the near-field component normal to the substrate at the feeding point close to the feed element and show the results in Figure 20. We use the actual geometric parameters of our resonant Yagi-Uda antenna, which we obtain from electron microscopy. Again, we investigate both the cases of the forward (red curve) and the backward (green curve) incident light. A minimum is observed around 1050 nm for the backward incident light, which is a maximum for the forward incident

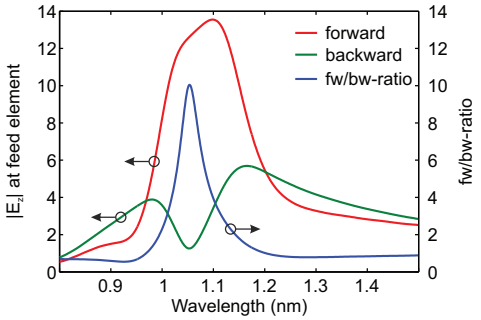

Figure 20: The spectral response of the near-field enhancement at the feed element is shown. At the incident wavelength $\lambda = 1064$ nm the near-field is resonantly enhanced for forward incident light (red curve) compared to backward incident light (green curve). The blue curve is the forward-backward ratio being a maximum around the illumination wavelength.

light. The forward-backward ratio with a peak value of more than 10 shows that we obtain highest asymmetry of the near-field enhancement at about our illumination wavelength.

4.3 3D YAGI-UDA NANOANTENNA ARRAYS

We have seen that the radiation pattern of a planar Yagi-Uda antenna is strongly modified by the presence of the glass substrate. The radiation tends to be deflected into the substrate and it is therefore difficult to make use of the directional properties in practical applications. Here, we demonstrate how to achieve directive radiation out of the substrate plane along the surface normal. We use an array of 3D optical Yagi-Uda antennas, which we fabricate with our EBL stacking technique (see Section 3.2). As in the previous section we investigate the optical properties of the 3D antenna array as a receiver. It is done with conventional FTIR spectroscopy since the forward and the backward directions of the 3D Yagi-Uda antennas are along the optical path of the spectrometer. We

use numerical simulations in order to illustrate the beamsteering out of the substrate plane.

4.3.1 *Directivity enhancement by nanoantenna arrays*

We use a 3D Yagi-Uda antenna with its axis perpendicular to the substrate (along the z-axis, as shown in Figure 21). Besides maximal directivity out of the substrate plane, the 3D geometry allows us to array Yagi-Uda antennas along the other two dimensions so as to realize a 2D antenna array with high directivity and beamsteering along the θ- and φ-direction as introduced in Section 2.3.

In my diploma thesis we investigated the directivity pattern of the antenna array. We used numerical calculations to determine the radiation pattern by exciting the feed element with a dipole emitter with its dipole moment oriented along the feed axis ($\lambda = 1500$ nm) and at a distance of 5 nm. In Figure 21 (a) we plot the simulated radiation pattern of a single gold Yagi-Uda antenna in the xz- (left) and yz-plane (right). The antenna axis is along the z-axis, which is the substrate normal. The antenna consists of three elements: a reflector, a feed and a director. To take into account the dielectric matrix in experiment we set the refractive index of the calculation domain to $n = 1.55$. In Figure 21, we compare the radiation patterns of the Yagi-Uda antennas (colored curves) to the emission patterns of the emitters without antennas (black curves). We optimize the three-element structure to obtain maximum radiation into the positive z-direction (forward direction) by varying the geometrical parameters of the Yagi-Uda antenna. We start from optimizing the feed to maximize the radiated power of the emitter-antenna coupled system. The optimal length of the feed element is found to be 250 nm. In this case the far-field radiation is completely determined by the dipole mode of the plasmon resonance. By adding a slightly longer element below the feed element, the reflector, the symmetry is broken and the directivity along the substrate normal is enhanced. We maximize the directivity by optimizing the length of the reflector and its distance to the feed element. The procedure is repeated for the shorter director, which is placed

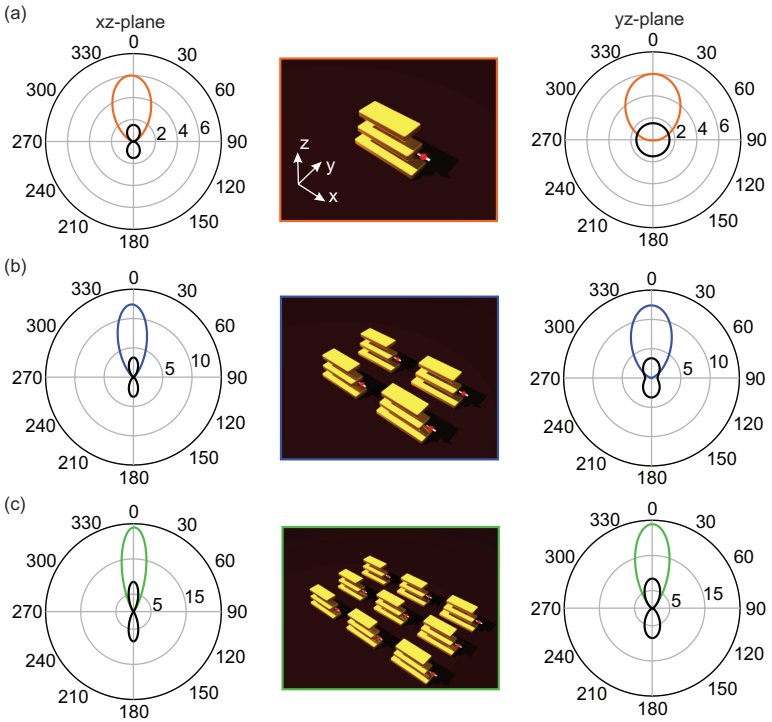

Figure 21: The radiation patterns in the xz- and yz-plane of (a) the single Yagi-Uda antenna , (b) a 2×2 array and (c) a 3×3 array are shown. To each feed element we couple a dipole emitter ($\lambda = 1500$ nm). Increased directivity is observed for increasing array size. Adapted from [124].

above the feed element. The red detuned reflector couples inductively and the blue detuned director couples capacitively to the surrounding field when the feed element is in resonance with the dipole emitter. The induced current distribution across all elements leads to constructive interference of the fields in the positive z-direction (forward direction) and cancels out the radiation in the negative z-direction (backward direction). For the single antenna in Figure 21 (a), a directivity of 6 in the forward direction is observed (orange curves), which is an enhancement

compared to the directivity of the dipole emitter (black curves), which is 1.5.

We now consider a 2D antenna array of 3D Yagi-Uda nanoantennas. In Figure 21 (b) and (c) we show the examples of a 2×2 array and a 3×3 array where each Yagi-Uda antenna is excited by in-phase oscillating dipole emitters. As a reference, we always show in black the directivity patterns of the dipole emitters. The radiation patterns in Figure 21 (b) and (c) illustrate the advantage of higher directivity by using directive antennas in the array. Importantly, the maximal directivity, which is along the z-direction, becomes higher with adding elements to the array. It scales from 6 for the single antenna to about 15 for the 2×2 antenna array and reaches almost 25 for the 3×3 antenna array.

We want to note here that these directivities are obtained by coupling the antenna structures to the dipole emitters that oscillate all in phase. A phase-stable feeding circuit for nanoantenna arrays is very challenging and new concepts will be necessary for its experimental realizations. Coherent nonlinear excitation and emission processes of nonlinear materials, which can be positioned at the feeding points of the individual antennas, could be one solution.

4.3.2 *Fabrication of nanoantenna array*

During my diploma thesis, I was able to obtain first results on the fabrication of the 3D geometry. In this thesis, I am able to achieve the necessary accuracy in the EBL layer-by-layer stacking procedure (see Section 3.2) and the new results are presented here. A SEM micrograph together with a schematic is shown in Figure 22. The inset in (a) depicts the geometry of the single Yagi-Uda antenna, consisting of a reflector, a feed and a director, as it has been designed in the previous section (resonant wavelength $\lambda = 1500$ nm). We choose the periodicity to be 450 nm in x-direction and 300 nm in y-direction, which is sub-wavelength, to avoid opening of the diffraction channels due to the periodic arrangement. The nominal lengths of the reflector, the feed and the director are 300 nm, 250 nm and 230 nm, respectively. The distance between the

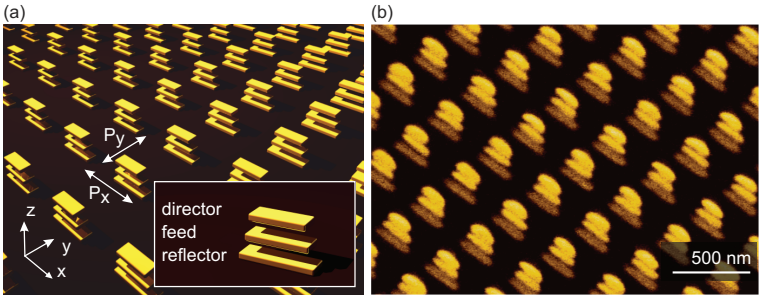

Figure 22: (a) Schematic of the 3D Yagi-Uda nanoantenna array. $P_x = 450$ nm and $P_y = 300$ nm are the periodicities in x- and y-direction, respectively. The inset is the single Yagi-Uda antenna consisting of a reflector (length 300 nm), a feed (length 250 nm) and a director (length 230 nm). The distance between the layers is 100 nm. (b) SEM micrograph of the fabricated structure. The antenna array is embedded in *PC403* and the footprint of the array is 90×90 μm^2. Adapted from [124].

layers is estimated to be 100 nm from the spin-coating parameters (see Section 3.2). The antenna array has a footprint of 90×90 μm^2 and, after fabrication of the third layer (director), we spin-coat another layer of *PC403* to embed the structure completely in a dielectric matrix.

4.3.3 *Receiving properties of the antenna array*

We have seen previously that aSNOM can be used to map the optical near-field distribution and also to demonstrate directional receiving by changing the direction of incident light on the antenna. The technique requires direct tip-sample interaction. Therefore, it cannot be used to investigate the receiving properties of our embedded antenna structure. In Chapter 5, we propose a novel technique, which is able to measure the near-field distribution of 3D buried antenna structures and is suitable for the IR and THz frequency region. Here, we use absorption as an indirect measurement of the current distribution inside the antenna structure.

The total loss of the antenna array P_{tot} can be expressed in terms of the currents in the individual elements as

$$P_{tot} = (P_{dir} + P_{feed} + P_{ref}) = mR(I_{dir}^2 + I_{feed}^2 + I_{ref}^2) \tag{54}$$

where m is the number of antennas in the array and I_{dir} (I_{feed}, I_{ref}) is the current inside the director (the feed, the reflector). R is the resistance of the nanorods and assumed to be equal for all elements as the lengths only differ by about 10% from each other. Equation 54 shows that the antenna array has higher absorption when the currents in reflector, feed and director are higher and not equally distributed over the elements.

We can characterize the receiving properties of the antenna array with conventional FTIR spectroscopy since the antenna axes are along the optical path in the spectrometer and the forward and the backward directions can be assessed by flipping the sample in the beam path. Figure 23 (a) shows the schematic with the definitions for the forward and the backward directions. Figure 23 (b) shows the numerical calculation

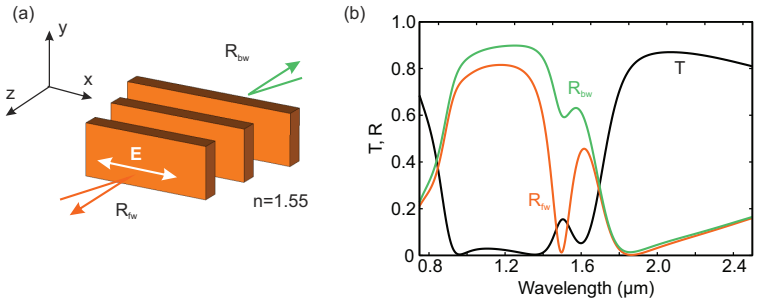

Figure 23: (a) Schematic showing that the forward notation is used for light impinging from the director side ($+z$) and the backward notation for light impinging from the reflector side ($-z$). The polarization is along the long-axis of the elements. (b) Numerically calculated transmittance and reflectance spectra for forward and backward incident light where the transmittance is equal but a distinct difference occurs at the resonance wavelength $\lambda = 1500$ nm in the reflectance spectra. Adapted from [124].

of the transmittance and the reflectance spectra for the two incident di-

rections when the polarization is along the long axis of the antenna elements, which has also been investigated in my diploma thesis. The transmittance is equal for incidence from both sides in contrast to a distinct difference in the reflectance, which occurs at the resonant wavelength $\lambda = 1500$ nm. Almost no light is reflected at this wavelength for light coming from the forward direction whereas only a small dip in the reflectance occurs for the backward incidence. This difference is attributed to the resonant behavior of the single Yagi-Uda nanoantenna, which has been designed to have maximum directivity in the forward direction at this wavelength.

We show the transmittance and reflectance spectra from the experiment in Figure 24 (a) and (b). In Figure 24 (a) the transmittance is equal

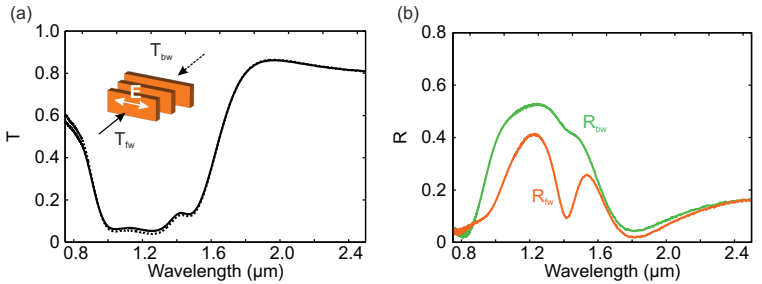

Figure 24: (a) The transmittance is equal for forward and backward incident light. (b) A difference at the resonant wavelength $\lambda = 1420$ nm occurs in the reflectance spectra for forward and backward incident light. Adapted from [124].

when we turn the sample around in the beam path changing the incident direction from forward to backward. It agrees very well with numerical simulations. We want to mention here that three resonances are observed in the transmittance, which are red- and blue-shifted compared to the plasmon resonance of the single elements. This is an indication of the near-field coupling between the layers due to hybridization [127]. What is also in good agreement with numerical simulations are the features in the reflectance spectra. A significant dip occurs at $\lambda = 1420$ nm

for the reflected light at the forward incidence compared to a very small modulation in the reflectance at the backward incidence at the same wavelength. The slight blue-shift of the feature compared to the numerical simulations is due to the fabrication tolerance of the plasmonic structures and the deviation in the spacer layer thickness.

We can now deduce the absorption A from the transmittance T and reflectance R, which becomes

$$A = 1 - T - R. \tag{55}$$

We plot the absorption spectra calculated from the numerical simulations in Figure 25 (a) and from experiment in Figure 25 (b). The ab-

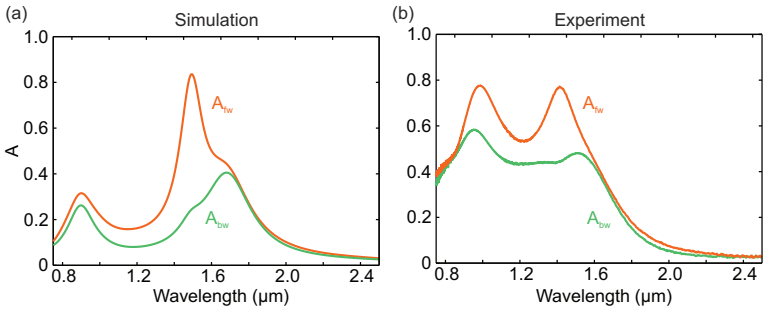

Figure 25: Absorption spectra deduced from simulations (a) and experiment (b) are plotted for the forward and the backward incidence. The largest difference in absorption between the forward and the backward incident light occurs at the resonance wavelength of about 1500 nm. Adapted from [124].

sorption is significantly higher around the resonant wavelength for the forward incident light compared to the backward incident light. At the resonant wavelength most of the power is dissipated in the gold structures for the forward incident light, which does not happen for the backward incident light. P_{tot} in Equation 54 reaches its maximum at the resonance wavelength for the forward incident light. We infer that the high absorption is due to an uneven distribution of the current among

the antenna elements upon illumination in the forward direction at the resonant wavelength.

In Section 4.2, we have shown that under excitation from the direction of the maximum directivity, most of the energy is exclusively confined to the feed element in a Yagi-Uda antenna (see Figure 19). In order to confirm that this is the case as well in the 3D Yagi-Uda nanoantenna array, we compare the simulated near-field distributions for the forward and the backward incident light in Figure 26. The structure is excited by

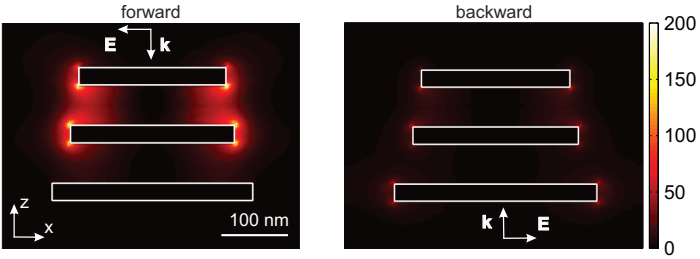

Figure 26: Near-field intensity distributions at the resonant wavelength, $\lambda = 1500$ nm, for plane wave illuminations from the forward direction (left) and the backward direction (right). Adapted from [124].

a plane wave at $\lambda = 1500$ nm. The strongest enhancement of the near-field intensity occurs at the feed element under the illumination from the forward direction. Another intensity enhancement is present at the tips of the director whereas the reflector remains completely dark. The near-field distribution is very different for the backward incident light where the near-field intensity is evenly distributed among all elements with an overall much weaker field enhancement compared to the case with the forward incident light. It proves that we have observed directional receiving in the direction of the substrate normal of our 3D optical Yagi-Uda nanoantenna array.

4.3.4 *Beamsteering with optical antenna array*

We have seen earlier that feeding each element in the Yagi-Uda nanoantenna array with the same phase leads to an enhanced directivity in the direction perpendicular to the plane of the array. In Section 2.3 we have introduced the concept of beamsteering, which is achieved by changing the phase between neighboring elements. In my diploma thesis, we applied this concept in the optical frequency regime by feeding each element in the 3D array with a different phase. Figure 27 (a) shows how it could be realized as a device. Each row of antennas along the

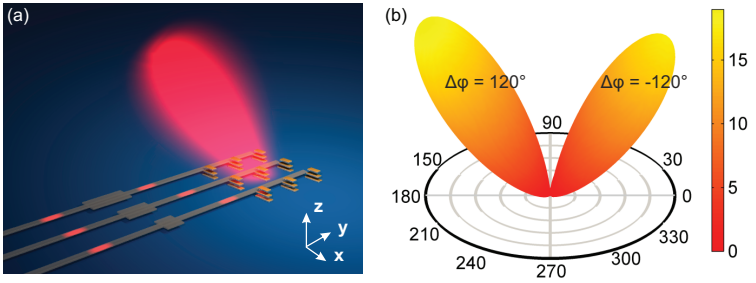

Figure 27: (a) A 3×3 Yagi-Uda nanoantenna array is fed with nanoscale waveguides. The feeding phase can be adjusted between adjacent nanoantennas so that beamsteering is achieved. (b) Simulated radiation pattern for the 3×3 array for a phase shift of $\Delta\varphi = +120°$ and $\Delta\varphi = -120°$ along the x-direction between neighboring antenna rows. Beamsteering from about $-30°$ to $+30°$ is realized. Different peak directivities are observed as the feeding point is at one end of the antennas. Adapted from [124].

x-direction is connected to a nanoscale waveguide, which is either a plasmonic waveguide or a high refractive index dielectric waveguide. The phase for each row can be adjusted by modulators so that in between each two neighboring rows there is a phase shift. By assigning a phase difference $\Delta\varphi = -120°$ to dipole emitters in adjacent rows and changing it to $\Delta\varphi = +120°$, we observe in simulation beamsteering over a range of

60°. Figure 27 (b) shows the two radiation patterns when $\Delta\varphi = -120°$ and $\Delta\varphi = +120°$, respectively.

4.4 CONCLUSION

We have shown in this chapter that directional receiving of radiation at the nanoscale is possible with optical Yagi-Uda nanoantennas. We have used aSNOM to analyze the modes of the receiving antenna and the coupling mechanism between the individual elements in a planar 2D Yagi-Uda antenna. This antenna geometry and its directivity can be easily tuned to different working wavelengths by just changing the length of the elements. The directivity of the 2D Yagi-Uda antenna is proved by measuring the near-field amplitude at the feed element under forward illumination and comparing it to the near-field amplitude under the backward illumination. The difference in the near-field distributions is due to the directional properties of the antenna. It is a very promising geometry for future applications, e.g., a nanoantenna link where the transmitted energy scales with the square of the directivity, which is studied in Chapter 6.

Furthermore, our measurement results demonstrate that the aSNOM technique is an appropriate tool to measure the directive properties of optical Yagi-Uda nanoantennas by assessing the near-field amplitude at the feeding point for different incident angles. Deep sub-wavelength resolution is achieved when mapping the amplitude and the phase. The results give insight into the working principle of the optical nanoantennas.

We have also realized 3D Yagi-Uda antennas with directive receiving properties from out of the substrate plane. It allows to fabricate 2D antenna arrays with the advantages of large enhancement of directivities and beamsteering. We have investigated the receiving properties of such Yagi-Uda nanoantenna arrays and have proved the field confinement at the feed element under forward illumination by using conventional FTIR measurement as well as numerical simulations.

5

SUB-WAVELENGTH LIGHT-MATTER INTERACTION IN THE INFRARED

5.1 INTRODUCTION

Optical spectroscopy in the IR region is a powerful analysis tool to detect and identify different kind of molecules. Molecules exhibit vibrational excitations at energies which are characteristic to the nature of the oscillation. Therefore the optical response is unique for each kind of molecule and its IR spectrum hence termed *molecular fingerprint*.

Nevertheless, huge quantities of molecules are needed for conventional spectroscopy techniques such as FTIR spectroscopy since the excitation of the vibrational resonances in the molecules is very inefficient. *Seeing* only a few molecules or even single molecules and identifying them via their molecular fingerprint plays a decisive role in health care, e.g. for early disease diagnostics or in industrial applications, e.g. in the detection of harmful substances or the detection of tiny concentrations of explosive gas mixtures.

This goal can be achieved by enhancing the optical cross section of molecular oscillations using surface-enhanced scattering techniques [128]. In surface-enhanced Raman scattering (SERS) the Raman signal is enhanced by several orders of magnitude, which was first observed by `Fleischmann et al.` on a roughened electrode surface [129]. Further experimental work on the origin of the enhancement was performed independently by `van Duyne` and `Creighton` [130, 131]. Over the years the sensitivity of the technique was improved so that the Raman signal of single molecules could be detected [80, 132]. Recently, sophisticated plasmonic nanoantennas were designed to serve as efficient SERS sensing platforms [64, 133] enabling a well-engineered optical response of the adsorbed molecules [134–137].

In surface-enhanced infrared absorption (SEIRA) the interaction of molecular vibrations with incident IR light is enhanced using nanostructured metallic substrates, which exhibit plasmonic resonances in the IR region. This effect was first observed by `Hartstein et al.` [138]. In the following years rough metallic films [139, 140], metallic nanoshells [141] or metallic nanoantennas [142–144] were used to increase light-matter interaction in the IR region via SEIRA.

In this chapter we will use SEIRA to detect very few quantities of molecules down to monolayers adsorbed on metallic nanoantennas as it is illustrated in Figure 28 (a). The nanoantennas, generating high near-field intensities shown in Figure 28 (b), are tuned in resonance or close to resonance with the vibrational oscillation. A typical infrared spectrum of vibrational bands is shown in Figure 28 (c). For this specific case the antenna in (b) is in resonance with the *Amide I* vibration of proteins and could be used to enhance the vibrational excitation in close by positioned proteins. Numerical calculations are used to design the antenna structures and also to predict the response of the coupled system, antenna plasmon and vibrational band. We will in detail elaborate on the mechanism of the light-matter interaction in this hybrid system introducing the concept of Fano-resonances [145]. The main part of this chapter will deal with a new method, which we develop to map plasmonic near-field intensities in the IR region based on SEIRA. For this we will use the quantitative response of the SEIRA signal, which depends on the local position of the molecules with respect to the nanoantennas. This is in particular important for the design of novel plasmonic structures and for the optimization of the coupling to molecular vibrations for detection and identification of trace substances. Moreover, our approach allows us to identify the physical mechanism which leads to the SEIRA signal. Our method is furthermore not restricted to planar surfaces but can measure the near-field intensity of 3D complex antenna structures. We will use a 3D plasmonic electromagnetically induced transparency (EIT) structure to demonstrate this. Our method is hence a complementary analysis tool to state-of-the art near-field mapping techniques.

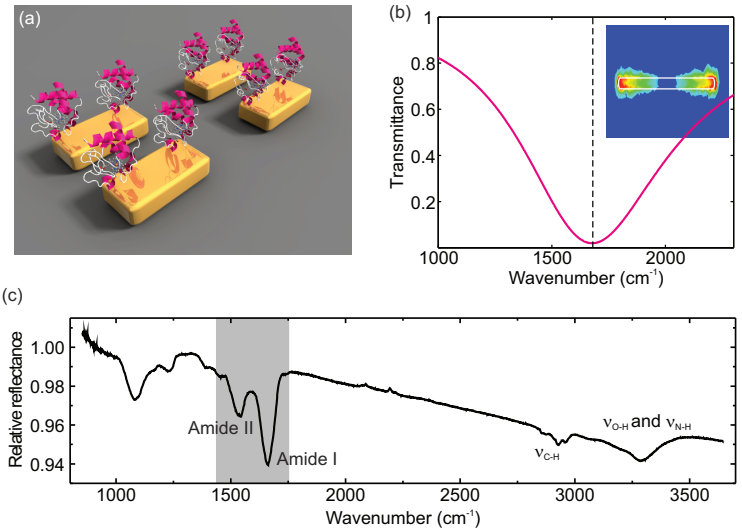

Figure 28: (a) Artistic impression of molecules adsorbed on the gold surface of plasmonic nanoantennas. (b) Numerically calculated far-field spectrum of an antenna array with a resonance frequency at the vibrational excitation of the *Amide I* band around 1640 cm^{-1} indicated by the black dashed line. The antenna length is 2650 nm. The inset shows the top-view of the near-field intensity at the resonance wavelength. (c) Typical infrared spectrum of a protein layer (*GIPC1*) on gold surface. The gray area indicates the region of the *Amide I* and *Amide II* vibrations. (Courtesy of Frank Neubrech).

5.2 THEORETICAL BACKGROUND

In this section the interaction of molecular vibrations with the light field will be shortly introduced. Furthermore an introduction to the concept of Fano-resonances is given, which describe the spectral response of EIT-like plasmonic structures and SEIRA. We finish this section with a short discussion about the signal origin in SEIRA experiments.

5.2.1 *Molecular fingerprints*

The number of degrees of vibrational motion of a molecule is $3N-6$ with N the number of atoms in the molecule and $N \geqslant 3$ [146]. These vibrational bands are associated with stretching, bending or rotational transitions where only stretching and bending vibrations can be observed in the condensed phase of molecules. They occur throughout the IR and THz region and can be probed with IR spectroscopy. Each observed band is characteristic for the vibration of a particular subgroup of atoms in a many atom molecule. IR spectroscopy is hence a powerful tool for structural analysis and identification of molecules [146].

The frequency $\Delta\nu$ of the vibrational band is given by the energy difference

$$\Delta E = h\nu_f - h\nu_i \tag{56}$$

of the transition from the initial state i to the final state f. Its intensity is determined by the perturbation of the molecule by the electromagnetic radiation. The perturbation is described in the quantum mechanical framework and in the dipole approximation by the operator $\hat{\mu} = q * \hat{\mathbf{r}}$, q being the effective charge and $\hat{\mathbf{r}}$ the effective displacement operator associated with the oscillation. The transition probability reads as [147]

$$P_{if} \propto |\langle \Psi_f | \hat{\mu} | \Psi_i \rangle|^2. \tag{57}$$

A vibrational transition is optically active and can be observed in the IR spectrum if the matrix element in Equation 57 is not vanishing and a change of the dipole moment is associated with the transition [146].

5.2.2 *Fano-resonances*

Fano-resonances are found in a multitude of physical phenomena [148]. Originally, Fano used his theoretical formula for explaining the lineshape of the spectrum of inelastically scattered electrons by helium [145]. Generally, Fano-resonances appear in physical systems where a spectrally

broad resonance and a spectrally narrow resonance are coupled. Interference of the different excitation pathways of the broad resonance leads to the typical lineshape, which furthermore depends on the energy overlap. It can be expressed as [148]

$$\sigma = \frac{(2(\omega - \omega_0)/\gamma + q)^2}{(2(\omega - \omega_0)/\gamma)^2 + 1}. \tag{58}$$

where σ is the cross section with resonance frequency ω_0 and spectral width γ. The Fano-parameter q determines the asymmetry of the Fano-resonance lineshape.

Recently, this intriguing phenomena was also observed in different arrangements of plasmonic and metamaterial structures [96, 149, 150], such as dimer structures [151–156], plasmonic oligomer structures [157–163], hybrid material structures [164], as well as discussed in theoretical investigations [165–169].

5.2.2.1 *EIT-like effects in plasmonics*

Fano's theory can describe the physical phenomena of EIT. EIT is a purely quantum mechanical effect in an atomic three-level systems [170] where destructive interference of two excitation pathways renders a dipole transition dark. The level scheme is drawn in Figure 29 (a). The transition $|0\rangle \rightarrow |1\rangle$ is dipole allowed and hence strongly radiation damped (large γ_1). The transition $|0\rangle \rightarrow |2\rangle$ is dipole forbidden and the decay rate γ_2 is therefore small. Another laser is used to couple $|1\rangle$ to $|2\rangle$, which means that $|1\rangle$ can be populated via two excitation pathways: directly via $|0\rangle \rightarrow |1\rangle$ and due to the coupling κ via $|0\rangle \rightarrow |1\rangle \rightarrow |2\rangle \rightarrow |1\rangle$. Destructive interference of the two pathways renders the transition $|0\rangle \rightarrow |1\rangle$ dark and leads to a narrow transparency peak in a broad absorption dip where the linewidths are determined by the decay rates γ_2 and γ_1, respectively. The detuning δ in energy determines the symmetry of the transmittance spectrum. A typical EIT spectrum is shown in Figure 29 (b) for the perfect symmetric case when $\delta = 0$.

Even though EIT describes a coupling phenomena of quantum mechanical discrete states, EIT-like effects can be observed in classical systems, such as coupled LC resonators [172, 173]. In plasmonics, the con-

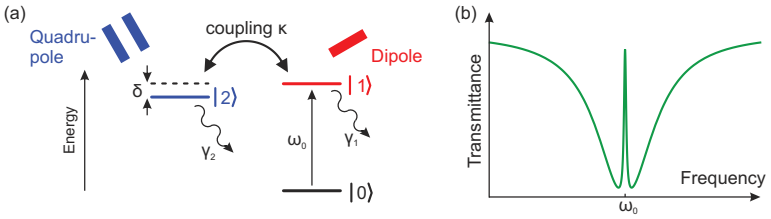

Figure 29: (a) Three level scheme of EIT. For switched on coupling κ the excited state $|1\rangle$ (bright state) is populated directly via the ground state $|0\rangle$ and simultaneously via the dark state $|2\rangle$ following $|0\rangle \rightarrow |1\rangle \rightarrow |2\rangle \rightarrow |1\rangle$. Interference leads to a transparency window. In a classical plasmonic EIT system the bright state can be a dipole (red) coupled to a quadrupole (dark state, blue). γ_1 and γ_2 are the decay rates of bright and dark transition with $\gamma_1 \gg \gamma_2$ and δ is the detuning. Adapted from [171]. (b) Typical EIT spectrum for $\delta = 0$ illustrating the EIT effect.

cept of the coupling scheme in Figure 29 still holds true when one replaces $|1\rangle$ with a metallic structure supporting a strong dipole moment (e.g. dipole antenna), which couples effectively to the radiation field. $|2\rangle$ is then a structure with weak dipole moment (e.g. quadrupole), being dark for the direct excitation via the radiation field. The coupling of bright and dark mode to each other in a plasmonic system is mediated via the near-field and renders the dipole mode dark at the transparency peak. The lineshape is narrow, which was recently harnessed in sensing applications where the steep slope of the spectrum increases the sensitivity on refractive index change of the environment [116, 174]. The high Q of the resonator can also be used to enhance the efficiency of nonlinear frequency conversion with plasmonic structures [170] and the strong dispersion renders these structures promising for slow light applications [175, 176] or reduction of losses [177].

The EIT effect depends crucially on the near-field coupling between dark and bright mode. This becomes an issue in fabrication for 2D structures where one needs to put them very close to each other on the order of several nm. This is hampered by the lateral size of the metallic nanostructures together with proximity effects in top-down EBL process

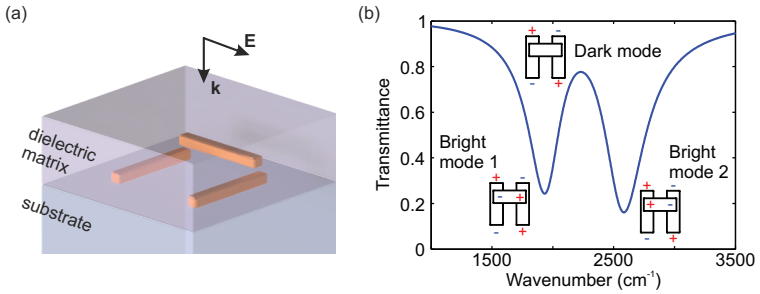

Figure 30: (a) Schematic of the 3D plasmonic analogue of EIT structure. Incident light is polarized along the long-axis of the bright dipole stacked on top of a dark quadrupole. Near-field coupling leads to mutual coupling between quadrupole and dipole. (b) Typical transmittance spectrum with respective charge distribution at the different modes: Low energy bright mode, dark mode, and high energy bright mode.

where small gaps are challenging to be realized. Stacking the structures on top of each other using a two-step EBL process proximity effects are avoided and the distance is tuned by the spacer layer (see Section 3.2). For example, `Liu et al.` fabricated a plasmonic dipole antenna on top of a plasmonic quadrupole [107]. A schematic of the structure is depicted in Figure 30 (a). The structure is embedded in a dielectric matrix and incident radiation is polarized along the long axis of the dipole. The dipolar charge distribution of the top wire leads to a quadrupole like charge distribution in the two wires below when the dipole is laterally displaced from the center position towards the tips of the quadrupole. As shown in the transmittance spectrum of Figure 30 (b) the near-field coupling results in two bright modes with excitation of charge oscillations in the dipole and the quadrupole, leading to Fano interference. It can also be understood in terms of mode coupling by looking at the charge distribution with the hybridization scheme for plasmonic structures [127, 178, 179]. For frequencies between the two modes the structure is transparent because the interference leads to canceling out of the charge distribution in the dipole at this spectral position.

Additionally, for larger distances between the two layers, retardation has to be taken into account. The coupling κ can now not only be switched on or off but the phase can be tuned by increasing the distance between the layers where near-field coupling is still maintained. For a properly tuned distance this can result in constructive interference of the two excitation pathways of $|1\rangle$, which was recently demonstrated in plasmonic nanostructures and termed plasmonic analogue of electromagnetically induced absorption (EIA) [109].

5.2.2.2 *Fano-lineshapes in antenna-enhanced vibrational spectroscopy*

Loosely speaking the plasmon mode in a metallic nanoparticle with large dipole moment can be considered as a classical continuum. Replacing the narrowband plasmonic resonator (quadrupole in the previous section) by quantum systems with discrete states such as quantum dots, atoms, or molecules, Fano interference occurs as well. This is particularly interesting since the coupling is mediated via the near-field and is observed via the lineshape in the far-field. We obtain therefore insight into light-matter coupling at the nanoscale by means of far-field spectroscopy. Furthermore these quantum transitions couple very weakly to the external light field and can be made visible via the coupling to plasmonic antennas. Such quantum systems with narrow lineshapes are for example vibrational transitions in molecules in the IR region. Recently, rigorous electromagnetic calculation and a quantum mechanical model were used to gain an understanding of the plasmon-molecule coupling at a quantum level [180] following the approach of Fano [145].

On the other hand a purely classical description using coupled harmonic oscillators can give an intuitive picture of the light-matter coupling as it has been outlined in [181]. In this picture, Lorentzian oscillators are coupled via a coupling rate to each other where only one oscillator experiences an external driving force. The absorption spectrum exhibits a Fano lineshape describing the experimental observations. The lineshape of the absorption spectrum in SEIRA experiments can therefore directly hint on the coupling mechanism of vibrational transitions to plasmonic modes. SEIRA experiments are furthermore intriguing be-

cause they make optically weak transitions of only a few molecules visible. Using plasmonic EIT structures for enhancing vibrational transitions adds another twist and could be beneficial for the signal enhancement due to higher near-field intensities at the high-Q dark modes of the plasmonic structure [149].

5.2.3 *Signal enhancement*

In SERS, the enhancement factor can be approximated to be proportional to the fourth power of the near-field intensity enhancement [182]

$$f_{SERS} \approx \left|\frac{E_{loc}(\omega_L)}{E_o}\right|^2 \left|\frac{E_{loc}(\omega_R)}{E_o}\right|^2 \approx \left|\frac{E_{loc}(\omega_L)}{E_o}\right|^4 \tag{59}$$

where E_{loc} is the local near-field amplitude at the laser frequency ω_L and the Raman frequency ω_R. E_o is the near-field amplitude without plasmonic scatterer and the second approximation is valid for a small Raman shift due to the vibrational excitation.

In SEIRA, the antenna is resonant in the infrared to the vibrational transition of the close-by molecules. The excitation rate depends on the local near-field intensity. It can be shown in *ab initio* calculations for typical antenna-molecule geometries that the reemission of light by the molecule is not prominent and the photon gets absorbed. A more handwaving argument for this can be made by considering the characteristic size a of a vibrational dipole transition. It is much smaller than the incident wavelength λ in the IR and a simple comparison of the classical scattering cross section $C_{sca} \propto a^6/\lambda^4$ and absorption cross section $C_{abs} \propto a^3/\lambda$ for small particles yields (see Equation 34):

$$\frac{C_{abs}}{C_{sca}} = \left(\frac{\lambda}{a}\right)^3 \quad \text{with} \quad \lambda \gg a \tag{60}$$

This suggests that in contrast to SERS experiments, absorption and not scattering is the dominant process in SEIRA. The channel scattering from the antenna to the molecule and back into the far-field via the antenna is a negligible process in SEIRA experiments [183] since the photon gets ab-

sorbed via the vibrational transition. As a consequence the SEIRA signal scales linearly with the local intensity:

$$f_{SEIRA} \propto \left| \frac{E_{loc}}{E_0} \right|^2 \tag{61}$$

This will be experimentally addressed in Section 5.4 where sub-wavelength volumes of molecules are positioned at different locations with respect to plasmonic antennas to probe their local near-field intensity enhancement.

5.3 DETECTING MOLECULAR MONOLAYERS WITH OPTICAL ANTENNAS

The extinction of light by molecules in a homogeneous sample with concentration C and thickness d is described by the *Lambert-Beer*-law [146]

$$-\ln \frac{I}{I_0} = \alpha C d. \tag{62}$$

It can be shown that the absorption coefficient α is proportional to the transition probability in Equation 57 [146], which is determined by the small dipole moment associated to the vibrational oscillation. For conventional IR spectroscopy long pathways d and high sample concentrations C are therefore needed to detect the vibrational transitions. Yet, for a large amount of applications in pharmaceutics or industry, it is essential to do spectroscopy on low concentrated samples down to single molecules. In this section we will show how to prepare monolayers of molecules on metallic surfaces and use plasmonic antenna structures with high local field intensities to make these single molecular layers detectable with antenna-enhanced spectroscopy.

5.3.1 *Formation of monolayers on metallic surfaces*

We use a self-assembled monolayer (SAM) to immobilize octadecanethiol (ODT)[1] molecules on a gold surface (see Figure 31). Gold is a very good

1 Sigma Aldrich, Germany

substrate for SAMs since its surface does not oxidize at ambient conditions and can be cleaned easily. With a thiol group $S-H$ at one end the ODT molecules bind to the gold surface and form a homogeneous monolayer where the orientation is well-defined due to van-der-Waals interaction between the adjacent alkyl chains [184].

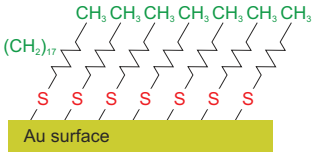

Figure 31: The ODT molecules bind covalently to the gold and form a homogeneous monolayer on the surface.

ODT molecules adsorb from solution onto the surface. It is important to keep the gold surface of the antennas clean after fabrication with EBL. The PMMA residuals from the EBL process are therefore removed with O_2 plasma etching. The sample is then immersed into a 0.1 mM solution of ODT in at least 98 % pure ethanol. The sample is removed from the solution after 30 hours and rinsed off with pure ethanol.

5.3.2 *SEIRA - Antenna-enhanced spectroscopy*

It was recently shown that the vibrational transitions of a SAM of ODT adsorbed on crystalline gold plasmonic antenna surfaces can be enhanced up to the order of 10^5 [142]. Also, vibrational bands in proteins, which are adsorbed on antenna structures, could be enhanced [26, 143, 149, 185, 186].

Here, we use EBL fabricated arrays of dipole antennas to observe vibrational transitions in a monolayer of ODT. Figure 32 (a) depicts the symmetric and asymmetric vibration of the $C-H_2$ bond in ODT. The length of the antennas were tuned so that the plasmon oscillation is in resonance with the vibrational bands. In this case the electric near-field intensity is enhanced by more than two orders of magnitude as it is

shown with numerical near-field calculations in Figure 32 (b). The polarization of incident light is along the long-axis of the antenna and the sideview shows that most of the near-field intensity is enhanced at the ends of the dipole antenna and confined to the surface. It is important that the distribution is not significantly altered by the presence of the substrate, which is in this case CaF_2.

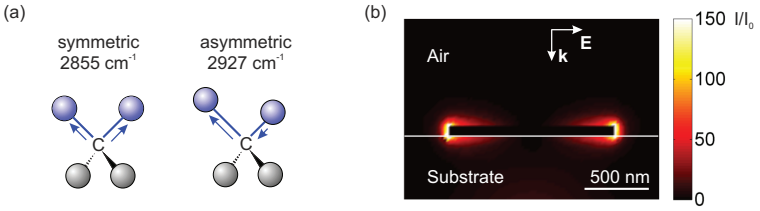

Figure 32: (a) ODT exhibits a symmetric and an asymmetric stretch vibration of $C-H_2$ at 2855 cm^{-1} and 2927 cm^{-1}, respectively. (b) Sideview of the numerically calculated electric near-field intensity enhancement I/I_0 of a plasmonic gold antenna on a CaF_2 substrate resonant at the stretch vibrations of ODT. I (I_0) is the near-field intensity with (without) antenna.

Figure 33 shows the measured transmittance spectra for five different antenna lengths with the polarization set along the long axis. The plasmon resonance is the broad peak shifting to lower energies with increasing antenna length. For all antenna lengths the plasmon resonances ω_{pl} are red-shifted compared to the vibrational bands ω_{vib} indicated by the black dashed lines. At the spectral position of the vibrational bands of ODT a dispersive feature is visible (zoom-in shown in the right panel) corresponding to the IR absorption of the monolayer. One can approximate a SEIRA enhancement factor due to the presence of the resonant antenna by taking as a reference the signal in infrared reflection absorption spectroscopy (IRRAS) measurement of ODT on a continuous gold film. Only the antenna ends where the near-field intensity is strongest are considered as interacting area. This means that the signal from about 150,000 molecules is considered ([142] and references therein). Figure 34 shows a comparison of the enhancement factor for single crystalline gold an-

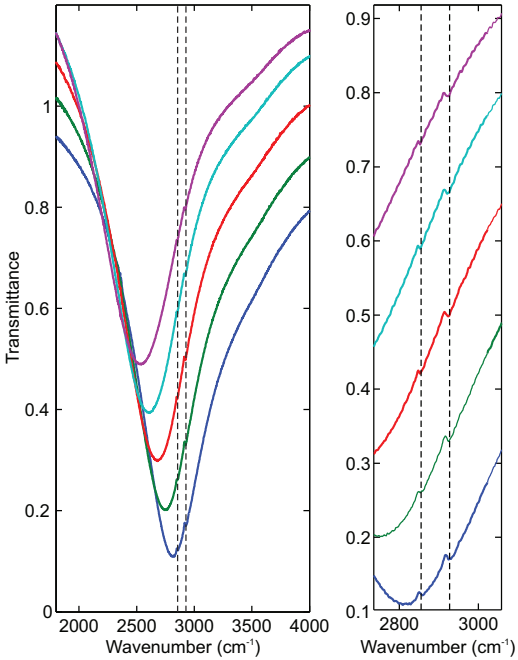

Figure 33: Transmittance spectra for different antenna lengths with a SAM of ODT on top of the gold antenna surface (left, spectra shifted for clarity by 0.1). The right panel shows a zoom-in of the transmittance spectra at the symmetric and asymmetric vibration of $C-H_2$. Black dashed lines indicate the vibrational bands. Spectra are shifted vertically for clarity.

tennas (data partially taken from [142]) to the enhancement factor for EBL fabricated antenna arrays as a function of the detuning of the plasmon resonance ω_{pl} with respect to the vibrational band ω_{vib}. Largest enhancement is achieved when the two resonances are spectrally overlapping where also the near-field intensity is largest. It is shown that the same order of magnitude enhancement is achieved with non-crystalline antenna structures in an array configuration. This suggests that the larger surface roughness of thermally evaporated gold does not have

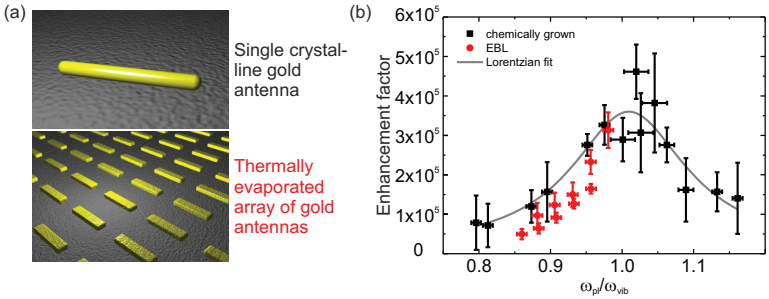

Figure 34: (a) Sketch of a single crystalline gold antenna (top) and an array of EBL fabricated gold antennas (bottom) on CaF_2 substrates used for enhancing the vibrational excitation. (b) Enhancement factor for the different antenna lengths as a function of the detuning ω_{pl}/ω_{vib}. Black squares are the estimated enhancement factors for the crystalline gold antennas (data taken partially from [142]) and the gray line is a Lorentzian fit. Red circles are the enhancement factors for the EBL fabricated arrays of gold antennas. (Courtesy of Frank Neubrech.)

major influences on the adsorption process of ODT molecules and the near-field enhancement associated with the plasmon resonance.

5.4 MAPPING PLASMONIC NEAR-FIELD INTENSITIES USING MOLECULAR NANOPROBES

In the previous section it was demonstrated that vibrational transitions in molecules adsorbed on a plasmonic antenna surface exhibit orders of magnitude enhancement due to very high near-field intensities associated with the plasmon resonance. The field distribution of these antennas suggest that the enhancement only stems from specific locations in the near-field of the antenna (see Figure 32 (b)). It is therefore of interest to assess these enhanced near-field intensities selectively. These will help to design novel plasmonic antenna structures resonant in the IR and optimized for coupling to vibrational transitions. Especially, 3D antenna structures exhibting EIT-like resonances are intriguing systems to enhance light-matter coupling in the IR as it has been outlined in Section 5.2.

So far, two-photon luminescence (TPL) microscopy was used to map plasmonic near-field intensities, which is limited by optical diffraction [40, 187]. Techniques with sub-wavelength resolution, such as electron energy loss spectroscopy (EELS) [65, 188], CL [163, 189], and photoemission electron microscopy (PEEM) [190, 191] require more complicated setups. They are nevertheless mostly restricted to the visible or near-IR region. High-resolution setups would be required to extend these techniques to the IR region. Also, accessing the hot-spots of 3D antenna structures which are buried in a dielectric matrix gets very difficult. Additionally, in the case of EELS, the samples need to be prepared on ultrathin membranes so that transmission electron microscopy (TEM) technology can work. Another technique is SNOM, which has been routinely used to map plasmonic near-fields in the visible as well as in the IR spectral region [49, 66, 72, 75, 123, 125, 183, 192–194].

However, mapping the electric near-fields of complex 3D embedded antenna structures [124, 195, 196] or plasmonic cavities [120, 197–199], remains very challenging for EELS, PEEM, and CL. For SNOM, mapping deeply below the surface is impossible because a direct tip-sample interaction is mandatory and the near-field intensity decays exponentially

with distance to the antenna surface. A further technique for plasmonic near-field mapping is local refractive index sensing, which was used to derive the local near-field intensity [200, 201]. Nevertheless, it is difficult to draw a quantitative conclusion from the spectral shift on the actual near-field intensity. In addition, photosensitive molecular probes around plasmonic structures were exposed via the plasmonic near-field intensity and subsequently imaged with SEM or AFM, which is an indirect measurement [202, 203].

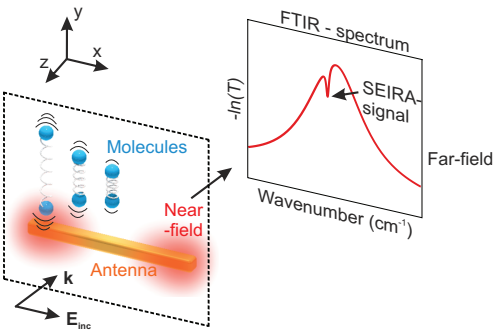

Figure 35: Molecules (blue) are positioned in the vicinity of plasmonic antennas (gold) at well-defined locations. IR radiation (x-polarized) is incident on the antennas along the $-z$-direction exciting the plasmon resonance. The molecular vibrational excitation depends on the spatial overlap of the molecules with the plasmonically enhanced near-field intensity. The spectrum is measured with conventional FTIR spectroscopy in the far-field. A narrow extinction feature, the SEIRA-signal, is observed on top of the broad extinction peak of the plasmon resonance.

In this section we present a new approach where a vibrational transition is used to directly map the near-field intensity of plasmonic nanostructures. A schematic of the measurement principle is shown in Figure 35. Molecular patches are positioned with an accuracy of 10 nm at different locations with respect to plasmonic antenna structures. The probe volume is deeply sub-wavelength, namely $1.4 \cdot 10^{-5}$ the volume of the free space wavelength cube. We measure the transmittance spec-

tra of the antennas in the far-field with conventional FTIR spectroscopy and extract the antenna-enhanced molecular vibrational strength as a function of the patch position. This is illustrated in Figure 36 where a typical extinction spectrum is shown. The broad peak is the plasmon resonance and the dispersive feature stems from the vibrational transition in the molecules, which is enhanced via the plasmonic near-field. A baseline correction where the spectrum is divided by the lineshape of the plasmon resonance gives a Fano-lineshape (see Section 5.2) [204]. This is the vibrational signal. The strength of this signal is defined in the right part of Figure 36. It is a quantitative measurement of the local near-field intensity since the vibrational strength scales directly with the overlap of the local molecular probe with the local plasmonic near-field intensity. This method works for plasmonic antenna structures resonant in the IR or THz spectral region. We show that molecular probes can be incorporated into complex 3D stacked plasmonic nanostructures, which allows to measure their near-field intensity. This is not possible with the aforementioned alternative methods and hence a stand-alone property of the technique.

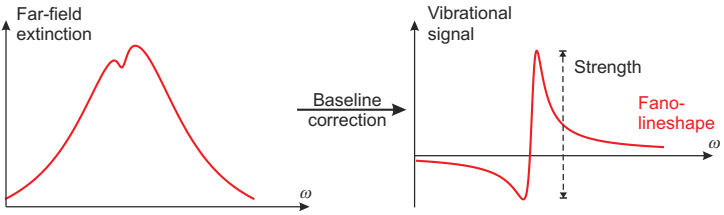

Figure 36: The far-field extinction spectrum (left) is baseline corrected around the vibrational resonance. The resulting spectrum (SEIRA signal, right) is a Fano-resonance due to coupling of the narrowband vibrational resonance to the broadband plasmon oscillation. The strength of the vibration is defined as the maximum minus the minimum of the SEIRA signal. Adapted from [78].

The presented results in this section are based on our publication of Ref. [205].

5.4.1 *HSQ - the molecular probe*

The probe molecules that we are using are patches of HSQ with a volume of $200 \times 200 \times 30$ nm^3. HSQ is a high-resolution negative resist where small volumes at well-defined position with our EBL stacking process can be fabricated (see Section 3.2).

On the other hand the patches are large enough that the optical properties of the material can be described with macroscopic material parameters. We follow here the derivation in [206].

The general wave equation in a conduction free medium is (see Equation 6)

$$\nabla \times (\nabla \times \mathbf{E}) + \frac{1}{c^2}\frac{\partial^2 \mathbf{E}}{\partial t^2} = -\mu_0 \frac{\partial^2 \mathbf{P}}{\partial t^2}. \tag{63}$$

The polarization $\mathbf{P}$ of the material induced by the propagating incident field vector $\mathbf{E}$ is described with a `Lorentz` model. It becomes for a harmonically time varying field with time dependence $e^{-i\omega t}$

$$\mathbf{P} = \frac{ne^2/m}{\omega_0^2 - \omega^2 - i\omega\gamma}\mathbf{E} = \epsilon_0 \chi_M(\omega)\mathbf{E} \tag{64}$$

with the resonance frequency ω_0, the damping γ, the density of electrons n, and the mass m and charge e of the electron. $\chi_M(\omega)$ is the frequency dependent susceptibility relating the polarization of the molecules to the incident electric field. Inserting Equation 64 in Equation 63 gives a differential equation for the electric field vector $\mathbf{E}$ where

$$\mathbf{E} = \mathbf{E}_0 e^{i(kz-\omega t)} \tag{65}$$

is a plane wave solution propagating along the z-direction provided that the wavevector k becomes

$$k^2 = \frac{\omega^2}{c^2}(1 + \chi_M(\omega)). \tag{66}$$

The wavevector is a complex number $k = \mathcal{K} + i\mathcal{A}$ and the solution of Equation 65 can hence be written as

$$\mathbf{E} = \mathbf{E}_0 e^{-\mathcal{A}z} e^{i(\mathcal{K}z-\omega t)}. \tag{67}$$

The extinction then becomes

$$-\ln\frac{I}{I_0} = -\ln\left|\frac{\mathbf{E}}{\mathbf{E}_0}\right|^2 = 2\mathcal{A}z, \tag{68}$$

which becomes the *Lambert-Beer* law describing the intensity decay in the medium (see Equation 62). In Section 5.2 we found that in a quantum mechanical picture the absorption coefficient is proportional to the transition probability (Equation 57) whereas here a classical expression for the attenuation coefficient $\mathcal{A}$ is found:

$$\begin{aligned} k = \mathcal{K} + i\mathcal{A} &= \frac{\omega}{c}\sqrt{1+\chi_M(\omega)} \approx \frac{\omega}{c}\left(1+\frac{1}{2}\chi_M(\omega)\right) \\ \mathcal{A} &= \frac{\omega}{2c}\,\mathfrak{Im}(\chi_M(\omega)) = \frac{\omega n e^2}{2cm\epsilon_0}\,\frac{\gamma\omega}{(\omega_0^2-\omega^2)^2+\gamma^2\omega^2}. \end{aligned} \tag{69}$$

$\chi_M(\omega)$ is the complex expression in Equation 64 and a Taylor-expansion was applied.

In Figure 37 the black curve is the extinction spectrum of a 30 nm thick HSQ film. Three absorption bands can be identified: two overlapping extinction peaks around 1100 cm^{-1} and one peak at 2252 cm^{-1}. To describe the spectrum we can sum up the different resonances and weigh them with an oscillator strength f_i, which gives the following expression for $\mathcal{A}$

$$\mathcal{A} = \frac{\omega n e^2}{2cm\epsilon_0}\sum_i \frac{f_i\gamma_i\omega}{(\omega_i^2-\omega^2)^2+\gamma_i^2\omega^2}. \tag{70}$$

Inserting this expression in Equation 68 gives us the fit-function to describe the experimental extinction spectrum. The fitting parameters are given in Table 1 where the vibrational bands are identified [207]. The different vibrational bands are shown with the red dashed lines in Figure 37 (a) and the total fit to the experimental extinction spectrum is shown in (b). It is important that the HSQ film is patterned with EBL before measurement since the $Si-H$ band at 2252 cm^{-1} is degrading with increasing electron dose in the exposure [207]. Therefore, in all our processing steps we were always using the same exposure conditions.

With the fitting parameters of the experimental extinction spectrum and

$$k = \frac{\omega}{c}n \quad \text{and} \quad \epsilon = n^2 \tag{71}$$

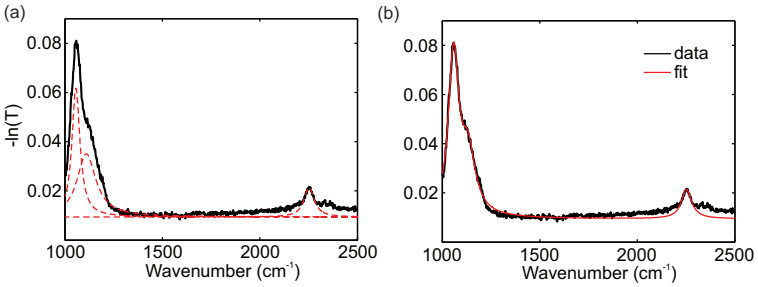

Figure 37: (a) Three Lorentz oscillators (red dashed curves) are fitted to the experimental extinction spectrum (black curve) of a 30 nm thick HSQ film. (b) Experimental extinction spectrum (black curve) and the complete fit (red curve) are shown.

we can now extract the complex dielectric function ϵ of HSQ and implement it as material parameters into our numerical simulation domain of CST. Real and imaginary part of ϵ are shown in Figure 38 (a). The numerical simulated extinction of a 30 nm thick HSQ film shows very good agreement with experiment [Figure 38 (b)].

5.4.2 *Sample design, fabrication and FTIR spectroscopy*

We use CST to design the antenna structures numerically. In our experiment we use gold nanostructures. The optical properties of gold in the IR can be well described with a Drude model, which we can implement into simulations. We use $\omega_{plasma} = 1.37 \times 10^{16}$ rad/s for the bulk plasma frequency and $\gamma = 1.4 \times 10^{14}$ rad/s, which accounts for the damping. As a substrate CaF_2 is suitable since it is transparent throughout the IR region from about 1100 to 10000 cm^{-1}. We set the refractive index to $n_{CaF_2} = 1.4$. For the optical properties of HSQ we use the dielectric function shown in Figure 38 (a), which we obtained from measurement. With this we are able to simulate the optical response of our plasmonic antennas coupled to the molecular HSQ probe. As it is seen in Figure 37, HSQ exhibits three vibrational bands in the given spectral region. Since

VIBRATIONAL BAND	RESONANCE FREQUENCY ω_0	DAMPING CONST. γ	OSCILL. STRENGTH F
$Si-H$ stretching	67.5 THz	1.99 THz	1.60×10^{13}
$Si-O-Si$ stretching	40.0 THz	2.49 THz	2.45×10^{13}
$Si-O_2$ vibrations	31.7 THz	1.99 THz	3.64×10^{13}

Table 1: Table of the HSQ parameters obtained from the fit shown in Figure 37 [207].

we want to extract a quantitative response of the antenna-enhanced vibrational excitation we focus here on the well-separated $Si-H$ band at 2252 cm^{-1}.

To fabricate the antenna samples we use standard EBL fabrication process as explained in Section 3.2. Typically, 100×100 μm^2 large antenna arrays are fabricated on a CaF_2 wafer. We evaporate 2 nm of chromium as an adhesion layer and 50 nm of gold, which gives the antenna height after lift-off. Together with this first antenna layer we additionally fabricate gold markers for later alignment of the coordinate system. Subsequently a 30 nm thick HSQ film is spin coated with spinning speed 6000 rpm for 60 seconds. For all samples we use the same exposure conditions for patterning the HSQ to make sure that the vibrational transitions are not altered from exposure to exposure. We use the gold markers to align the coordinate system to the first antenna layer. With this we achieve 10 nm accuracy in positioning $200 \times 200 \times 30$ nm^3 HSQ patches at different locations with respect to the plasmonic antennas. In order to enhance the vibrational band in HSQ with 3D antenna structures we use our stacking procedure explained in Section 3.2 with an additional EBL step in between for positioning HSQ patches. The spacer layer is *PC403*,

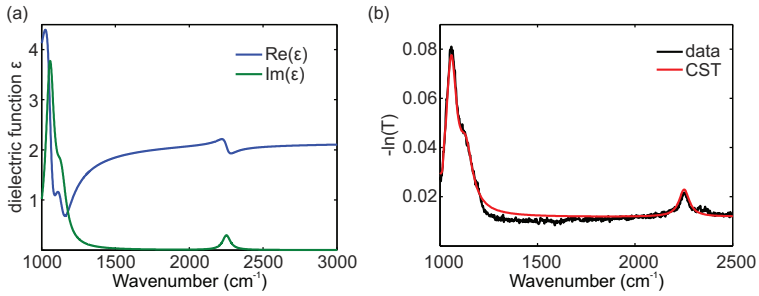

Figure 38: (a) The dielectric function ϵ of HSQ as a function of wavenumber is shown. It is extracted from the fit to the extinction spectrum shown in Figure 37. (b) The dielectric function is implemented as material properties into the numerical simulation domain of CST. The numerical simulation of a 30 nm thick HSQ film (red curve) agrees very well with the experimental extinction spectrum (black curve).

which works for our vibrational spectroscopy since no vibrational bands of *PC403* are overlapping with the vibrational band of HSQ at 2252 cm^{-1}.

We record transmittance spectra with our FTIR spectrometer. We measure 50 scans on sample and subsequently 50 scans next to the field as a background measurement. This yields one spectrum and we repeat the procedure 50 times and average the 50 spectra to reduce the influence of the vibrational bands of CO_2 and H_2O in the atmosphere.

5.4.3 *Quantitative near-field measurements*

In this part we discuss the use of HSQ patches as molecular nanoprobes of the plasmonic near-field intensity. We therefore position them at different locations with respect to different antenna structures and extract the vibrational strength as it is exemplary shown in Figure 39.

First, we investigate molecular patches at the end of plasmonic dipole antennas. As shown in the inset of Figure 28 (b) this is the location where the highest near-field intensity occurs. In Figure 40 (a) the SEM micrograph shows two exemplary antennas in an array with the mol-

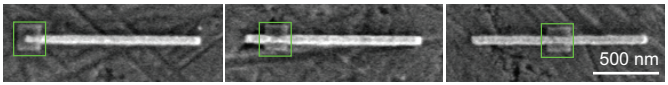

Figure 39: SEM micrographs of antennas with molecular patches (green) at different positions.

ecules in the patch at the left end. We use two incident polarizations, one along the long axis of the antenna (x-polarization) and one perpendicular to it (y-polarization). In the given frequency range around 2252 cm^{-1} x-polarized incident light excites the plasmon oscillation along the long axis of the antenna whereas y-polarization is off-resonant. This

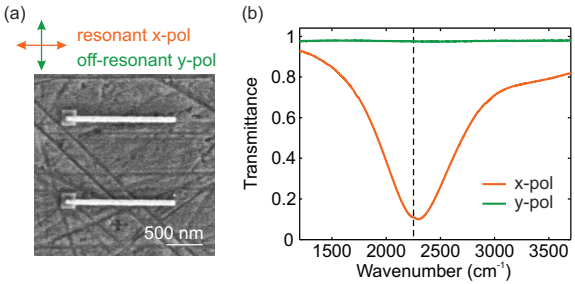

Figure 40: (a) SEM micrograph of two antennas in an antenna array is shown where the HSQ patch is positioned at the left end of each antenna. The volume of the patch is $200 \times 200 \times 30$ nm^3. The incident IR light is either polarized along the long axis of the antennas (resonant x-polarization) or along the short axis of the antennas (off-resonant y-polarization). (b) Transmittance spectra of the antenna array. The broad dip for resonant polarization (orange curve) is the plasmon resonance where a tiny feature is observed on top of it at 2252 cm^{-1} at the vibrational resonance (black dashed line). No resonance is observed for the off-resonant polarization (green curve). Adapted from [205].

is demonstrated in Figure 40 (b) where a broad dip in the experimental transmittance spectrum is observed for resonant polarization along the x-axis and the resonance being absent for the perpendicular polar-

ization. Furthermore the length of the antenna is designed to be resonant at 2252 cm^{-1}, which is marked with the black dashed line. A closer look at the plasmon dip of the transmittance reveals a dispersive feature exactly at the vibrational band. A zoom-in of this spectrum is shown in Figure 41 (a) together with the lineshape of the plasmon resonance (black curve). Now, the dispersive feature is clearly visible. We perform the baseline correction by dividing the transmittance spec-

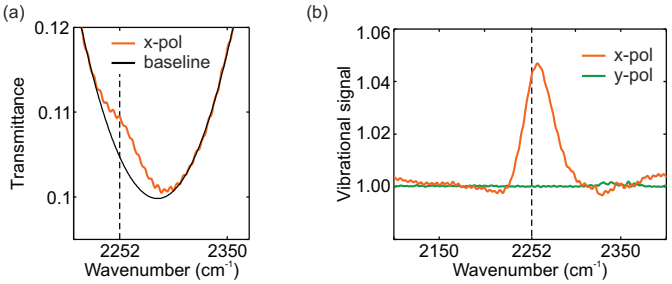

Figure 41: (a) A zoom-in of the transmittance spectrum for x-polarized incident light is shown (orange curve) together with the baseline (black curve). (b) Baseline correction of transmittance in Figure 40 gives the vibrational signal. A Fano-resonance is observed for x-polarized incident light (orange curve) and no feature is present for y-polarization (green curve). The black dashed lines in (a) and (b) indicate the vibrational resonance at 2252 cm^{-1}. Adapted from [205].

trum with the lineshape avoiding the vibrational band (orange curve and black curve, respectively) and plot the result in panel (b) of Figure 41 for both polarizations. For x-polarization a clear feature in the spectrum is observed, which we term vibrational signal. It is important that no signal is present for the other polarization where no plasmon oscillation is excited in the antennas. This means that an observed signal is originating solely from the enhanced near-field intensities associated with the plasmon resonance. The asymmetric lineshape of the vibrational signal can be explained with Fano interference (see Section 5.2). The spectrally broad plasmon resonance is coupled via the enhanced near-field inten-

sity to the spectrally narrow molecular vibration resulting in the Fano lineshape.

It is interesting to not only investigate the coupling of the molecular probe at the point of highest near-field intensity, but perform the nano-spectroscopy at different locations exhibiting different near-field intensities. Therefore, nine different patch positions are fabricated along the long-axis of the antenna, which is shown in the SEM micrographs in the right panel of Figure 42. The shift s is defined as the distance of the patch center to the left end of the antenna where negative values correspond to locations outside the antenna. In the left panel of

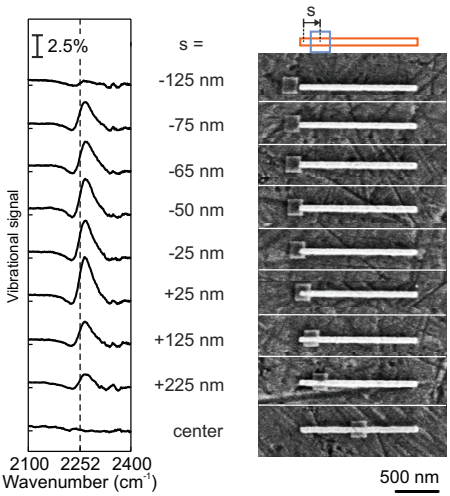

Figure 42: The measured vibrational signals for different patch position shifts s are shown. The spectra on the left are shifted for clarity and the vibrational resonance is indicated by the black dashed line. The SEM micrographs of the respective patch-antenna configuration are shown to the right. A patch shift s of only 10 nm in the near-field close to the antenna can be distinguished via the strength of the far-field vibrational signal. Adapted from [205].

Figure 42, the vibrational signals for the different patch locations are plotted and shifted vertically in accordance with the SEM micrographs.

Each vibrational signal exhibits a Fano resonance and its strength shows a strong dependence on the actual position of the patch. It is observed that the signal increases from $s = -125$ nm to the left end of the antenna ($s = +25$ nm) but then decreases again with shifting the patch further to the center of the antenna. Shifts of only 10 nm difference can be experimentally realized, which is demonstrated for the two patch positions $s = -75$ nm and $s = -65$ nm. Even though the difference is barley visible in the SEM images, a difference in the vibrational strength of the spectrum can be observed. This means that changes of the near-field intensity close to plasmonic antennas on a 10 nm scale lead to a difference in the light-matter coupling, which can be detected in the far-field.

The strength of the vibrational signal, as defined in the right panel of Figure 36, is used to measure the plasmonically enhanced near-field intensity of the dipole antennas. We extract the strength from each vibrational signal in Figure 42 and plot it as a function of the patch location in Figure 43 (a) (red circles). The error of the signal strength is smaller than the size of the red circles. We support the experimental data (red circles) with numerical simulations. Transmittance spectra for antennas in resonance with the vibrational transition and patches at 19 different positions along the x-axis are calculated. In the next step the vibrational strength is extracted from our simulations for each patch location. The data is normalized to the experiment (factor 0.85) and plotted as blue crosses together with the measured datapoints. Very good agreement is observed. A numerical simulation in Figure 43 (b) shows the typical enhanced near-field intensity distribution of the resonant dipole antenna.

From the considerations for conventional IR spectroscopy in Section 5.2 an intensity dependence of the vibrational signal is expected (see Equation 61). There, we have concluded from the small size of the vibrational dipole moment that absorption is dominating scattering. Here, we want to address this issue experimentally and answer the question: What is the influence of the antenna on the emission of the excited vibrational state? If the presence of the antenna provided enhanced scattering channels of the vibrational excitation similar to SERS an intensity squared dependence would be expected (see Equation 59). With our ex-

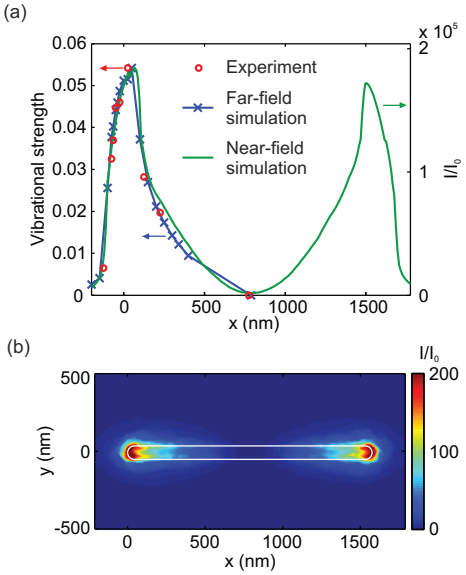

Figure 43: (a) The experimental vibrational strength (red circles) are extracted from the signals in Figure 42 and plotted for the different patch positions along the x-axis. The same is done in simulations for more patch positions along the x-axis (blue crosses). Very good agreement of the far-field data is obtained with numerical near-field simulations of the integrated electric-field intensity in the probe volume ($200 \times 200 \times 30$ nm^3) along the x-axis. (b) Numerically calculated near-field intensity 10 nm on top of the plasmonic antenna resonant at the vibrational band of HSQ (2252 cm^{-1}). Adapted from [205].

periment we measure the vibrational signal where its strength depends on the overlap of the molecular probe with the antenna generated near-field. We can now understand what near-field quantity exactly causes the enhancement if we compare numerical near-field simulations with the vibrational strength data. This is shown with the green curve in Figure 43, which is the ratio of the near-field intensity I along the x-axis of the resonant antenna and the near-field intensity I_0 with no antenna present. To be comparable to our experiment we integrate over the volume of the patch and shift this volume in 10 nm steps along the x-axis.

Very good agreement with the behavior of the vibrational strength is obtained, which proves that the vibrational enhancement scales with the near-field intensity as originally expected and not the near-field intensity squared. To support this fact we add in Figure 44 the near-field intensity squared (pink curve) illustrating the deviations from far-field experiment and far-field simulations. This means that efficient scatter-

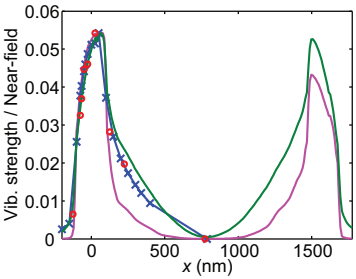

Figure 44: Very good agreement for the near-field intensity (green curve) with experiment and far-field simulation (red circles and blue curve) is obtained which is not observed for the intensity squared (pink curve). In fact, absorption is the dominating process over scattering contributing to the vibrational signal. The asymmetry between left and right edge of the antenna is due to numerical errors causing nonphysical high individual pixel values at the edge of the antenna.

ing channels are not provided due to the presence of the antenna, which would alter the intensity dependence of the vibrational strength. Small differences for patch positions $x > 0$ nm (inside the antenna) can be explained with modified probe volumes in the fabrication process when the patch is positioned on top of the antenna.

Chemical adsorption effects, such as the formation of metal-molecule complexes at the interface can be excluded, since most of the molecules in the patches are far away from the metal surface. For some patch positions the molecules are even not in contact with the metal. As discussed above, experimental and simulation results show excellent agreement where chemical adsorption effects are not taken into account in simula-

tion. Furthermore, chemical adsorption leads to a spectral shift of the vibrational band ω_{vib}, which we do not observe in our experiment.

From the experimental data we find that the vibrational strength is $8.4 \pm (0.9)$ higher at the end of the antenna compared to when the patch is located at $s = -125$ nm, which means that also the near-field intensity is that much higher. This method is able to accurately map plasmonic near-field intensities and allows to resolve differences on a 10 nm scale, which is only limited by the positioning accuracy of the EBL. Nevertheless, the near-field intensity is convoluted with the patch volume, which means that the lateral resolution is determined by the patch size. This can be improved by reducing that patch size but would lead to a worse signal to noise ratio, which is discussed later in this chapter.

The absolute enhancement factor of the signal strength is estimated to be 270. It is obtained by comparing the plasmonically enhanced vibrational signal when the patch is at the end of the antenna to the non antenna-enhanced vibrational signals of the HSQ film and taking into account the probe volume. Compared to the enhancement factors we observe in Section 5.3 and reported in other experiments [142, 208], the enhancement observed here is significantly smaller. The hotspots located at the antenna ends are not completely covered with HSQ, since the patch height is 30 nm compared to the 50 nm high gold antennas. Furthermore, the signal is integrated over the patch volume and vibrational transitions, which are further away from the antenna are excited less efficiently. Smaller patches at the hotspot of the antenna would lead to a larger enhancement.

5.4.4 *Spectroscopy at the nanoscale*

Light-matter coupling at the nanoscale is an intriguing topic of current research. Gaining a deeper understanding of how we can efficiently address light emission, absorption or scattering by nanosized objects could give answers to open questions in fundamental science and allows for a plethora of innovative technology in industrial applications. Radiation engineering in the visible and near-IR region was already demonstrated

in several experiments by coupling quantum emitters, such as quantum dots [85, 87, 209], nitrogen-vacancy centers in diamond [210–214] or fluorescent molecules [41, 83, 84, 215, 216] to plasmonic waveguides and plasmonic antennas. Our experiment, where we define molecular nanoprobes at different locations with respect to plasmonic antennas gives further insight into the coupling of molecular vibrations to the enhanced antenna near-field in the mid-IR and THz region. Nanospectroscopy in the IR and THz region with SNOM [183, 217–222] or tip-enhanced Raman spectroscopy (TERS) [223–225] already allow to enhance the transitions via the plasmonic oscillation in the tip from a sub-wavelength volume defined by the tip apex. Our method allows for the design of more complex plasmonic antennas to tailor the near-field intensity and enhance the vibrational excitations. From this perspective, our method gives besides quantitative information about the near-field intensity new possibilities in antenna-enhanced nanospectroscopy, which we will elaborate in the following.

5.4.4.1 *Dispersive probe*

The molecular patch has a strong dispersive response due to its narrow absorption bands [see Figure 38 (a)]. The measurement of the vibrational signal is therefore not only a probe for the near-field intensity as investigated before but also gives directly information on the plasmon-molecule coupling on the nanoscale. Usually, in SNOM experiments the tip has a rather flat spectral response and is a strong scatterer, which mediates the near-field intensity into the far-field. Therefore the detected signal would not represent directly the spectral response of the antenna-molecule coupled system but is altered by the necessary scattering channel provided by the tip. With our method we can directly measure the plasmon-molecule coupling with conventional FTIR spectroscopy, which we investigate here with plasmonic dipole antennas. We change the length of the dipole antennas, which shifts the plasmon resonance ω_{pl} with respect to the vibrational band ω_{vib}. The experimental vibrational signals are shown in the left column of Figure 45. The patch is here positioned at the left end of the antennas. One can observe that

the Fano-resonance changes its symmetry from asymmetric to symmetric when the antenna length is increased from the bottom to the top spectrum. The fit of the Fano-formula (see Equation 58) to the ex-

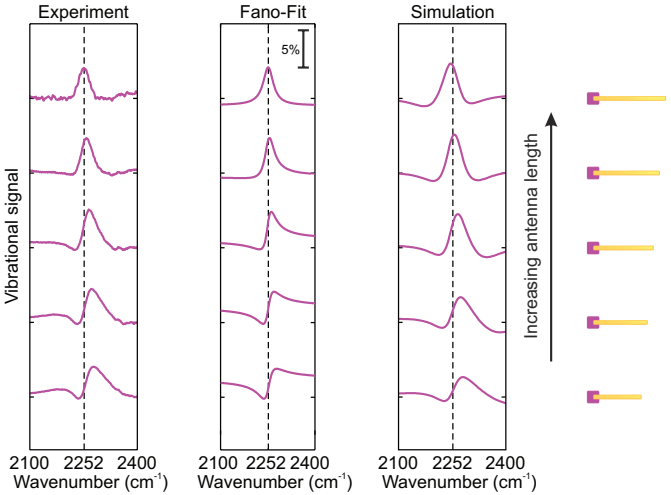

Figure 45: The patch is positioned at the left end of the antennas. The vibrational signal of experiment (left), fit of the Fano-resonance (center), and vibrational signal of numerical simulation (right) are shown for different antenna lengths. The antenna length increases from bottom spectrum to top spectrum, which tunes the plasmon resonance. A change of the strength and the lineshape of the vibrational signal is observed. The parameters are shown in Table 2.

perimental data is shown in the center column of Figure 45 where the Fano-parameter q is written in Table 2 together with the antenna length and the corresponding detuning ω_{pl}/ω_{vib}. The detuning shows that we investigate plasmon-molecule coupling from a blue detuned plasmon ($\omega_{pl}/\omega_{vib} > 1$) to a red detuned plasmon ($\omega_{pl}/\omega_{vib} < 1$). This results in the symmetry change, which is associated with the sign change of the Fano-parameter at perfect resonance overlap $\omega_{pl}/\omega_{vib} = 1$. The right column in Figure 45 shows the numerical calculations as a comparison

LENGTH (EXP.) AND ω_{pl}/ω_{vib}	FANO-PARAMETER	LENGTH (SIM.) AND ω_{pl}/ω_{vib}
1600 nm 0.99	+0.01	1625 nm 0.98
1550 nm 1.02	−0.21	1575 nm 1.01
1500 nm 1.04	−0.58	1525 nm 1.04
1450 nm 1.07	−1.05	1475 nm 1.07
1400 nm 1.10	−1.37	1425 nm 1.10

Table 2: The five different antenna lengths in experiment (left) and simulation (right) together with the detuning ω_{pl}/ω_{vib} are shown. The center column is the Fano-parameter extracted from the fit shown in Figure 45.

to experiment for antenna lengths written in Table 2. The lineshape and amplitude of the vibrational signal are in very good agreement.

We fabricate for each patch position five antenna lengths. In Figure 46 (a) we show four examples of positioned patches with respect to plasmonic dipole antennas. In the left panel of Figure 46 (b) the vibrational strengths are extracted from the five different antenna lengths for each patch position and plotted as a function of the detuning ω_{pl}/ω_{vib}. We compare it to numerical simulations where the result is shown in the right panel of Figure 46 (b). We simulate more antenna lengths than we realize in experiment. In the simulations we observe that the highest enhancement occurs for almost perfect overlap of the plasmon resonance frequency ω_{pl} with the vibrational resonance ω_{vib} whereas in experiment we observe a maximum for a slightly blue detuned plasmon. Furthermore the signal decreases with shifting the patch away from the left end, which is due to a decrease of the near-field intensity. For the patch at the center no signal is detected. In this representation it is clearly observed that a patch shift of only 10 nm has an influence on the vibrational signal strength and can be resolved experimentally (orange curve vs. blue curve).

Figure 47 (a) is the same representation as Figure 46 (b) for all patch positions in experiment and simulation. Since the strength is a direct measure for the near-field intensity, each data point represents the near-field intensity enhancement for a given detuning ω_{pl}/ω_{vib} at a certain location probed by the sub-wavelength volume of the patch. From Figure 47 (b), where the simulated data points are represented in a color-plot as a function of patch position x and detuning ω_{pl}/ω_{vib}, it becomes clear how the near-field intensity is enhanced at different locations and different frequencies.

5.4.4.2 *Probe volume*

In this section we investigate the influence of the probe volume on the vibrational signal and test the resolution limit of our current experimental configuration.

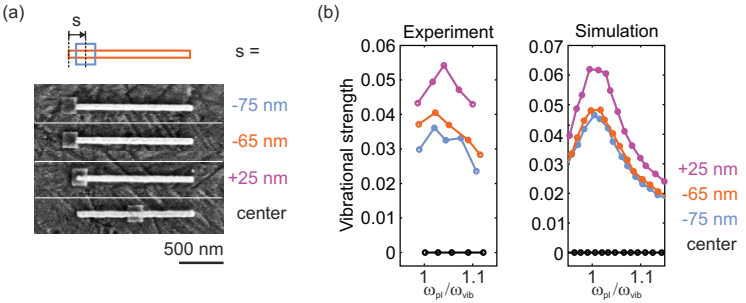

Figure 46: (a) SEM micrographs of four different patch locations along the x-axis of the dipole antenna. (b) Experimental vibrational strengths of five different antenna lengths as a function of detuning ω_{pl}/ω_{vib} (left) compared to 14 antenna lengths in simulation (right). The four different curves correspond to the different patch positions s as shown in (a) with respective color-coding. The highest vibrational strength is observed when the plasmon resonance is close to the vibrational transition (detuning ω_{pl}/ω_{vib} around 1) where the near-field intensity is highest. Adapted from [205].

At first, we fabricate two patches, which are symmetrically positioned with respect to the center of the antenna as shown in the SEM micrographs in Figure 48 (a). In the left panel we plot the respective vibrational signal for the resonant antenna length ($\omega_{pl}/\omega_{vib} \approx 1$). Considering the different scale compared to the one patch experiment in Figure 42 we observe double the signal. Also, in Figure 48 (b) where the spectral dependence of the signal strength is plotted we obtain similar behavior as in the one-patch experiment but double the strength. Here, the color-coding corresponds to the colors of shift s labeling the different patch positions. This is of course a well-expected result since the near-field intensity is symmetrically distributed with respect to the center of the antenna. Nevertheless, it proves that our method is giving accurate insight into the near-field distribution. Furthermore by increasing the probe volume we obtain a better signal-to-noise ratio at the disadvantage of lower resolution, which we will investigate in the following.

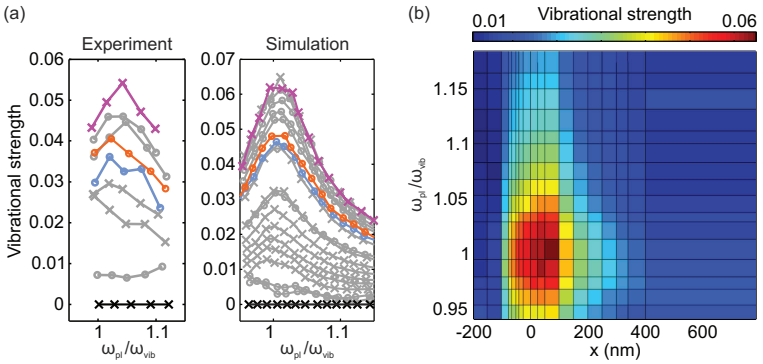

Figure 47: (a) All experimental (left) and simulated (right) vibrational strengths as a function of detuning ω_{pl}/ω_{vib} are plotted. The color coded spectra are the vibrational signals for the four patch positions shown in Figure 46 (a). The lines with circles correspond to negative patch shifts s, and the lines with crosses correspond to positive shifts s. (b) Different representation for the simulated vibrational strenghts in (a). The color encodes the strength as a function of the patch position (x-axis) and detuning ω_{pl}/ω_{vib} (y-axis). The maximum occurs for the left antenna end ($x = 0$ nm) and ω_{pl}/ω_{vib} around 1.

Figure 49 (a) shows SEM micrographs where we position HSQ patches at the left end of the dipole antennas and decrease the lateral size of the patches (200×200 nm^2, 100×200 nm^2, and 100×100 nm^2). Even for the smallest patch size we observe a signal, which is plotted in Figure 49 (b) (green curve) giving higher resolution when mapping the plasmonic near-field intensities. The drawback is that the signal-to-noise ratio is decreased and it would be more difficult to detect the enhancement when the patch is shifted away from the optimal position at the tip of the antenna. Yet, for all these experiments the band at 2252 cm^{-1} is used, which is a rather weak vibrational transition of HSQ compared to, e.g., the transitions around 1100 cm^{-1}. Choosing a strong vibrational absorption could improve the signal-to-noise ratio by orders of magnitude, which would allow for much smaller probe volumes. The limit is

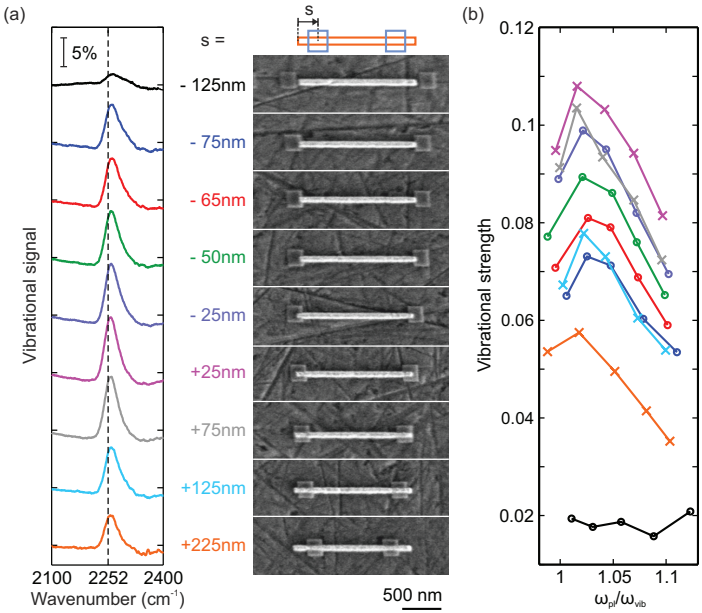

Figure 48: (a) The measured vibrational signals for different patch position shifts s are shown similar to Figure 42, but with two symmetrically positioned nanoprobes. The spectra on the left are shifted for clarity and the vibrational resonance is indicated by the black dashed line. The vibrational signal is two times larger than for one patch (compare Figure 42). The SEM micrographs of the respective patch-antenna configuration are shown to the right. (b) Vibrational strength measured for five antenna lengths for each patch position as a function of detuning ω_{pl}/ω_{vib}. Each colored curve corresponds to the respective patch position in (a).

the resolution of the EBL process to fabricate such small volumes on the order of only several nanometres [226–228].

5.4.5 *Plasmonic gap antennas enhancing vibrational transitions*

A promising geometry to further enhance near-field intensities are antennas with small gaps, so called dimer antennas. In Figure 50, SEM

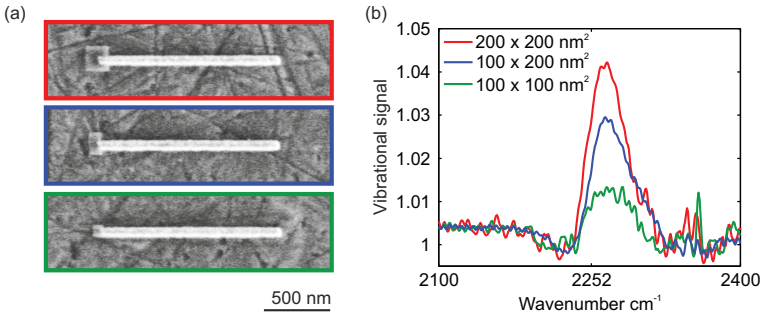

Figure 49: (a) SEM micrographs for three different molecular probe volumes positioned at the left end of the antennas: $200 \times 200 \times 30$ nm^3 (red), $100 \times 200 \times 30$ nm^3 (blue), $100 \times 100 \times 30$ nm^3 (green). (b) Vibrational signals for the different sized molecular probes in (a).

micrographs of dimer antennas with a 55 nm gap are shown. For such small gaps, much smaller than the incident wavelength, the hybridization scheme suggests that two new modes are formed, where one exhibits a dipole moment, which can therefore be excited with incident plane waves. This mode is lowered in energy due to the attractive interaction of the induced current oscillations in the two arms. Large near-field intensities in the gap are expected, which increase with decreasing gap size. In order to measure these effects we position the molecular patches

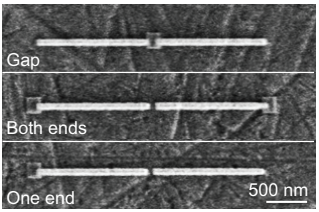

Figure 50: Three different patch positions with respect to plasmonic gap antennas are fabricated: one patch at the gap (top SEM micrograph), two patches at both ends (middle SEM micrograph), and one patch at the left end of the antenna (bottom SEM micrograph). Adapted from [205].

in the gap of such antennas. Furthermore, we realize configurations with patches at the ends of the antenna as a reference (see Figure 50).

As for the dipole antennas we measure transmittance spectra and extract the vibrational signals and strengths. The vibrational signals for the three different patch configurations are plotted in Figure 51 (a). We observe an 5.9($\pm$0.2)-fold enhancement of the vibrational strength with the patch at the gap compared to the patch at the left end of the antenna. This translates in an equally enhanced near-field intensity in the gap. The gap size of 55 nm is still rather large and the enhancement would increase strongly when the gap is further reduced. When comparing the one patch at the left end to the two patches at both ends a factor of 2 is observed between the respective signal strengths. This is well expected, since the probe volume is simply doubled for the two patches and the near-field intensity is symmetric along the long axis of the antenna having the same distribution at both ends.

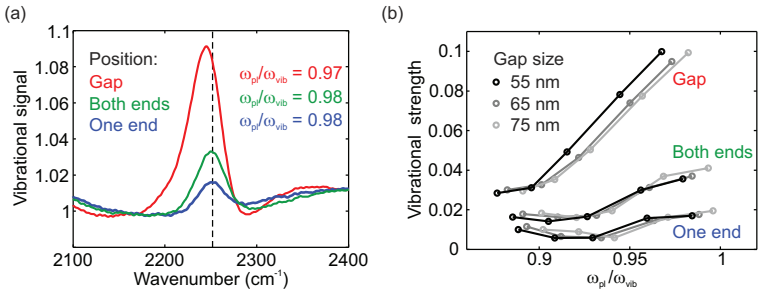

Figure 51: (a) Vibrational signals for the three different patch positions shown in Figure 50 and a gap size of 55 nm. The strongest signal is observed for the patch at the gap (red curve). Two patches at both ends (green curve) show double the signal strength compared to one patch (blue curve). (b) The vibrational strength for three gap sizes, five antenna lengths, and three patch positions as a function of the detuning ω_{pl}/ω_{vib} are plotted. Each set of curves corresponds to a patch position labeled accordingly in the plot. The gray-scale color-coding indicates the gap size as labeled in the plot. Adapted from [205].

In Figure 51 (a) the detuning values ω_{pl}/ω_{vib} are given. They indicate the spectral shift of the plasmon resonance ω_{pl} with respect to the vibrational band ω_{vib} and can be modified by changing the length of the antenna arms. For the shown vibrational signals in Figure 51 the detuning is smaller than 1, which means that the antennas are slightly red detuned to ω_{vib}. For each of the three different patch positions we fabricate five antenna lengths, varying the detuning. The vibrational strength as a function of ω_{pl}/ω_{vib} is plotted in Figure 51 (b). Additionally, three different gap sizes for each patch position and each antenna length are realized where the vibrational strengths are also shown in Figure 51 (b). First, it becomes clear that the near-field intensity is highest at the gap. Second, tuning the antenna lengths more in resonance with the vibrational band leads to an increased strength and hence higher near-field intensity. Third, decreasing the gap size leads to a higher strength hence higher near-field intensity. It is important to note here that the gap size shows no influence on the strength when the patches are located at the ends of the antenna, which demonstrates furthermore the accuracy of the method. Also, only the 55 nm gap has an influence on the signal strength whereas it is equal for 65 nm and 75 nm. It seems, that in this configuration the near-field intensity only starts to increase for gap sizes equal and smaller than 55 nm. Further experiments with additional gap sizes should be performed to draw more quantitative conclusions.

5.4.6 *Assessing near-field intensities of 3D plasmonic antenna structures*

Adding another dimension to planar structures leads to improved functionalities, such as chirality [229–238], more efficient near-field coupling with the possibility to induce retardation [109, 120], or novel concepts, like out-of-plane beamsteering [124]. Especially for sensing applications and Raman or IR spectroscopy, a 3D arrangement interacts naturally with incident light in common experimental setups where the light propagation direction is usually perpendicular to the substrate normal as we have seen in Section 4.3 for 3D Yagi-Uda nanoantennas. Hence, sensing platforms with 3D plasmonic structures as building blocks have a great

potential. So far, it was not possible to measure the near-field intensity of complex 3D plasmonic antennas. This is possible with our method, where the positioning of the molecular probe is the same process like the layer-by-layer fabrication of 3D plasmonic antennas and hence easy to incorporate. In addition, by coupling molecular transitions to these complex antenna structures, we are making use of their advanced properties, like higher near-field intensities or narrow linewidths, which is beneficial for the detection of vibrational transitions.

It was demonstrated that near-fields of shallow buried plasmonic scatterers can in principal be measured with SNOM [239]. Nevertheless, SNOM relies on the overlap of the near-field intensity with the tip, which cannot penetrate into the substrate or the dielectric matrix where the plasmonic antenna is embedded in. It is therefore restricted to structures, which are close to the surface. Resolution and depth contrast decrease rapidly with increasing distance of the tip to the structure. In our approach, the vibrational signal depends only on the overlap of the molecular probe with the plasmonic near-field intensity. The probe patches can be directly incorporated during fabrication of 3D antenna structures next to the different layers. There is no limitation for the thickness of the dielectric matrix, in which the antenna is embedded, as long as it is transparent for IR light. Our method is therefore perfectly suited to measure the near-field intensity of 3D plasmonic structures, which is demonstrated in this section.

We are investigating the coupling of a plasmonic Fano-resonance to the narrow transition of molecular vibrations. We choose a 3D plasmonic EIT structure as it has been suggested by `Liu et al.` (see Section 5.2). We position molecules at the edge of the bright (dipole) and the dark resonator (quadrupole). Figure 52 (a) and (b) depict the schematic and the experimental realization of the two configurations. In (a) the molecular patches are at the edge of the quadrupole and the dipole antenna is stacked as a second layer, whereas the geometry is reversed in (b) where the patches are positioned at the edge of the dipole. In the SEM micrographs (bottom) the molecular patches are not visible anymore after coating the first layer with the dielectric spacer (*PC403*) due to the weak

contrast of electron scattering between *PC403* and HSQ. For both configurations the patches are buried in a 160 nm thick spacer layer. The dipole

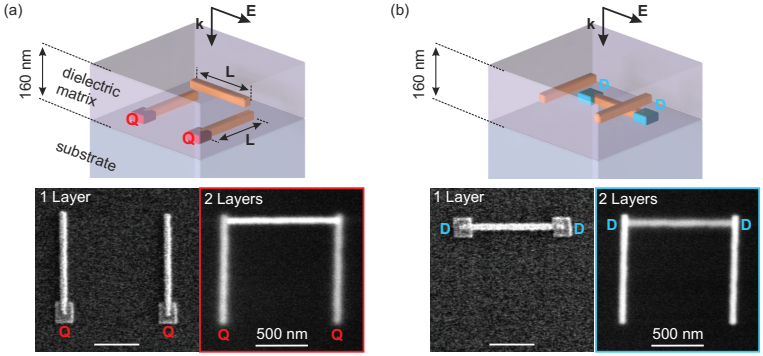

Figure 52: Schematics and SEM micrographs of molecular nanoprobes coupled to a 3D plasmonic EIT structure. The structure is embedded in a 160 nm thick dielectric matrix. (a) After the first layer, molecular patches are positioned at the end of the quadrupole (bottom left SEM micrograph). The dipole antenna is fabricated in a second EBL step on top (bottom right SEM micrograph). The patches are not visible in the dielectric matrix. (b) The first layer is the dipole with the patches at the end and a second layer of quadrupole is fabricated on top. Adapted from [205].

is shifted away from the center position of the quadrupole and its dipolar mode can therefore induce a quadrupole-like charge distribution in the two wires of the quadrupole via near-field coupling. As explained in Section 5.2 this leads to a cancellation of the charge distribution in the dipole at certain energies rendering it dark. This is observed in the transmittance spectra of Figure 53 (a) where for the vertically shifted spectra the length L of the respective wires are increased from bottom to top spectrum. As expected, two bright modes are observed with a transparency window in between, originating from the coupling to the dark quadrupole mode. By changing the length, it is possible to tune the different modes in resonance with the vibrational transition at 2252 cm^{-1}, which is indicated by the black dashed line. The blue (red) spectra correspond to the configruation when the patches are positioned at the dipole

(quadrupole). The narrowband absorption features around 1740 cm^{-1} and 2900 cm^{-1} stem from vibrational excitations in the dielectric matrix and are not of importance here. To observe the enhancement of the HSQ

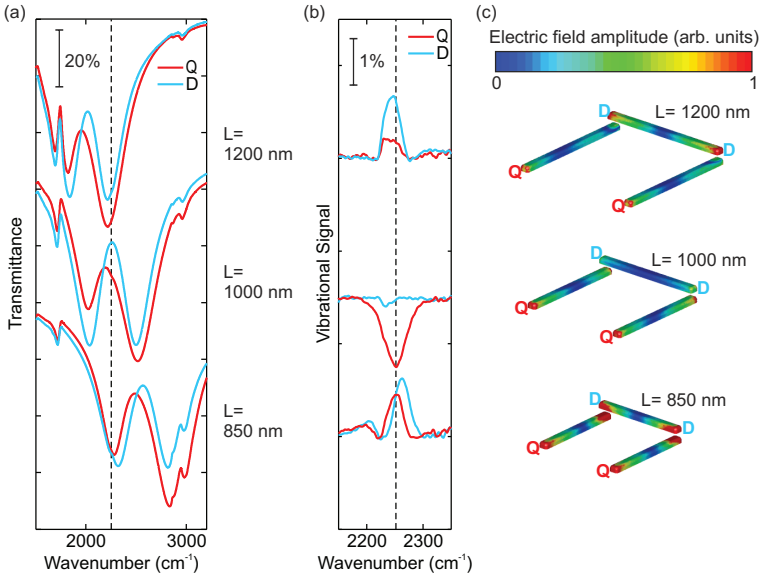

Figure 53: (a) Transmittance spectra for increasing structure size (spectra shifted vertically) with the lower energy bright mode, the dark mode, and the higher energy bright mode tuned to the HSQ vibration, respectively. The spectral position of the HSQ vibration is indicated by the black dashed line. The red (blue) curve is the transmittance spectrum when the patches are positioned at the quadrupole (dipole) (see Figure 52). (b) Vibrational signals for the three different modes with patches at the quadrupole (red curves) and the dipole (blue curves), which is supported by the simulated electric field amplitude on the structure surface in (c). Adapted from [205].

band, the baseline corrected vibrational signal is plotted in Figure 53 (b). Very different features are observed for the different lengths and the different patch positions. For the two bright modes (bottom and top spectra) both patch positions render a signal where the signal from the dipole is higher than from the quadrupole. The signals have a Fano line-

shape with enhanced transmission around the HSQ transition. When the dark mode of the EIT structure is tuned in resonance to the vibrational band, no signal is observed for the dipole (blue curve in the center spectrum). A clear signal is observed when the patches are positioned at the quadrupole. Strikingly, a *reduced* transmission (dip) is observed around the HSQ transition, which stems from the interference of the mutual coupling of vibrational transition to the plasmonic Fano resonance. With the near-field simulations in Figure 53 (c) we can understand the signal strengths of the measured vibrational signals. Indeed, at the dark mode, the electric field amplitude at the dipole is very low compared to at the quadrupole. For the two bright modes the simulation shows that the electric field amplitude is enhanced at the dipole and at the quadrupole, which is consistent with our experimental observations.

5.4.7 *SEIRA with single antennas*

All the results in the previous sections are measured on arrays of plasmonic antennas. Although EBL is a fabrication process with high reproducibility small differences between the individual antennas can occur. An ensemble measurement rules out these individual particularities and deletes them from the near-field picture that we get. It might be therefore interesting to apply the method to single structures. Also, for detecting vibrational transitions in single molecules or measuring its modification when a single molecule undergoes a conformation change, it is necessary to go to single antennas. In Figure 54 (a) the transmittance spectrum of a single antenna is shown with the patch positioned at the point of highest near-field intensity, at one end of the antenna. The spectrum was taken with a conventional FTIR spectrometer and a globar light source. It becomes clear that the noise is too large to make conclusive observations on the enhancement of the vibrational transition. Still a tiny distortion to the transmission can be seen at the HSQ band (black dashed line). In Figure 54 (b) a synchrotron was used as a light source delivering high intensities. In this case, the vibrational excitation can be observed more clearly due to a better signal-to-noise ratio but at the

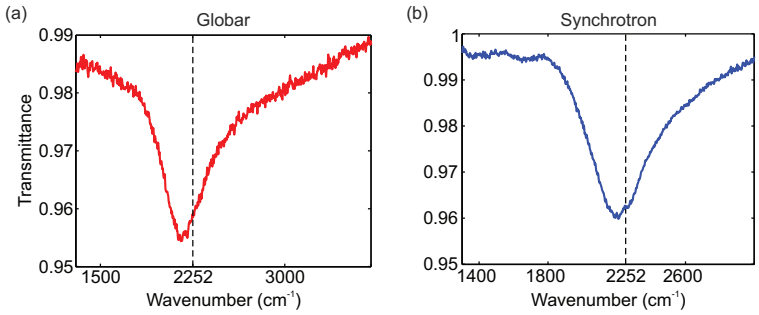

Figure 54: (a) Transmittance spectrum measured with a globar of a single dipole antenna where a HSQ patch is positioned at one end of the wire. (b) Transmittance spectrum measured with a synchrotron as a light source. The black dashed lines indicate the vibrational transition in HSQ at 2252 cm^{-1}.

disadvantage of tremendously increased complexity of a synchrotron source. Combining the FTIR with high-power white-light laser sources in the infrared will yield a table-top setup with good signal-to-noise ratio. Antenna-enhanced spectroscopy of nanoscale molecular volumes or even of single molecules in the lab could be realized.

5.5 SUMMARY

We have seen that IR spectroscopy in combination with the high near-field intensities generated by plasmonic antennas is a powerful technique. It can play a big role in pharmaceutical, industrial applications or in life sciences, where optical spectroscopy of a few or single molecules is required.

It has been shown that by employing SEIRA with well-defined antenna structures, we gain insight into the coupling of antenna-enhanced near-field intensities to molecular transitions. Especially, the quantitative character of the coupling has been investigated and a new method has been demonstrated for mapping plasmonic near-field intensities in the IR region. It is not restricted to a very narrow spectral window but can

be applied throughout the IR and THz region by exploiting the whole *fingerprint* region, which offers a huge variety of resonance frequencies, spectral linewidths and vibrational strengths.

The presented near-field mapping technique could be extended in the future for measuring the optical density of states of plasmonic antennas [83, 163, 240] or high-Q cavities [241] in the IR region via the absorption transition of molecular vibrations. This could lead to new concepts of radiation engineering in the IR and THz region at the nanoscale.

6

WIRELESS OPTICAL SIGNAL TRANSFER AT THE NANOSCALE

6.1 INTRODUCTION

Integrated electronics is approaching the limit in further miniaturization and therefore at consequence novel ideas are needed to avoid saturation of information processing. In this realm, a single molecule optical transistor was demonstrated [242] and fast optical switching capabilities of a single nitrogen-vacancy center in nanodiamond were recently published [243]. Besides this, it is a major task to develop new concepts enabling efficient on-chip and also chip-to-chip data transfer between nanoscale devices. Current photonic components already allow orders of magnitude better performance regarding bandwidth and speed of signal transmission than state-of-the-art electronic wire connections with at the same time low power consumption [90]. Concepts in silicon photonics based on dielectrics are close to on-chip implementation. Yet, the minimum size of such components is at about half the wavelength due to the diffraction limit. It is therefore of great interest to achieve efficient signal transmission on the nanoscale at optical frequencies. An ideal optical data link should fulfill the following requirements:

1. Efficient signal transfer to and from nanoscale devices.
2. Low-loss signal transfer, also across large distances for chip-to-chip communication.
3. Controllable distribution of the signal to different receiving points.
4. Nanoscopic footprint of the device enabling high integration density.
5. Large bandwidth for multiplexing data streams.

Plasmonics brings optics to the nanoscale [2, 5]. Current research demonstrating optical signal transfer at the nanoscale has been carried out on plasmonic wires [54, 58, 103, 211, 244–247] or a chain of plasmonic nanoparticles [248–250]. They allow a lateral confinement of the propagating plasmon mode to the sub-wavelength scale which makes efficient signal transfer from and to nanscopic devices possible. Nevertheless, these wire connections exhibit huge losses, they have a fixed layout, and realizing crossing data links requires a complicated 3D layer arrangement.

A novel concept in optical communication is wireless signal transfer at optical frequencies with optical nanoantennas. The link consists of a transmitting and a receiving nanoantenna and the signal is transmitted in free space. Nanoscale mode confinement at the two points is achieved due to the resonant plasmonic properties of the nanoantennas. The receiving pattern [123, 124] and the transmission pattern [34, 85, 87, 251–253] of the optical antennas can be engineered to achieve high directivities as we have seen in Chapter 4.

Figure 55 depicts the concept of wireless signal transfer with plasmonic antennas in comparison to the concept of plasmonic wire connections. In both cases nanoscale confinement is achieved at the point of interests with the main differences that for the plasmonic waveguide the mode is guided on the metal surface throughout the transmission line until it reaches the receiving point. This has a large impact on the amount of transferred power as illustrated in Figure 56. In the waveguide case the power transfer follows an exponential decay with increasing distance:

$$\left(\frac{P_R}{P_o}\right)_{Wg} = e^{-\alpha d}, \tag{72}$$

where P_R is the remaining power after propagation of the input signal P_o across a distance d. In contrast, wireless power transfer exhibits power law decay due to free-space propagation of radiation. It is described with the *Friis equation* [118]

$$\left(\frac{P_R}{P_o}\right)_{Ant} = e_T e_R (1-\Gamma_T^2)(1-\Gamma_R^2) D_T D_R (\hat{\mathbf{p}}_T \cdot \hat{\mathbf{p}}_R)^2 \left(\frac{\lambda}{4\pi d}\right)^2. \tag{73}$$

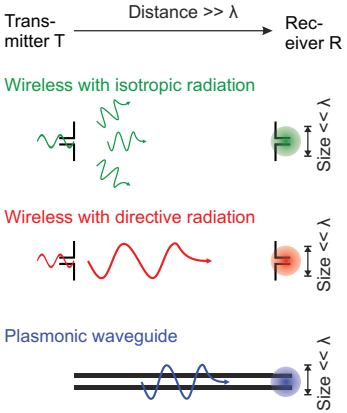

Figure 55: The challenge is to transport optical signals from and to nanoobjects which are much smaller than the wavelength λ across distances which are much larger than λ. State of the art plasmonic waveguide connections (lower panel) are very lossy compared to free space signal transfer with optical nanoantennas (two upper panels). Directive radiation by using sophisticated antenna geometries is even more beneficial (see Figure 56).

where the efficiencies $e_{T,R}$, impedance matching properties $(1-\Gamma_{T,R}^2)$, directivities $D_{T,R}$ and respective orientations $\hat{\mathbf{p}}_{T,R}$ of transmitting and receiving antenna are taken into account. For perfect impedance and polarization matching and alignment of the two antennas in the direction of maximum radiation it reduces to

$$\left(\frac{P_R}{P_o}\right)_{Ant} = G_{oT} G_{oR} \left(\frac{\lambda}{4\pi d}\right)^2, \tag{74}$$

which is expressed in terms of the gains $G_{oT,oR} = e_{T,R} D_{oT,oR}$ of the antenna pair. Thus, power transfer is increased for enhanced directivities, which is demonstrated in Figure 56 by comparing the red ($D_o = 6$) and green curve ($D_o = 1$). Overall, the $1/d^2$ decay outperforms the exponential decay of waveguides by orders of magnitude for large distances. We assume for the waveguide an absorption constant $\alpha = (2\mu m)^{-1}$ at $\lambda = 785$, which was experimentally demonstrated for a lithographically fabricated 100 nm wide nanowire [103]. In this case a distance increase

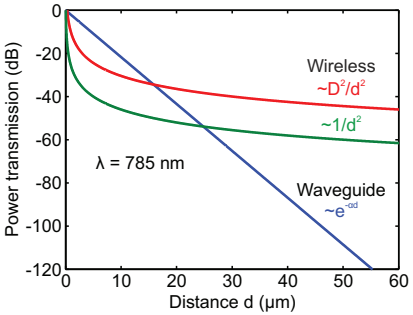

Figure 56: The blue curve is the power transmission for a plasmonic waveguide following an exponential decay (see Equation 72). The wireless point-to-point connection realized with optical nanoantennas transfers signal via free space with a power law signal decay (see Equation 74). Compared to the waveguide this is orders of magnitude more efficient for large distances d.

from 20 μm to 200 μm leads to a signal drop by more than 40 orders of magnitude, which is not competitive with the 1% of power arriving at the receiving antenna in the wireless link. Besides this, it has been demonstrated for cylindrical plasmonic wires where the propagation constant can be calculated analytically that a decrease of the width and therefore smaller mode volume leads to a strong increase of the absorption [254]. The antenna link does not suffer from this trade-off between propagation length and mode confinement. Furthermore, plasmonic waveguide links require a much larger footprint scaling with the transmission distance whereas the footprint of the wireless link remains nanoscale no matter what the distance between transmitter and receiver is. This also means that multiple crossing links can be realized without the need for complicated and bulky multilayer arrangements.

In Section 2.3 the concept of antenna arrays in the RF domain was introduced. In Chapter 4 we have shown that the advantages of increased directivity and beam steering compared to single antennas apply also in the optical regime. We have seen above that increased directivity leads to increased power transfer in an antenna link and the possibility

of beamsteering would allow for redistribution of the signal to different receiving points in a controllable way. This is depicted in Figure 57 where a phased optical antenna array distributes the signal to different receiving antennas depending on the feeding phase.

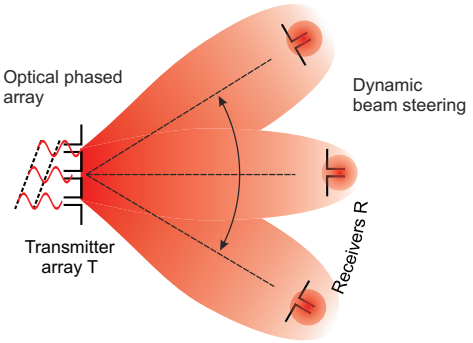

Figure 57: Phasing an optical nanoantenna array leads to redirection of the transmitted radiation. Different receivers can be adressed dynamically in a reconfigurable nanoantenna link via beamsteering.

In this chapter we experimentally demonstrate an optical nanoantenna link. The transmitter is driven by a focused laser beam at $\lambda = 785$ nm. We use fluorescent light of dye molecules to image the resonantly scattered intensity. Similar techniques were employed to image propagating surface plasmons [255–258]. The antennas are embedded in a homogeneous environment so that the radiation pattern is not deflected. We observe a gradual directivity increase of the radiation by adding antenna elements to an antenna array. Using patterned fluorescent nanoscopic receivers we are able to directly record the intensity transfer, which follows the predicted power law decay. Additionally, we investigate the influence of a receiving plasmonic antenna by sub-wavelength confinement of the incident radiation. Due to the steep focusing of our incident wave we can adjust the gradient of the wavefronts across the transmitter array to control the emission direction. We achieve a beam steering

range of 29° and use different plasmonic antenna receivers to pick up the signal at different points.

6.2 EXPERIMENTAL CONSIDERATIONS

We give in this section a short description of the experimental setup and give details on the sample fabrication allowing us to position fluorescent receivers with nanometer precision. The larger part is devoted to the theoretical description of the electric field in a high-NA objective. This will be important to understand the influence of the incident beam on the imaged fluorescence and allows to describe the phasing of the antenna array causing the beamsteering.

6.2.1 *Experimental setup*

The experiments are performed with a home-built fluorescence microscope (schematic shown in Figure 58). As excitation source we use 785 nm laser diodes[1]. The tilt of the incident beam is adjusted with a mirror mounted on a galvanometer. A lens system projects the tilt of the mirror to the backfocal plane of the objective leading to scanning of the incident beam in the image plane. We use an oil immersion objective (NA = 1.4)[2] to focus the incident beam. We collect the fluorescent light with the same objective and filter it from the excitation light with a dichroic beam-splitter[3] and a long-pass filter[4]. Wide-field images of the sample are taken with a nitrogen cooled CCD camera[5] and confocal scans can be performed by recording the intensity through a pinhole with a single photon counting module based on an APD[6].

1 Spindler and Hoyer, Germany; Roithner Lasertechnik, Austria
2 Nikon CFI Plan Apo VC 100, Japan
3 Semrock, USA
4 Chroma, USA
5 Princeton Instruments, USA
6 Perkin Elmer, Canada

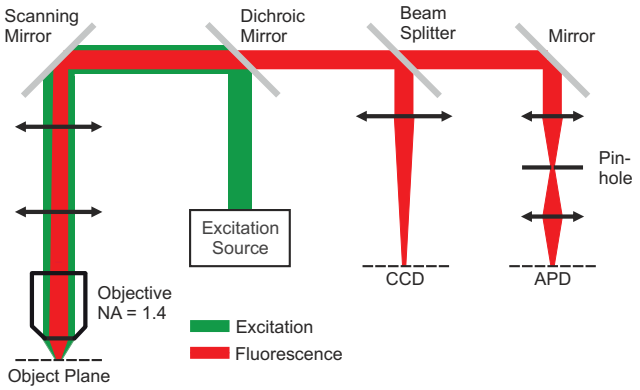

Figure 58: Experimental setup to perform confocal scans and to record wide-field images of a fluorescent sample. The setup is equpipped with a high-NA objective ($NA = 1.4$). A scanning mirror adjusts the incident laser beam with respect to the sample and a dichroic mirror separates excitation from fluorescence light. The object plane can be imaged on a CCD camera or the fluorescent light is detected through a pinhole with an APD while scanning the incident laser beam.

6.2.2 *Sample fabrication*

We use standard EBL as outlined in Section 3.2 to fabricate single antennas and antenna arrays on microscope cover glasses. For the measurement of the radiation pattern we cover the sample with a layer of fluorescent molecules (*IR140*)[7]. This is done by mixing them with a concentration of 2 mg/ml into PMMA (950k chain length) and spin coating the polymer with the standard parameters (see Section 3.2). The layer thickness is 60 nm and a final bake at 160° for 5 minutes hardens the layer. This is important to stabilize the layer since it is covered with immersion oil.

For the antenna link we fabricate in addition to the antenna transmitter receiving plasmonic antennas. For a second EBL step we blend

7 Sigma-Aldrich, Germany

IR140 dye molecules in negative resist (ARN 7520)[8] at a concentration of 2 mg/ml. The prepared resist is spin coated for 30 s with 6000 rpm and subsequently baked for 60 s at 90°. The thickness of the layer is 60 nm. We use the alignment procedure described in the stacking approach of Section 3.2 and pattern 250 nm diameter disks out of the fluorescent resist at defined positions.

6.2.3 *High-NA microscopy*

In this section we will show how to calculate the electric field in the focus of a high-NA objective. The objective is assumed to fulfill the *sine-condition* where the imaging optics in the objective can be replaced with one refracting reference sphere. This is equivalent to assume that the image quality by the objective is not reduced by spherical aberrations. The refracted field at the reference sphere is then propagated to the focal point with the *angular spectrum representation* introduced in Section 2.1 giving the full vectorial field around the focal plane. The same approach is used to calculate the PSF and the resolution limit of our imaging system by calculating the image of a point dipole in the focal plane of our objective. The theoretical treatment of the focal fields follows the textbook by `Novotny and Hecht` [53].

6.2.3.1 *Paraxial approximation of a propagating Gaussian beam*

The cross section in a plane $z = 0$ of a linearly polarized propagating laser beam can be approximated with a Gaussian field distribution

$$\mathbf{E}(x, y, 0) = \mathbf{E}_0 e^{-\frac{x^2+y^2}{w_0^2}}, \tag{75}$$

with w_0 being the beam waist at $z = 0$. It generally propagates along z with spreading out slowly in the transverse direction. In this case the wavevector k_z in Equation 9 can be approximated with the expansion

$$k_z = k\sqrt{1 - (k_x^2 + k_y^2)/k^2} \approx k - \frac{k_x^2 + k_y^2}{2k}, \tag{76}$$

8 Allresist, Germany

which is the *paraxial approximation*. The full field propagating along the z-direction can be now calculated by evaluating the spatial Fourier spectrum $\hat{\mathbf{E}}(k_x, k_y, 0)$ and inserting it into the angular spectrum representation (Equation 10) with the paraxial approximation for k_z. The calculation can be followed in [53] and only the result for $\mathbf{E}(\rho, z)$ with $\rho^2 = x^2 + y^2$ is given here

$$\mathbf{E}(\rho, z) = \mathbf{E}_0 \frac{w_0}{w(z)} e^{-\frac{\rho^2}{w^2(z)}} e^{i[kz - \eta(z) + k\rho^2/2R(z)]}, \tag{77}$$

where the following abbreviations have been used

$$\begin{aligned} w(z) &= w_0\sqrt{1 + z^2/z_0^2}, && \text{beam radius, with} \quad z_0 = \frac{kw_0^2}{2}, \\ R(z) &= z(1 + z_0^2/z^2), && \text{wavefront radius,} \\ \eta(z) &= \arctan(z/z_0), && \text{phase correction.} \end{aligned} \tag{78}$$

The phase correction $\eta(z)$ expresses a gradual phase shift of π when the beam propagates through $z = 0$ where w_0 is the beam waist. This phase change is called *Gouy phase shift*. Another important parameter is z_0, which is the *Rayleigh range*. It indicates the distance in positive and negative z-direction where the beam stays roughly collimated, namely where the radius $w(z)$ has increased to $\sqrt{2}w_0$. In Figure 59 the main

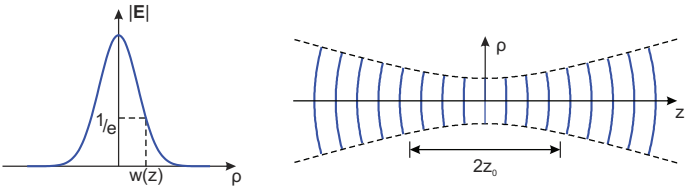

Figure 59: The amplitude of the electric field in a plane $z = \text{const.}$ is shown (left) and the wavefronts propagating along the z-direction are illustrated (right). Adapted from [53].

characteristics with the definitions of $w(z)$ and z_0 of the propagating Gaussian beam are shown.

The description in Equation 77, found in the paraxial approximation, is not a solution to Maxwell's equations and it breaks down for describ-

ing fields where the transverse wavenumbers (k_x,k_y) become comparable to k. This is the case for electric and magnetic fields upon focusing with a high-NA objective where maximal angles of around $\theta_{max} = 70°$ between propagating rays and optical axis are possible. A rigorous description is then required to calculate the electric and magnetic fields, which is treated in the following.

6.2.3.2 *Electromagnetic field in the focus of a high-NA objective*

The *angular spectrum representation* is applied to calculate the fields in the focus of a high-NA objective. The procedure is outlined here and the main results are presented. The detailed approach can be looked up in [53] and in the references given there.

Replacing the rather complicated lens system in an objective with just one spherical surface is a valid simplification of the problem when the *sine condition* is fulfilled by the objective. It states that each converging ray to the focus intersects the incident ray on the sphere at the distance ρ to the optical axis (see Figure 60). The image generated by objectives with a complicated combination of aspherical lenses can therefore be calculated using the approach here. For any converging ray to the focus

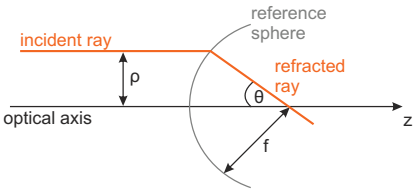

Figure 60: Any incident ray propagating parallel to the optical axis at a distance ρ converges to the focus after being refracted at the reference sphere. Adapted from [53].

the distance ρ of an incident ray to the optical axis becomes then

$$\rho = f \sin(\theta), \tag{79}$$

with f being the focal length and θ the angle between optical axis and refracted beam propagating to the focal point. The reference sphere transforms the cylindrical coordinate system (ρ, ϕ, z) of the incident ray to a spherical coordinate system (r, ϕ, θ) after refraction, where $r = f$ when the point is on the surface of the lens. We limit our calculation to the case where plane waves are incident on the objective. This is a valid assumption since in our experiment the incident laser beam completely fills the aperture of our objective. Furthermore, we assume that the incident field is polarized along the x-axis so that the amplitude of the incident field is

$$\mathbf{E}_{\text{inc}} = E_{\text{inc}} \mathbf{e}_x, \tag{80}$$

and that no light is reflected from the surface of the lens. The refracted field on the surface of the reference sphere can then be expressed in spherical coordinates as

$$\mathbf{E}_\infty(\theta, \phi) = E_{\text{inc}} [\cos\phi \mathbf{e}_\theta - \sin\phi \mathbf{e}_\phi] \sqrt{n_1/n_2} \sqrt{\cos\theta}. \tag{81}$$

$\mathbf{E}_\infty$ denotes the vectorial field at the surface of the reference sphere, which converges to the focus. The ∞ index indicates that we are only considering propagating wave components filtering out evanescent waves which do not contribute to the fields in the focus. Together with this, we require in the expression for the angular spectrum representation of Equation 10 that $kr \to \infty$. After some intermediate steps, which are outlined in Ref. [53] the field in the focal point becomes

$$\begin{aligned}\mathbf{E}(\rho, \varphi, z) = \frac{ikfe^{-ikf}}{2\pi} \int_0^{\theta_{\max}} \int_0^{2\pi} \mathbf{E}_\infty(\theta, \phi) e^{ikz\cos\theta} \\ e^{ik\rho\sin\theta\cos(\phi-\varphi)} \sin\theta \, d\phi \, d\theta.\end{aligned} \tag{82}$$

The integration over θ is limited to $\theta_{\max}$, which is given by the NA of the objective

$$NA = n \sin\theta_{\max}. \tag{83}$$

Equation 81 can now be inserted into Equation 82 and the integration over ϕ can be carried out analytically so that the final expression for the focal field in cartesian coordinates becomes

$$\mathbf{E}(\rho, \varphi, z) = \frac{ikf}{2}\sqrt{\frac{n_1}{n_2}}E_0 e^{-ikf}\begin{pmatrix} I_{00} + I_{02}\cos 2\varphi \\ I_{02}\sin 2\varphi \\ -2iI_{01}\cos\varphi \end{pmatrix}, \tag{84}$$

where the following abbreviations for the integrations over θ have been used:

$$\begin{aligned} I_{00} &= \int_0^{\theta_{max}} \sqrt{\cos\theta}\sin\theta(1+\cos\theta)J_0(k\rho\sin\theta)e^{ikz\cos\theta}d\theta, \\ I_{01} &= \int_0^{\theta_{max}} \sqrt{\cos\theta}\sin^2(\theta)J_1(k\rho\sin\theta)e^{ikz\cos\theta}d\theta, \\ I_{02} &= \int_0^{\theta_{max}} \sqrt{\cos\theta}\sin\theta(1-\cos\theta)J_2(k\rho\sin\theta)e^{ikz\cos\theta}d\theta. \end{aligned} \tag{85}$$

These integrals, with J_n being the nth-order Bessel function, have to be evaluated numerically. Figure 61 shows the intensity distribution in the focal plane of a high-NA objective. It becomes clear that the vectorial nature of the electric field has to be considered when one looks at the cross sections along the x- and y-direction of the focal field intensity in Figure 61 (b). The spot is not circular but elliptical in contrast to the paraxial approximation and scalar theories. It is elongated in the direction of the incident electric field polarization. This effect becomes more pronounced with increasing NA and is therefore important to describe our experiment accurately. In Figure 62 (a) the logarithmic intensity distribution along the propagation direction z is shown. The wave fronts as shown in the phase distribution in Figure 62 (b) cannot be described with circles as it has been done in Equation 78 and Figure 59. We will see in our experiment that we can switch on and off antenna radiation by simply changing the polarization of incident light. The rigorous description of the focal fields outlined here allows us to model accurately our experimental observations.

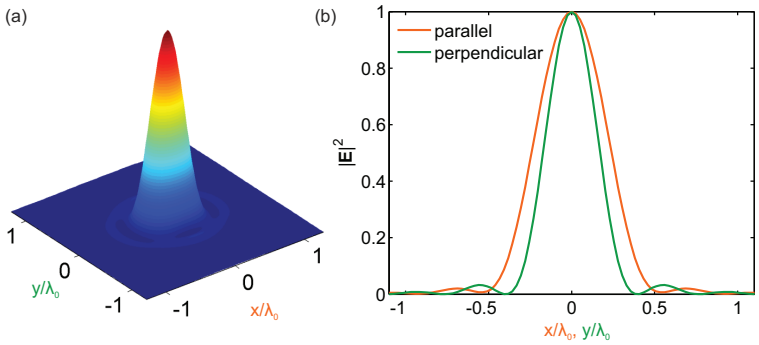

Figure 61: (a) Intensity distribution in the focal plane $z = 0$ of a high-NA objective for incident light polarized along the x-axis and incident wavelength λ_0. The NA is 1.4 and the refractive index n assumed to be 1.51. (b) Line-cuts of the intensity through the maximum along the x-direction (orange curve) and y-direction (green curve). The spot is elongated parallel to the direction of incident polarization due to the vectorial nature of the field [53].

6.2.3.3 *Resolution limit*

The resolution of our imaging setup is determined by its PSF. Each point source is convoluted with the PSF, which has a finite width and therefore closely spaced points might not be resolved. The finite width is a direct consequence of the filtering of the spatial frequency components $k_x^2 + k_y^2 > k^2$ that occurs on propagating the field from the source to its image in the far-field where evanescent waves are absent. Furthermore, due to the finite size of the collecting lens also propagating waves with high transverse spatial frequencies are lost, which can to a certain extend be avoided by using high-NA objectives.

The PSF is the image of a point source. After collimation of the emitted light by a reference sphere with focal length f refraction on a second reference sphere with focal length f' generates the image in the image plane. Similar to the previous section, the spatial angular representation allows us to describe the propagation of the dipole image after refraction

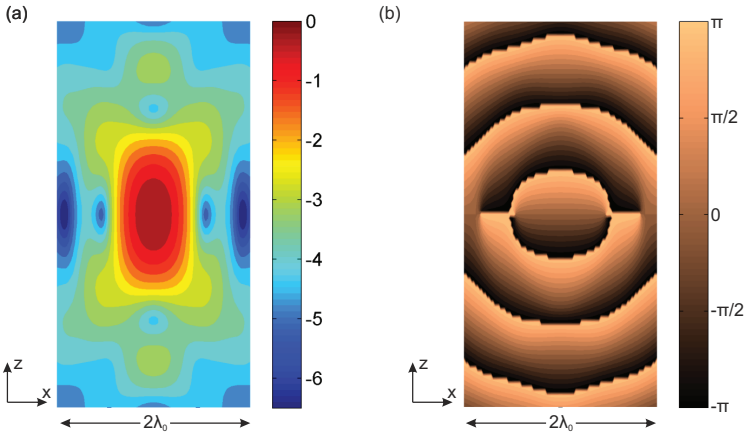

Figure 62: (a) The intensity distribution $|\mathbf{E}|^2$ (logarithmic scale) is plotted of a focused plane wave propagating along the z direction through the focus. The NA is 1.4 and the refractive index n assumed to be 1.51. (b) Phase distribution of E_x is shown.

at the second lens to its focus. It becomes for a x-polarized dipole $\mathbf{p} = p\hat{\mathbf{e}}_x$ and $f' \gg f$ [53]

$$\mathbf{E}(\rho, z = 0) = \frac{\omega^2 p^2}{\epsilon_0 c^2} \frac{ik'}{8\pi} \frac{f}{f'} \sqrt{\frac{n}{n'}} e^{i(kf - k'f')} \begin{pmatrix} \tilde{I}_{00} + \tilde{I}_{02} \cos 2\varphi \\ \tilde{I}_{02} \sin 2\varphi \\ 0 \end{pmatrix}. \quad (86)$$

The following abbreviations for the integrals have been used

$$\tilde{I}_{00}(\rho, z = 0) = \int_0^{\theta_{max}} \sqrt{\cos\theta} \sin\theta (1 + \cos\theta) J_0(k\rho \sin\theta / M) d\theta,$$
$$\tilde{I}_{02}(\rho, z = 0) = \int_0^{\theta_{max}} \sqrt{\cos\theta} \sin\theta (1 - \cos\theta) J_2(k\rho \sin\theta / M) d\theta, \quad (87)$$

which is similar to the expression found in Equation 84 when $z = 0$. The difference is that E_z becomes zero for $f' \gg f$ and the transverse magnification of the imaging system $M = \frac{n}{n'} \frac{f'}{f}$ is in the argument of

the Bessel function. Due to the vectorial nature of the field the image of the dipole is elliptical just as it is the case for the focal fields [see Figure 61 (b)].

In the paraxial approximation for low NA the PSF becomes the expression for the airy disk found as the diffraction pattern of a circular aperture [53]

$$|\mathbf{E}(\rho, z = 0)|^2 \propto \left[2\frac{J_1(k\rho \sin\theta_{max}/M)}{k\rho \sin\theta_{max}/M}\right]^2. \tag{88}$$

The Abbe criterion states that the resolution limit is the distance ρ_{min} between two dipoles where the maximum of one dipole's PSF coincides with the first minimum of the other dipole's PSF as shown in Figure 63. From Equation 88 we obtain

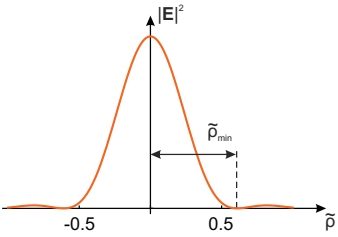

Figure 63: The Abbe criterion as the definition for the resolution limit is shown, where $\tilde{\rho} = \rho NA/(M\lambda)$.

$$\rho_{min} = 0.6098\frac{\lambda}{NA}M. \tag{89}$$

In confocal microscopy light coming from the sample is focused onto a pinhole in front of a detector. Depending on the choice of the pinhole only light intensity in the airy disk or close to the center of the PSF is detected. The total PSF can be determined as the product of excitation PSF and detection PSF, which leads to increased axial as well as a small increase in transverse resolution [53].

6.3 MODELING THE EXPERIMENT

The fluorescence signal at a point $\mathbf{r}$ that we measure in our experiment does not scale linearly with the intensity exciting the molecules at this point. It is shown in this section that saturation and bleaching play an important role when describing the fluorescence of dye molecules. We furthermore use a single dipole approximation model to describe the scattering response of a multiparticle system. This helps us to describe the scattering properties of an antenna array where several plasmonic dipole antennas are closely spaced and couple mutually. Together with the definitions of the focal fields from the previous section we develop a nonlinear model, which describes our experimental findings accurately.

6.3.1 *Modeling the fluorescence signal of dye molecules*

Besides vibrational transitions (see Chapter 5) electronic transitions in molecules are possible. The transition occurs between the highest occupied molecular orbital (HOMO) and the lowest unoccupied molecular orbital (LUMO) also involving higher vibrational states. After excitation from the ground state relaxation from the LUMO can occur radiatively usually to a higher vibrational state of the HOMO causing a Stokes-shift of the emitted photon or non-radiatively generating heat. In dye molecules radiative decay is the dominating process. The quality of a dye is quantified by its quantum efficiency

$$Q = \frac{k_r}{k_{nr} + k_r}, \tag{90}$$

where k_r is the radiative decay rate and k_{nr} the non-radiative decay rate. An energy level diagram (not showing the vibrational states) is displayed in Figure 64. An absorbed photon excites the system from its singlet ground state with the rate k_{01} to its singlet excited state (both spin 0). The lifetime of this state is usually on the order of 10 ns. From the excited state it can decay radiatively with a rate k_r or non-radiatively k_{nr} back to the ground state. Besides this, spin-orbit coupling can cause *intersystem crossing* with a rate k_{ISC} to a triplet state with spin 1. From

there it decays non-radiatively to the ground state with rate k_{nrT} corresponding to a lifetime on the order of milliseconds. This lifetime is very long since the relaxation is a spin forbidden transition. Interaction with

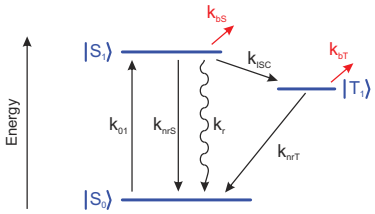

Figure 64: Energy level scheme to model a fluorescent molecule. The system gets excited from the singlet ground state $|S_0\rangle$ to the singlet excited state $|S_1\rangle$ with rate k_{01} via laser irradiation. From there it can decay radiatively k_r or non-radiatively k_{nrS} to the ground state or with k_{ISC} to the triplet state $|T_1\rangle$ and from there further with k_{nrT} to the ground state. The system is disturbed by bleaching, which can occur in the excited singlet state $|S_1\rangle$ with rate k_{bS} or in the triplet state $|T_1\rangle$ with rate k_{bT}.

oxygen or other chemicals in the surrounding can stop the molecule to fluoresce. This is known as photobleaching [259]. We assume in our model that photobleaching can occur from the singlet excited state with a photobleaching rate k_{bS} as well as from the triplet state with k_{bT}. It is a valid assumption for a dye molecule to consider the bleaching rates k_{bS} and k_{bT} being much smaller than the other rates. This allows us to consider the bleaching process as a small perturbation to the system and we can first find expressions for the population of the different states without bleaching. The dynamics of the probability to find the molecule in one of the three states (s_0, s_1, t_1) can then be described as [53]

$$\begin{aligned}
\dot{s}_0 &= -k_{01}s_0 + (k_{nrS} + k_r)s_1 + k_{nrT}t_1 \\
\dot{s}_1 &= k_{01}s_0 - (k_{nrS} + k_r + k_{ISC})s_1 \\
\dot{t}_1 &= k_{ISC}s_1 - k_{nrT}t_1
\end{aligned} \tag{91}$$

where $s_0 + s_1 + t_1 = 1$ has to be fulfilled and the dot denotes time derivation. Here, we are interested in the steady-state solutions of the equation

system since we are using continuous light to excite the fluorescence in the dye molecules. By setting the left part of the equations in Equation 91 to 0 we can find expressions for (s_0, s_1, t_1). The excitation rate is proportional to the incident intensity I

$$k_{01} = \frac{\sigma}{\hbar\omega} I, \tag{92}$$

where σ is the absorption cross section [53]. The rate at which photons are emitted $F_r(I)$ can now be expressed as a function of the incident intensity and the decay rates of the system:

$$\begin{aligned} F_r(I) &= k_r s_1 = F_{r,\infty} \frac{I/I_S}{1 + I/I_S}, \\ F_{r,\infty} &= \frac{k_r k_{nrT}}{k_{nrT} + k_{ISC}}, \\ I_S &= \frac{(k_{nrS} + k_r + k_{ISC}) k_{nrT}}{\sigma(k_{nrT} + k_{ISC})} \hbar\omega. \end{aligned} \tag{93}$$

In the case of bleaching the rate at which molecules cease to fluoresce is given by

$$F_b = k_{bS} s_1 + k_{bT} t_1, \tag{94}$$

which is proportional to the fluorescence rate F_r

$$F_b(I) = \frac{k_{bS} k_{nrT} + k_{ICS} k_{bT}}{k_r k_{nrT}} F_r(I) = F_{b,\infty} \frac{I/I_S}{1 + I/I_S}. \tag{95}$$

Therefore the bleaching in our system can be described with the same saturation intensity as the fluorescence. In the experiment we expose our sample for time Δt and integrate the signal. The number of bright molecules $n(t)$ decreases with time due to photobleaching following the temporal evolution described by the differential equation

$$\dot{n}(t) = -F_b(I) n(t). \tag{96}$$

This gives us the number of fluorescent molecules at a certain time t as

$$n(t) = n(t_o) e^{-F_b(I)(t - t_o)} \tag{97}$$

starting from a population $n(t_o)$. The signal we detect at a time t is then $F_r(I) \cdot n(t)$, which gives us after integration the measured intensity recorded during the exposure time Δt:

$$s(t_o) = \int_{t_o}^{t_o+\Delta t} F_r(I) \cdot n(t) dt = \frac{F_{r,\infty}}{F_{b,\infty}} n(t_o)(1 - e^{-F_b(I)\Delta t}). \tag{98}$$

Equation 98 describes the spatial and temporal response of dye molecules imaging an intensity pattern $I(\mathbf{r})$ via their fluorescence. It takes into account saturation and bleaching.

6.3.2 *Point-dipole model for multiparticle scattering*

We develop here a self-consistent model to describe the response of an ensemble of dipoles. It is necessary to account for the mutual coupling between closely spaced scatterers where the excitation of one scatterer is due to the incident field and the fields generated by the other scatterers. For plasmonic particles, which are small compared to the incident wavelength higher order excitations can be neglected and it is valid to describe each particle in the ensemble with a point current source (Equation 15) generating a dipole field. The total electric field at $\mathbf{r}_j$ following Equation 13 then becomes

$$\mathbf{E}(\mathbf{r}_j) = \mathbf{E}_{inc}(\mathbf{r}_j) + \mu_o \omega^2 \sum_{k \neq j} \overline{\mathbf{G}}(\mathbf{r}_j, \mathbf{r}_k) \mathbf{p}(\mathbf{r}_k) \tag{99}$$

where $\mathbf{E}_{inc}$ is the incident field. A simple reorganization with the additional relations

$$\begin{aligned} \overline{\mathbf{A}}_{jk} &= -\mu_o \omega^2 \overline{\mathbf{G}}(\mathbf{r}_j, \mathbf{r}_k) \\ \mathbf{p}(\mathbf{r}_j) &= \alpha_j \bar{\mathbf{I}} \mathbf{E}(\mathbf{r}_j) = \overline{\mathbf{A}}_{jj}^{-1} \mathbf{E}(\mathbf{r}_j) \end{aligned} \tag{100}$$

gives the linear equation system [260]

$$\sum_{k=1}^{N} \overline{\mathbf{A}}_{jk} \mathbf{p}_k = \mathbf{E}_{inc}(\mathbf{r}_j). \tag{101}$$

After solving it for the dipole moments $\mathbf{p}_{1...N}$ the total electric field can be calculated by summing up the incident field and the dipole fields generated by these dipole moments following Equation 16.

By using the identity matrix in Equation 100 we assume particles with isotropic polarizabilities. In our experiment we have dipole antennas, which are resonant for x-polarized light and off-resonant for the other directions so that we consider only the x-component of the dipole moments when we model the scattering response. The complex polarizability α can be calculated from the current distribution and the incident electric field via

$$\int \mathbf{j} dV = i\omega\alpha \mathbf{E}_{inc} \tag{102}$$

where the integration is over the volume V of the scatterer. We obtain the current distribution and the incident field from numerical simulations where we simulate a 120 nm long, 60 nm wide and 40 nm thick gold antenna at $\lambda = 785$ nm. With this α becomes $8.1 \cdot 10^{-4} - i7.1 \cdot 10^{-4}$ Cm^2/V.

6.3.3 *Fitting function*

In the previous three sections we developed the model, which allows us to fully describe our fluorescence experiment:

1. We found an expression for the fluorescence of dye molecules as a function of time and intensity. It accounts for bleaching and saturation.

2. We can describe the electric field of an incident laser beam focused by a high-NA objective in different planes $z = \text{const.}$ perpendicular to the propagation direction.

3. We can solve self-consistently for the dipole moments in an antenna array excited by an incident field. This allows us to calculate the coherently scattered field.

In this section we put these parts together to obtain an expression, which we fit to our experimental data.

In our experiment we use *IR-140*[9] as dye molecules to image the radiation pattern of an antenna array. From measurements on a continuous film of molecules we find that the temporal response is accurately described by assuming two different molecular populations with two different decay rates. Equation 98 therefore has to be extended with a second term and becomes

$$s[N\Delta t, I(\mathbf{r})] = \frac{s_1}{c_1} e^{c_1 \Delta t \sum_{k=1}^{N-1} f_k[I(\mathbf{r})]} (1 - e^{-c_1 f_N[I(\mathbf{r})]\Delta t}) + \frac{s_2}{c_2} e^{c_2 \Delta t \sum_{k=1}^{N-1} f_k[I(\mathbf{r})]} (1 - e^{-c_2 f_N[I(\mathbf{r})]\Delta t}). \quad (103)$$

We are subsequently recording N images each with an integration time Δt. The respective first exponential functions describes the bleaching due to previously ($k = 1...N-1$) recorded frames giving us the starting population for the Nth image.

After each frame we alternate the incident polarization from along the long-axis of the antennas (x-polarization, see Figure 68), where we resonantly excite the antennas, to perpendicular to it, where scattering of the antennas is negligible at the incident wavelength $\lambda = 785$ nm (see Figure 65). As a consequence, the intensity function

$$f_k[I(\mathbf{r})] = \frac{I_k/I_S}{1 + I_k/I_S} \quad (104)$$

around the scattering antennas has to be calculated for each polarization separately. For off-resonant polarization the intensity I_k exciting the dye molecules solely stems from the y-polarized focused laser beam

$$I_y(\mathbf{r}) = |\mathbf{E}_{inc,y}(\mathbf{r})|^2, \quad (105)$$

where the field $\mathbf{E}_{inc,y}(\mathbf{r})$ is calculated following Equation 84 and a y-polarized incident beam is assumed. For resonant polarization (x-polarization) the scattering response of the antennas has to be added. In our experiment we are applying single dipole antennas and antenna arrays with two to five elements arranged in a linear chain. We can calculate the dipole moments self-consistently with Equation 101 using the

9 Sigma-Aldrich, Germany

complex values of incident field at the position of the antennas (Equation 84). This allows us to calculate the full scattered field by adding up the electric fields of the N dipoles generated by the dipole moments using Equation 16. The intensity then becomes

$$I_x(\mathbf{r}) = |\mathbf{E}_{inc,x}(\mathbf{r}) + a \sum_{k=1}^{N} \mathbf{E}_{dip,k}(\mathbf{r})|^2 \tag{106}$$

where a is a parameter to account for fabrication deviations altering the polarizability α derived from numerical simulations.

The image that we record is convoluted with the PSF of our microscope. As we have seen previously the PSF is similar to the expression for the focal field. We therefore use this expression to compute the PSF of our system for $z = 0$ at the luminescence wavelength $\lambda = 850$ nm. We use circularly polarized light incident on the objective for calculating the PSF

$$I_{PSF}(\mathbf{r}) = |\mathbf{E}_{circ}(\rho, \varphi, z = 0)|^2. \tag{107}$$

Using Equation 104 to Equation 106 with Equation 103 and convoluting it with the expression for the PSF in Equation 107 we obtain the expression to fit our experimental data

$$(s * I_{PSF})(\mathbf{r}) = \int_{-\infty}^{\infty} s[N\Delta t, I(\mathbf{r}')] I_{PSF}(\mathbf{r} - \mathbf{r}') d\mathbf{r}'. \tag{108}$$

6.4 RESONANT SCATTERING OF A SINGLE DIPOLE

A nanoantenna link consists of a transmitting antenna and a receiving antenna. Here, we focus first on the transmitting antenna. The fundamental building block is a dipole antenna. In this section we design the dipole nanoantenna to be in resonance with the driving laser field. We then measure the resonantly scattered dipolar fields with our fluorescence method.

6.4.1 *Design of the antenna*

We use numerical simulations to find the geometrical lengths of a single gold nanoantenna. The calculated scattering cross section for a 100 nm long gold antenna (width 50 nm, height 40 nm) is shown in Figure 65 (a). The structure is embedded in a homogeneous environment with refractive index $n = 1.5$. This is the configuration used in the experiment where the substrate is index matched with immersion oil. The

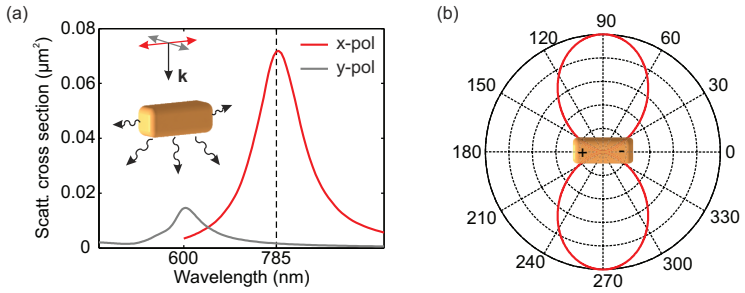

Figure 65: (a) For a 100 nm long gold antenna (width 50 nm, height 40 nm) the numerically calculated scattering cross section is resonant at 785 nm (black dashed line) for x-polarized incident light (red) and off-resonant for the perpendicular polarization (gray) in a homogeneous environment with refractive index $n = 1.5$. (b) Numerically calculated far-field scattering pattern in the plane of the antenna for excitation along the long-axis (x-polarization) at 785 nm. The two dipole lobes spread out along the y-direction.

aspect ratio is 2, which therefore gives two distinct resonances for incident waves polarized along the long-axis (x-polarization, red curve) and the short-axis (y-polarization, gray curve) of the antenna. Since the wavelength of our laser diode is $\lambda = 785$ nm (black dashed line) we can *switch* the resonant scattering of the antenna *on* and *off* by changing the incident polarization from x to y. In the case of resonant scattering the pattern has a dipolar shape where the two lobes are pointing along the y-direction [Figure 65 (b)]. From the width of the resonance one deduces a 50 THz bandwidth of the plasmonic dipole antenna. This en-

ables transmitting multiple channels of data across this large bandwidth using frequency-division-multiplexing.

In order to measure the resonances we fabricate arrays of dipole antennas changing the periodicity along the x-direction. Figure 66 (a) shows two SEM micrographs of the structures. By fabricating $100 \times 100\ \mu m^2$ sized arrays the resonances can be measured with conventional FTIR spectroscopy. The extinction spectrum of the array is similar to the one for single antennas due to the homogeneity of the antennas and the large periodicity (left image) so that near-field coupling between the individual antennas can be neglected. For closely spaced antenna elements near-field coupling sets in and the fundamental resonance is red-shifted for a fixed antenna length. In Figure 66 (b) we plot the transmittance spectra for the two different samples and incident polarizations along the long and short axis of the antennas. The antennas in the closely spaced

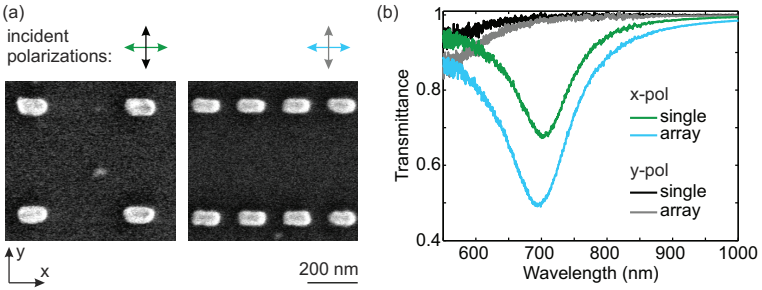

Figure 66: (a) SEM micrographs of individual dipole antennas (left panel) and arrayed dipole antennas along the x-direction (right panel). The polarization of incident light is either along the long axis of the antennas (x-polarization) or perpendicular to it (y-polarization). The length of the individual dipole antennas is 125 nm and of the dipoles in the array 115 nm to account for near-field coupling. The distance between adjacent antennas in the array is 170 nm. (b) FTIR transmittance measurement on the structures in (a) with incident polarizations color-coded as indicated in (a). A resonance is observed in the given spectral region for incident x-polarized light.

configuration are 10 nm shorter than for the large periodicity (115 nm

and 125 nm, respectively), which will be important for the design of antenna arrays in the next section. This accounts for the near-field coupling so that in both cases the resonances for x-polarized incident light occur around 700 nm. Overall the experimentally realized antennas are slightly longer than numerically optimized antennas resonant to $\lambda = 785$ nm in an environment with $n = 1.5$ [see Figure 65 (a)]. For the perpendicular direction the resonance is far blue-shifted as also expected from the numerical simulation.

For the FTIR measurements the antennas were not yet covered with the fluorescent polymer layer and immersion oil to avoid bleaching the molecules. Covering the structures with a dielectric halfspace will lead to a red shift of the plasmon resonances due to the larger refractive index of the covering medium. This red-shift is predicted in numerical simulations of the periodic arrangements shown in Figure 67. In panel

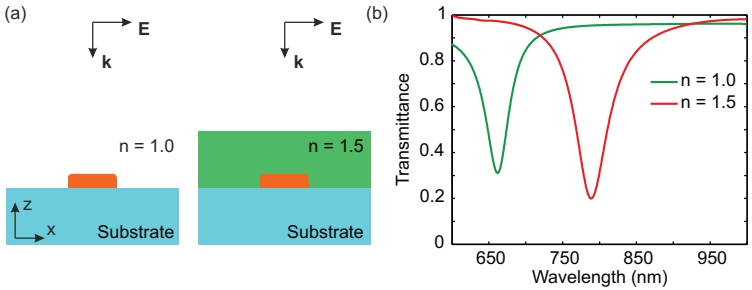

Figure 67: Influence of the superstrate on the transmission of the samples predicted with numerical simulations. (a) The antennas (orange, length 100 nm, width 50 nm, height 40 nm) are on a glass substrate ($n = 1.5$) and either not covered (left configuration) or covered with a dielectric material ($n = 1.5$, right configuration). The incident polarization is along the x-direction. (b) Numerically simulated transmittance spectra for the two configurations shown in (a). A pronounced red-shift is observed for the covered structure, which tunes the plasmon resonance to 785 nm.

(a) we show the schematic sideviews of the sample with large periodicity (only one antenna shown) for air and dielectric halfspace. The incident

polarization is along the long axis of the antennas (length 100 nm). Figure 67 (b) is the numerically calculated transmittance spectrum of the periodic arrangement where the resonance of the covered structure (red curve) is red-shifted to $\lambda = 785$ nm. Compared to the numerically calculated resonance of the uncovered structure (green curve) the measured resonance [see Figure 66 (b)] is slightly red-shifted due to the longer elements in experiment. From this we infer that by covering our sample the resonance will red-shift beyond the aimed 785 nm. Even though this is not ideal, we observe enhanced scattering at $\lambda = 785$ nm because of the large width of the scattering cross section of the plasmonic antenna [see Figure 65 (a)].

6.4.2 *Experimental configuration to measure the radiation pattern*

We next map the radiation pattern of the nanoantennas. The sample is covered with a fluorescent polymer layer and embedded in immersion oil (details given in Section 6.2). The refractive indices of the glass substrate, polymer layer, and immersion oil are 1.52, 1.48 and 1.52, respectively. This provides on the one hand an almost homogeneous environment avoiding deflection of the radiation into the substrate and on the other hand cancels out the possibility of waveguiding effects in the polymer layer due to its slightly lower refractive index compared to the adjacent glass and oil. Figure 68 shows the geometry used in the experiment. We use focused incident laser light at $\lambda = 785$ nm polarized along the long axis (x-polarization) and short axis (y-polarization) of the antennas, which leads to enhanced scattering and no scattering, respectively, of the antennas as discussed in the previous section. We depict here a five dipole array as transmitter (SEM micrograph). The dye molecules absorb at $\lambda = 785$ nm and have their emission maximum around $\lambda = 850$ nm. The radiation pattern is observed in the xy-plane by taking wide-field images of the fluorescence intensity, which depends on the local intensity. As discussed previously, the recorded signal follows a nonlinear function of intensity due to bleaching and saturation of the molecules and is dependent on previous exposures of the sample. This

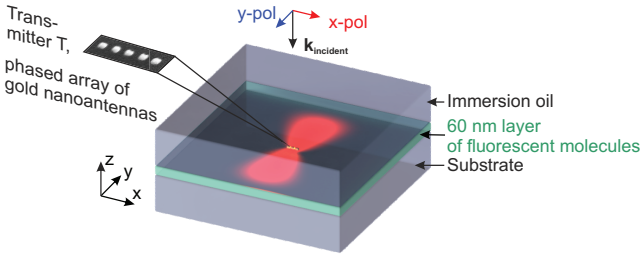

Figure 68: The antenna transmitter T is on a glass substrate ($n = 1.52$), subsequently spin-coated with a 60 nm thick layer of PMMA with fluorescent molecules ($n = 1.48$), and then covered with immersion oil ($n = 1.52$). The incident laser light ($\lambda = 785$ nm) propagates along the z-direction and is either x-polarized (resonant scattering) or y-polarized (off-resonant, no scattering). A wide-field image of the fluorescence in the xy-plane measures the in-plane radiation pattern.

will become important later when we fit our experimental observations using our model.

Figure 69 shows the fluorescence image around the antenna. When the antenna is excited with x-polarized light [Figure 69 (a) left panel] we observe that the intensity distribution is elongated along the y-direction. This is in good agreement with the theoretical dipole pattern in Figure 65 (b) of an x-oriented dipole. This preference along one direction is gone for y-polarized incident light [Figure 69 (a) right panel]. In this case the fluorescence intensity stems from the incident laser spot since the scattering from the antenna is too weak to be detected. We plot here the raw data with the background subtracted. The background is acquired with the laser turned off during image acquisition. The background corrected images are then normalized to the maximal value of the luminescence for x-polarized excitation.

In panel (b) we plot the intensity on a circle around the transmitter with mean radius 9 µm, which is indicated by the white dashed lines in (a). The effect of the antenna is clearly visible as the two lobes at the azimuthal angles $\varphi = 90°$ and $\varphi = 270°$, which corresponds to the

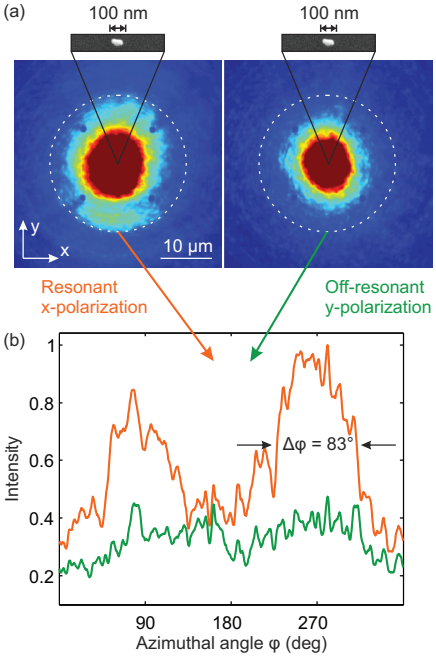

Figure 69: Radiation pattern of a dipole antenna in the xy-plane. (a) The fluorescence intensity in the xy-plane is shown when a single dipole antenna is excited with x-polarized (left panel) and y-polarized light (right panel). A stretching out of the intensity distribution along the y-direction is observed in the resonant case in contrast to the off-resonant case where the fluorescence intensity is isotropic. (b) The fluorescence intensity along the white dashed circle in (a) is plotted for resonant (orange) and off-resonant (green) incident polarization. The two lobes along the y-direction (90° and 270°) in the resonant case are due to the dipolar scattering from the antenna.

y-axis direction. We extract the angular width $\Delta\varphi$ of the luminescence pattern, which is the full width at half maximum of the peak at 270° excluding the offset due to direct excitation of the molecules by the incident laser beam. For the single antenna it is 83°. This quantity serves in the following as measure for the directionality of the transmitted radiation. A smaller beam width means that more intensity is channeled

in this direction, which would increase power transfer in a nanoantenna link.

6.5 INCREASING THE DIRECTIVITY WITH ANTENNA ARRAYS

As we have seen in the previous section a single dipole antenna with deep sub-wavelength dimensions leads to directional redistribution of radiation along a certain direction. We have also learned from antenna theory that a coherently driven antenna array increases directivity due to constructive interference. In this section we expand our single dipole nanoantenna by fabricating antennas in a linear chain along the long axis of the antennas as is shown in the SEM micrographs in Figure 70 (a). The distance between adjacent elements is 170 nm and the individual antenna length is 115 nm, which corresponds to the sample parameters with small periodicity in Figure 66.

In Figure 70 we compare the fluorescence experiment for the single antenna to nanoantenna arrays with three and five dipole elements. Panel (a) is the fluorescence intensity when we drive the transmitters with polarized light along the x-direction. As expected, the intensity distribution for the nanoantenna arrays is also elongated in the y-direction. Importantly, the signal along this direction increases by adding elements to the array, which is also associated with a narrowing of the pattern. A clear antenna array effect is observed, which completely vanishes for excitation with incident y-polarized light as shown in panel (b). The beamwidth decreases from the 83° of the single dipole to 52° and further to 35° for the three and five dipole arrays. The physical reason is that the individual dipoles are driven in phase and the dipole fields add up coherently. This leads to constructive interference on the y-axis. For all cases the scattering along the y-direction vanishes when the antenna arrays are switched off, which is further proven by the flat curve in the cross sectional plots in panel (c).

As we have pointed out the observed fluorescence pattern does not directly represent the intensity of the sum of incident and scattered electric field. Bleaching and saturation of the dye molecules as well as the

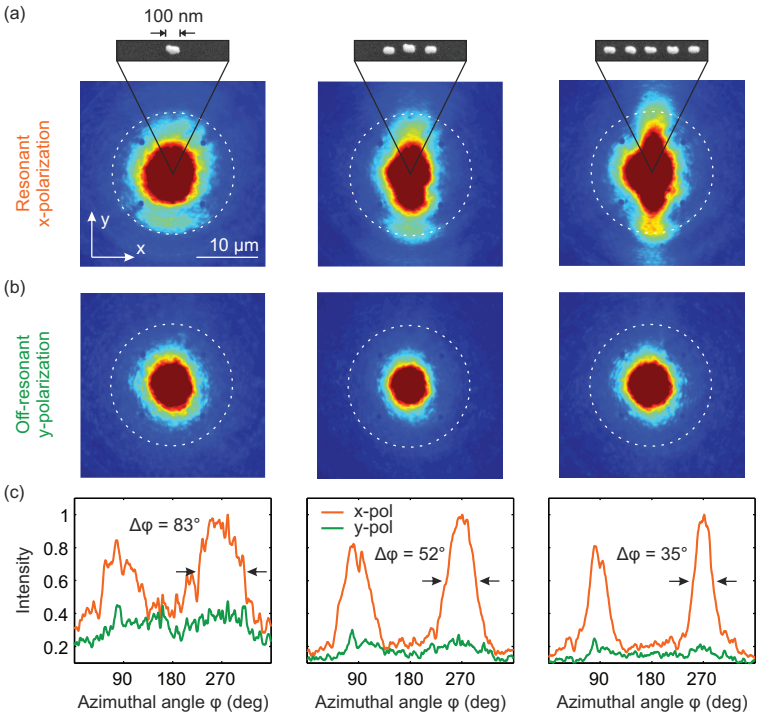

Figure 70: (a) x-polarized light is incident on a single antenna (left), three dipole array (center), and five dipole array (right). The radiation along the y-direction gets stronger with increasing number of elements. (b) As a control we show the pattern for incident y-polarization. No antenna pattern is observed for all three cases. (c) The intensity distribution along the white circles in (a) and (b) is plotted for both polarizations. A narrowing of the lobes (decreasing beamwidth $\Delta\varphi$) along the y-direction is observed for increasing number of antenna elements in the array.

PSF of our imaging system has to be taken into account to model the experimental data. A direct conclusion from the in-plane radiation pattern on the directivity is therefore not possible. Figure 71 shows that our nonlinear model (Equation 108) describes accurately the experimental observations. In addition to the three transmitter configurations dis-

cussed above we also investigate nanoantenna arrays with two and four elements. All patterns for resonant excitation are shown in the top row

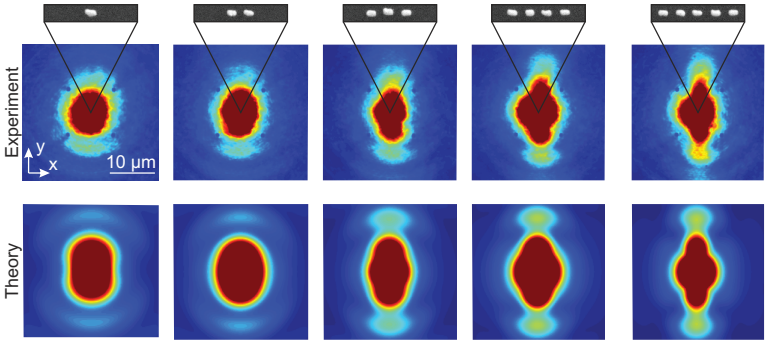

Figure 71: A comparison of the experimental fluorescence patterns (first row) to the fit of the nonlinear bleaching model (second row) is shown for a single dipole and arrays with two to five elements (left to right). The parameters describing the fluorescent film are fitted once for the five dipole array and then used for all the other fits by leaving the magnitude of the polarizability as only fitting parameter.

of Figure 71, which we compare to our model in the bottom row. To obtain the parameters characterizing the luminescent molecules, I_S, s_1, s_2, c_1, and c_2, we fit the experimental data for the five dipole antenna array to the theory (see Equation 108), shown in the right most column of Figure 71. We then use these parameters to fit all the other data to the model using a as the only fitting parameter. This accounts for small variations in the fabricated devices, which alter the dipole moment. The fitted patterns reproduce the essential indicators for increased directivity for larger antenna arrays, namely larger signal into the positive and negative y-direction as well as narrowing of the fluorescence intensity pattern.

It is of interest for future on-chip integration of our device to find an optimal configuration, which is nanoscale but still provides high directivities. We therefore plot the beam width as a function of antenna elements in Figure 72. It is extracted from experiment in panel (a) and from

the fitted pattern in panel (b) showing good agreement. In both plots we

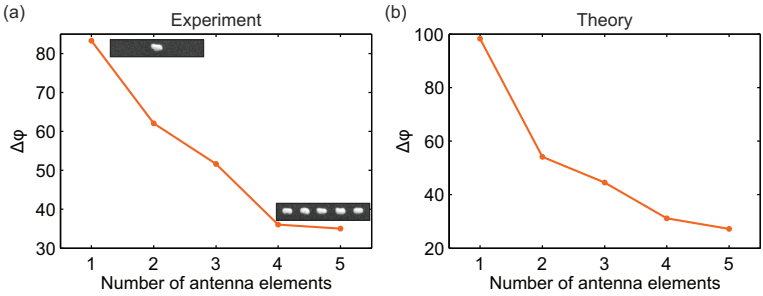

Figure 72: (a) Experimental and (b) theoretical values of $\Delta\varphi$ as a function of the number of antenna elements. Due to the finite width of the incident focused laser beam an array with more than five antenna elements does not provide further narrowing of the radiated beam.

observe that adding more elements to the five elements would not significantly enhance the directivity. This saturation behavior is understood when we remember that the intensity of our driving focused beam decays away from the center (Figure 61). As a consequence, increasing the number of elements in the array means also that the outermost antennas get less efficiently excited and do not contribute significantly to the radiation pattern. Here, an optimal trade-off regarding directivity and nanoscale footprint is realized with the five dipole array as transmitter (footprint 850×50 nm^2).

Finally, since we know the magnitude and phase of the focused incident field at the position of the dipole antennas we can calculate with the polarizability and the self-consistent theory the dipole moments. From this we determine the fields and the Poynting vector, which we use to calculate the directivity pattern. We show in Figure 73 the 3D radiation patterns for the single dipole, three and five element array and their cross sections in the xy-plane. The maximal directivity is along the y-direction and indicated for the different transmitter configurations where we find a maximum of 3.7 for the five dipole array. Here we use as basic element a simple dipole antenna. In the future, more sophisticated

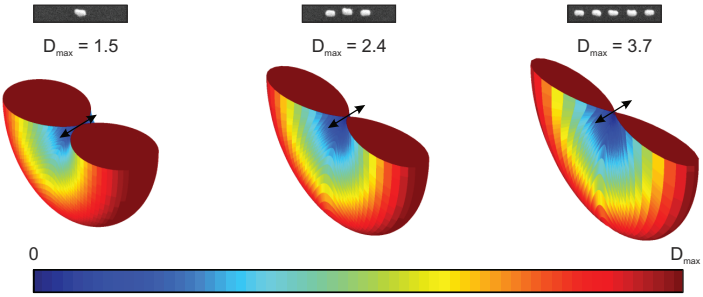

Figure 73: 3D radiation patterns of the single dipole, three dipole array, and five dipole array, calculated with the dipole moments induced by the incident focused laser beam. The arrows indicate the orientation of the dipole moments and the pattern is cut in the xy-plane.

designs of transmitting antenna [33, 85] will boost the directivity even further. This means that the power transfer is enhanced following Equation 74 where the directivity of the receiving antenna plays an equally important role. A big step for increased directivity is made by expanding the array to a two-dimensional configuration (see Chapter 4) since the radiation pattern gets narrowed in two orthogonal planes. This goes of course at the cost of larger footprint and would require a 3D arrangement for signal transfer in the xy-plane. Recently, directional scattering from single element antennas was demonstrated [261–263], which favors small footprint but does not allow beam steering as we will demonstrate later by phasing the antenna array.

6.6 POINT-TO-POINT WIRELESS LINK WITH PLASMONIC NANOANTENNAS

A point-to-point nanoantenna link is demonstrated in Figure 74. As a transmitter the five dipole array is employed, which is surrounded by nanoantenna array receivers. We saw in the previous section that the directivity of the transmitter is enhanced leading to a efficient power transfer. The structure is depicted in the SEM micrograph of panel (a).

Receiver arrays with five dipoles R_{10} are positioned at a distance of 10 µm in the x- and y-direction to the transmitter T. At a distance of 20 µm

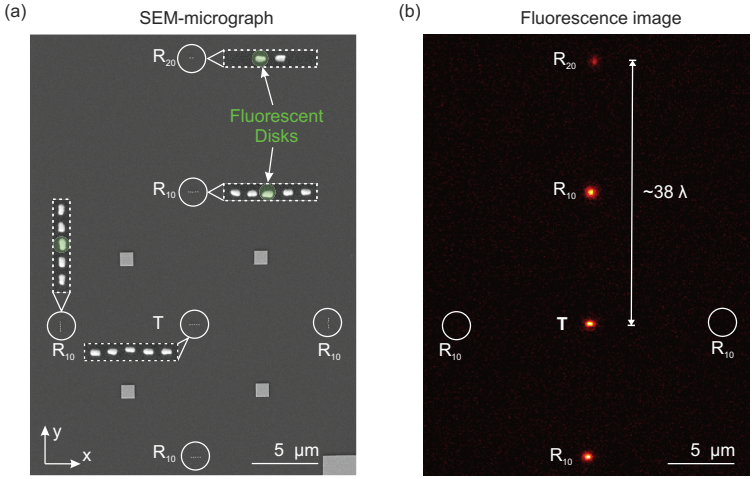

Figure 74: (a) SEM micrograph of the point-to-point antenna link. The transmitter T is a five dipole array and receiving arrays R_{10} and R_{20} are positioned along the radiation direction (y-direction) at a distance of 10 µm and 20 µm, respectively. As a control, receiving arrays are also fabricated 10 µm away from transmitter T in the x-direction. Each receiving array is equipped with a fluorescent dye disk. (b) Fluorescence image of the configuration when the transmitter T is excited with x-polarized incident light. The radiated signal is picked up by the receivers R in the y-direction.

in the positive y direction we position a receiving two dipole array R_{20}. Each receiving array is equipped with a fluorescent dye disk to record the received signal via fluorescence. As shown in Figure 75 the antenna link is embedded in a homogeneous environment, which minimizes the perturbation of the radiation pattern in the xy-plane.

Figure 74 (b) is the fluorescence image when the transmitter is excited with incident polarization along the x-direction. Consequently, the dye disks coupled to the receiving arrays in this direction light up whereas the receivers in the perpendicular direction remain dark. This proves for

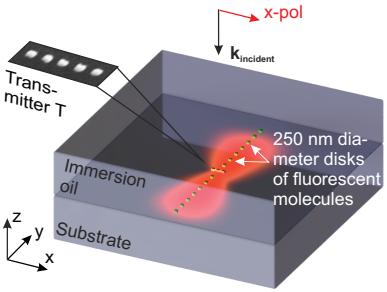

Figure 75: Geometry to measure power transfer efficiency in a wireless point-to-point link. After fabrication of the antenna, fluorescing dye disks with diameter 250 nm are positioned in a chain along the y-direction and x-direction up to 20 µm away from the antenna. The transmitting antenna T is oriented along the x-direction and resonantly driven with x-polarized incident light. The structure is covered in immersion oil.

the first time power transfer based on the radiation of optical nanoantennas. Due to the still very clear signal 20 µm away even larger transmission distances are easy to realize. We are only limited here by the field of view of our experiment to a maximal distances of 20 µm, which is of course not the limit of power transmission with optical antennas.

We have seen so far that the antenna link enables power transmission across large distances. We expect this from the theoretical prediction of Equation 74 and Figure 56 where free space radiation as transmission channel decays as $1/d^2$. Still, we lack the proof that this is indeed the case for our nanoantenna link and the necessity of using a plasmonic antenna to enhance the received power becomes not apparent from this experiment. To investigate on this experimentally we fabricate chains of sub-wavelength sized disks of fluorescent dye molecules around a transmitter antenna array along the x- and y-direction up to a distance of 20 µm, which is the border of our field of view. The two furthest dye disks are positioned on top of plasmonic disks, which serve as receiving antennas. A schematic of the structure and the background corrected fluorescence image is shown in Figure 76 when the transmitter is excited with x-polarized light. Due to the antenna radiation along the y-direction the

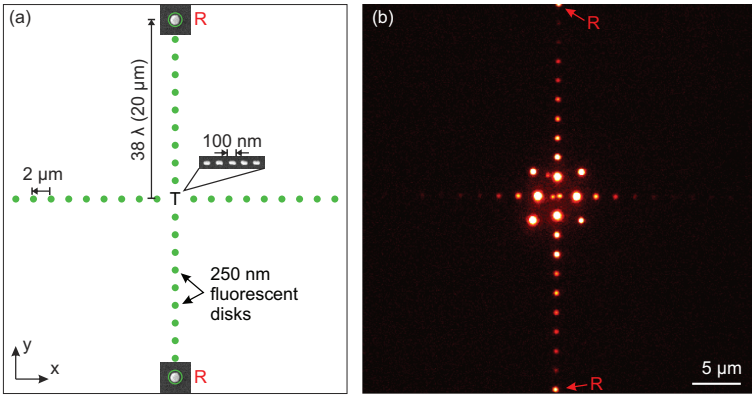

Figure 76: (a) Schematic of the experimental geometry. The transmitter array T is a five dipole antenna array and positioned in the center of two crossing linear chains of 250 nm dye disks. Dye disks with a distance of 20 µm (corresponding to 38 λ in the medium) to the transmitter in the y-direction are equipped with a plasmonic receiver antenna R. (b) Fluorescence wide-field image of the configuration when the transmitter T is excited with x-polarized light. The power of the incident laser beam is in this case 80 µW. Disks along the x-direction light up due to the incident beam whereas the radiation from the antenna along the y-direction is observed. Dye disks equipped with receiving antennas R show a clear intensity enhancement. The four additional dots in a square lattice around the transmitter serve as alignment markers to center the incident beam on the transmitter array.

intensities of the fluorescent dye disks decay slower with distance than the intensity of the fluorescent dye disks along the x-direction, which are only excited by the incident beam. Strikingly, the dye disks, which contain the plasmonic receiver exhibit a distinct enhancement of the received signal being comparable to the signal from the receivers positioned at 6 µm and 8 µm distances. In order to quantify these two effects, the intensity decay along the y-direction and the influence of the plasmonic receiver, we plot the fluorescence intensity as a function of distance in Figure 77. We use excitation powers of 1 µW, 5 µW, 10 µW, 20 µW, 30 µW, 40 µW, 50 µW, 60 µW, 70 µW, and 80 µW encoded by the

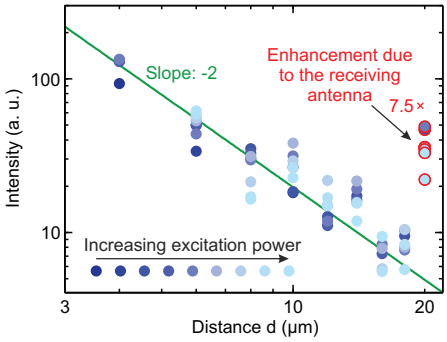

Figure 77: Free-space power transfer of a point-to-point nanoantenna link. Fluorescence intensity of the dye disks is shown measured with different incident powers to increase the dynamic range. A $1/d^2$ power decay is plotted for comparison (green curve), which is in very good agreement with the fluorescence intensity from the dye disks at different distances. A $7.5\times$ receiving enhancement is obtained when a plasmonic antenna is picking up the signal at $d = 20$ μm.

blue color of the plotted data. The dynamic range of our measurement is in this way enlarged: For low excitation power the luminescence of the receivers close to the transmitter scales linearly with the excitation power and the dye is not significantly bleached. As the excitation power is increased, this linear regime is shifted to larger distances from the transmitter, allowing us to obtain data with high signal-to-noise ratio over the whole distance range. The plotted data is finally normalized with the respective excitation power value. Together with the data from the fluorescent disks we plot a $1/d^2$ decay (green line). The good agreement with our experimental data proves that we obtain power transfer via free space propagation. This is much less lossy then the exponential decay of plasmonic waveguides and enables signal transmission across large distances.

We exclude from this plot the fluorescence of dye disks with low signal-to-noise ratio and those which are mostly excited by the incident laser beam. This is important to draw quantitative conclusions from the experiment. To do this, we first determine the signal for each receiver by

summing up the luminescence signal in the pixels falling within a 700 nm diameter area around each receiver. The background signal for each receiver is obtained by taking the mean signal on a circular ring around the receiver with inner diameter 1000 nm and outer diameter 1400 nm. We estimate the noise of our images from the standard deviation of the background signal and only plot then the signal for the receivers where the signal per pixel is twice the noise. The contribution due to direct excitation of the receiver by the incident laser beam can be estimated from receivers placed in the orthogonal x-direction. We compare for each distance the signal for receivers in the x- and y-directions and exclude the data points for which the ratio of the two is larger than 0.3. To obtain the green line we take the mean of the signals at each distance and fit the offset y_0 of a y_0/d^2 decay.

By taking the ratio of the mean of the antenna signals at the position of the plasmonic receiver disk (circles with red rim in Figure 77) and the intensity without antenna (value on green line at 20 μm) a 7.5× enhancement of the fluorescence intensity is observed. This is due to the plasmonic nanoscale confinement of incident radiation exciting the dye molecules in the sub-wavelength volume of the resist disk. In Figure 78 we show with numerical calculations that this enhancement depends on the overlap of the sub-wavelength receiver dye disk and the plasmonic mode of the antenna. In this plot we change the diameter of the fluorescent disk and calculate the ratio of the integrated intensity in the disk with plasmonic disk antenna (diameter 145 nm) and without antenna. This is in good agreement with our experimental observation where the nominal size of our fluorescent disks is 250 nm. The slightly higher value of 7.8 compared to the numerical calculation for a 250 nm diameter disk indicates that the real diameter is actually smaller.

For intra-chip communication between nanoscale integrated devices, data links across distances of several hundred microns are desirable. We have seen so far that the nanoantenna link is low-loss and at the same time allows nanoscale confinement of the transmitted and received signal, which makes it a very promising component for high-density integration in photonic chips.

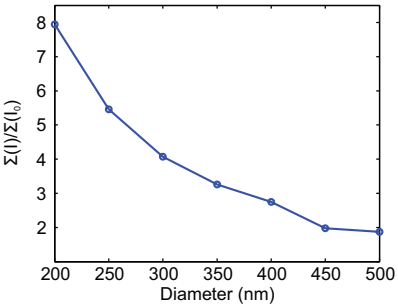

Figure 78: We integrate the intensity over the volume of the fluorescent disk with antenna I and without antenna I_0 and plot the ratio as a function of the dye disk diameter. The antenna is a gold disk with diameter 145 nm resonant at $\lambda = 785$ nm.

6.7 RECONFIGURATION OF THE LINK VIA BEAMSTEERING

Data transmission via free space offers another important advantage besides being low-loss. The transmission channel is not tied to a certain layout as it is the case for wire and waveguide connections. This freedom brings along several benefits compared to state-of-the art fixed waveguide or wire connections:

1. The link has nanoscale footprint in two dimensions enabling very high integration density,
2. multiple crossing data links in the same layer can be realized since the radiation is not interfering,
3. the links are reconfigurable by addressing different receivers with the same transmitter via beamsteering.

The concept of *beamsteering* is well established in RF technology where *phased arrays* are used to control emission and receiving direction. Here, we bring this concept to the optical frequency range and to the nanoscale and demonstrate signal transmission with phased optical nanoantenna arrays.

6.7.1 *Phased nanoantenna array transmitter*

In Section 2.3 we have seen that the emission direction of an antenna array depends on the distance and phase difference between adjacent elements. The distance is fixed but the phase difference on the antenna array can be used to control the emission direction. Applying the idea to plasmonic antennas in the optical frequency region requires phase control on the nanoscale. In our dipole nanoantenna arrays the distance between adjacent elements is only 170 nm. From the phase calculation of the incident focused laser (see Figure 62) we observe that the phase is not constant in planes close to the focal plane. This is is schematically illustrated in the top row of Figure 79 (a). The SEM image of the transmitting five dipole array is to scale with the wavefronts of the incident beam. When we move away from the focus, the wavefronts are curved across the array and by shifting the incident beam laterally with respect to the transmitter gives external control on the phase gradient across the array. Three situations are displayed with a lateral shift of $s = -400$ nm, $s = 0$ nm, and $s = +400$ nm. The corresponding phase in the xy-plane at $z = -1$ μm from the full calculated fields (Equation 84) is shown in the bottom row of panel (a) together with the SEM micrograph. It becomes clear that the driving field reverses its phase distribution across the array by shifting the incident beam laterally from -400 nm to $+400$ nm. The induced dipole moments inherit this phase (altered negligibly by the mutual coupling), which results in a redirection of the transmitted beam. In Figure 79 (b) and (c), the fluorescence and theoretically calculated patterns are shown for the three different beam positions. A clear tilt to left and right of the radiation pattern is observed. For the fitting we use the parameters obtained from the five dipole array fit. The incident field exciting the transmitter is calculated using the rigorous theory of focusing of vectorial beams as described above taking into account the shift of the focal spot away from the center of the nanoantenna array. The parameter α is the only parameter used in the fitting. The excellent agreement with theory proves that the phasing of antenna array is accurately described with the incident driving wavefronts.

We determine the beam direction from the wide-field fluorescence images by plotting the cross section around the transmitter (similar to Figure 70) and extracting the direction of the maximum. In Figure 80 we plot φ_{max} as a function of incident beam shift. Continuous beamsteering is achieved with a remarkable range of 29°. In the theory we calculate the patterns with the fitted parameters for all the intermediate beam shifts between $s = -400$ nm to $s = +400$ nm and extract the beam direction. This is in excellent agreement with experiment.

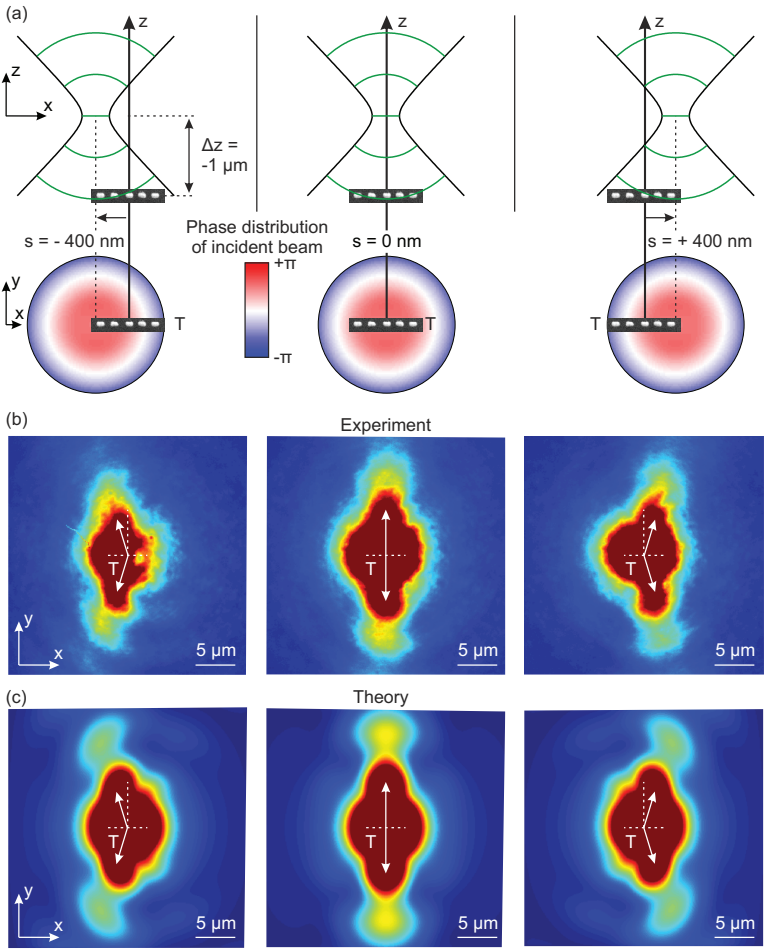

Figure 79: Beamsteering by phasing the transmitting array. (a) Top row: Wavefronts in medium (green) of a focused gaussian beam ($\lambda_o = 785$ nm) propagating along the z-direction. The beam is displaced slightly out of focus with respect to the five dipole transmitter array T and shifted laterally with a shift $s = -400$ nm (left), $s = 0$ nm (center), and $s = +400$ nm (right). Bottom row: phase distribution of the incident beam E_x in the xy-plane at $z = -1$ µm. Shifting the beam laterally tunes the phase across the array. (b) Experimental and (c) theoretical fluorescence patterns for the respective beam shifts s in (a) leading to a steering of the beam to the left or right.

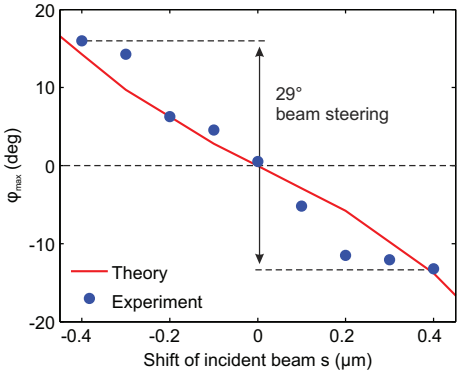

Figure 80: Beamsteering range for the five dipole phased array transmitter. The incident beam is shifted laterally across the antenna array, which leads to beamsteering. The direction of maximal intensity φ_{max} is extracted from the film measurements [compare Figure 79 (b) and (c)] and plotted as a function of the shift s. A maximal beamsteering range of 29° is measured.

6.7.2 *Communication to different receivers*

The beamsteering capability demonstrated in the previous section of our nanoantenna array is now employed to reconfigure an optical data link. Figure 81 (a) shows a SEM micrograph of the device. We fabricate plas-

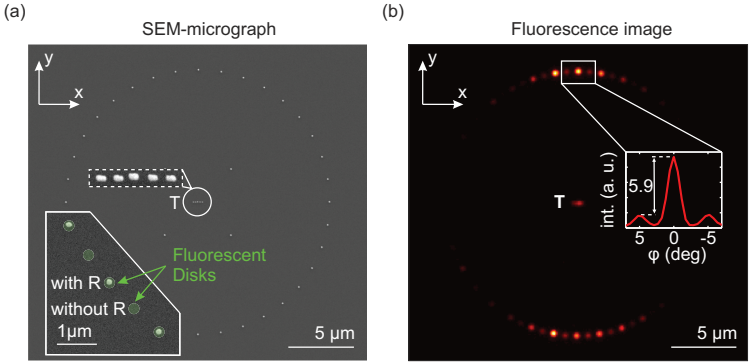

Figure 81: (a) SEM micrograph of the geometrical arrangement for the reconfigurable nanoantenna link. Fluorescent disks are positioned on a ring (radius 10 µm) around the five dipole transmitter array. Every second disk is equipped with a gold plasmonic disk serving as antenna receiver (inset). (b) Wide-field fluorescence image of the configuration for x-polarized incident light exciting the transmitter. Fluorescent disks in the direction of the radiation (y-direction) light up. The fluorescence at every second receiver is clearly enhanced due to the plasmonic antenna (5.9× enhancement).

monic disk antennas on a circle with radius 10 µm around the five dipole nanoantenna transmitter. In a second electron-beam step we position fluorescent disks on each plasmonic antenna and in between them (inset). Figure 81 (b) shows the fluorescence image when driving the antenna array with light polarized along the x-direction. The transmitted radiation is only received by receivers along the y-direction. It is apparent that a high directivity of the transmitted signal is besides higher signal transfer important to avoid cross-talk with neighboring receivers. The inset

demonstrates the enhancement due to the plasmonic receiving antenna. The signal is enhanced by a factor of 5.9.

Switching on the phasing by moving away from the focus and shifting the beam laterally allows us to steer the beam and therefore channel the power to different receivers. This is shown in Figure 82. The phasing is

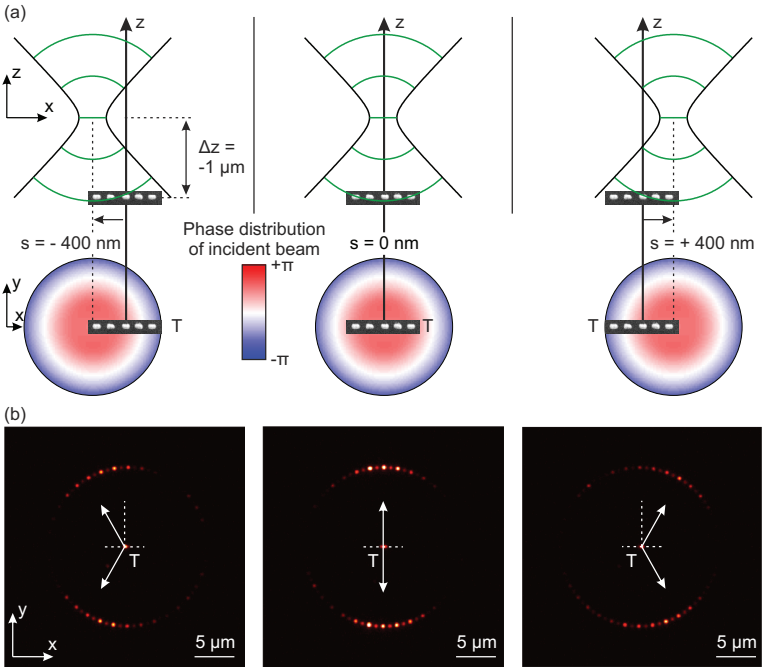

Figure 82: (a) As in Figure 79 (a) the phasing of the transmitter array T as a function of the lateral incident beam shift s is shown. (b) Luminescence images are shown of the configuration of Figure 81 (a) when adjusting the beam shift s. Different receiving antennas are addressed by steering the beam from left to right.

similar to the experiment in Figure 79 but now in the link configuration. Steering the beam to the left (right) channels the signal to left (right) receivers. This combines low-loss signal transfer at the nanoscale with the capability to reconfigure the data link.

Beamsteering can also be achieved by fixing the lateral beam position but scanning through the focus (Figure 83). In this case the sign of the radius of curvature of the wavefronts reverses, which results in the change of the phase gradient. In this experiment we left out the plasmonic receiver disks and probe the power transfer only with fluorescent dye disks. The change in quality of the fluorescence images for differ-

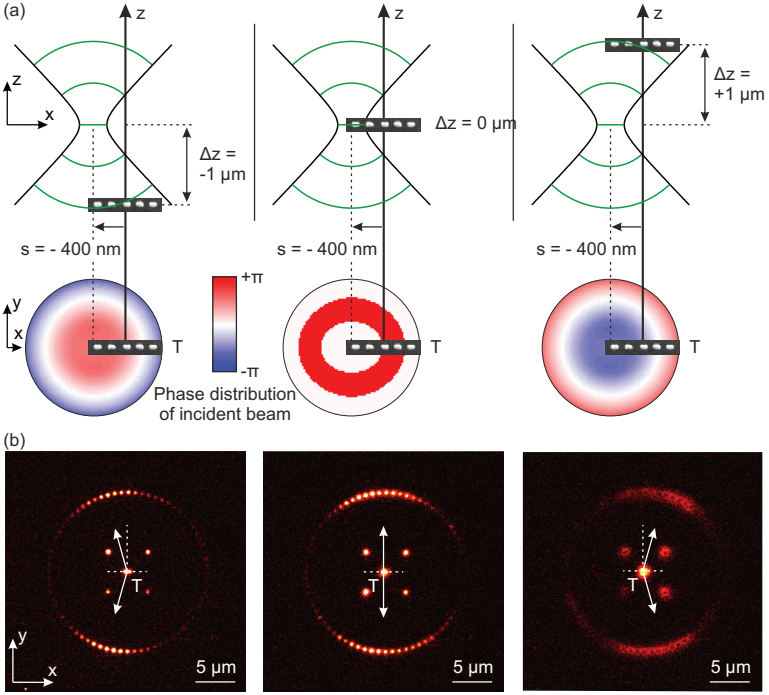

Figure 83: Top row: Wavefronts as in Figure 79 (a) are shown now scanning the incident beam through the focus and keeping the lateral position fixed at $s = -400$ nm. Bottom row: phase distribution of the incident beam E_x in the xy-plane at $z = -1$ μm (left), $z = 0$ μm (center), and $z = +1$ μm (right). As in Figure 82 (b) different receiving antennas are addressed since the radiated beam is steered from left to right when scanning the array through the focus.

ent z-values is due to aberrations of our objective. This result proves

again that the incident wavefronts are causing the beamsteering. Furthermore, it demonstrates the robustness of the reconfigurability of our data link. In future applications, wavefront shaping techniques, such as liquid crystal modulators, are easy to implement in order to make the signal transfer between two plasmonic antennas regarding direction and switching speed highly flexible.

6.8 SUMMARY AND OUTLOOK

In this chapter we have demonstrated for the first time signal transfer with plasmonic antennas. We have shown that a plasmonic nanoantenna link fulfills the requirements on high-performance data links outlined in Section 6.1. This makes them very interesting for future integration into photonic chips for intrachip and chip-to-chip optical communication.

To achieve coherent feeding of our antenna array from nanoscopic sources instead from the far-field, we envision coupling of non-linear frequency conversion nanoparticles or Raman-active molecules to the individual antenna elements. Beamsteering and directive radiation as demonstrated in our work would then work in concert with nanoscopic excitation of our antennas.

For integration with nanoscale electronic components the transmitter can be coupled to nanolasers [264–266] and the receiver to a nanoscale photodetector [88, 89], which allows electrical input and output signals. An additional degree of freedom is obtained by controlling the polarization, which would increase the possibilities to encode transmitted data even further.

7

CONCLUSION

In nano-optical engineering, plasmonics offers us unique solutions to tailor radiation, light-matter interaction, density of states, and near-field intensities.

In this thesis, we have applied plasmonics in the optical frequency regime, from the visible to the infrared region. Plasmonics provides simple and elegant approaches to design a functionality at a certain wavelength within such a broad spectral range, because the characteristic geometries of a plasmonic structure decides its functional wavelength.

In the first chapter, we used optical Yagi-Uda antennas to demonstrate directive receiving of light. Previous research focused only on the transmitting properties of optical Yagi-Uda antennas and their prospect as efficient light-sources down to the single photon level. In our work we showed that directive antennas can receive radiation from the far field and confine it to a deep sub-wavelength scale. We investigated two different antenna geometries, a single 2D Yagi-Uda nanoantenna and a 3D Yagi-Uda nanoantenna array, both resonant in the near-infrared. We used aSNOM to study the 2D Yagi-Uda antenna. This technique allows to measure simultaneously the amplitude and the phase of the plasmonic mode supported by the antenna. We determined the directive properties by recording the near-field amplitude in the vicinity of the feed element under illumination from different directions. This approach is similar to what is commonly used in the RF regime where radiation patterns of antennas are determined by measuring the load current with a far-field excitation. We showed that this measurement technique can be applied to the optical frequency range. We have furthermore determined the nature of the coupling between the individual elements and the surrounding field by the means of phase-measurements. Three different types of coupling, which are respectively capacitive, resonant and inductive,

lead to a high directivity of the optical Yagi-Uda antenna. From these experimental results, we concluded that the working principle of the 2D Yagi-Uda antenna in the optical regime can be understood in close analogy to its RF counterpart. Following the discussion on the 2D Yagi-Uda antenna, we studied the 3D Yagi-Uda antenna array. Compared to the 2D Yagi-Uda antenna, each 3D antenna has its axis directed out of the substrate plane. Therefore, the enhanced directivity is accessible when light is incident normal to the substrate. Such a 3D configuration brings along potential applications of chip-to-chip signal transfer in optical communications. Furthermore, it gives us the degree of freedom to construct a 2D array of antennas so that on the one hand, the directivity can be enhanced and on the other hand, beamsteering over a large angular range can be accomplished. By measuring the absorption when light is incident on the antenna array from two opposite directions, we confirmed the directional receiving properties of the array.

In the second chapter we employed optical antennas from the mid- to far-infrared region to enhance the signals of the vibrational bands of molecules. Our approach is based on the state-of-the-art technique SEIRA. We designed the antenna and tailored the molecule-antenna coupling carefully. We were able to position and detect molecular probes with a volume of 1.2 attoliter at specific positions with respect to the plasmonic antennas. By detuning the resonance of the antennas gradually away from the vibrational band we could identify Fano-resonances, which originated from the antenna-molecule coupling. Furthermore, we proved that the vibrational excitation is a quantitative measure for the near-field intensity. By positioning nanoscopic molecular probes with 10 nm precision, we were able to map the near-field intensity of plasmonic structures. This novel technique has a sub-wavelength resolution and can be applied in the entire IR and THz region. In addition, it has the unique capacity to assess near-fields of 3D and embedded plasmonic structures. We demonstrated near-field mapping of 3D embedded structures by coupling the vibrational bands to the dark and the bright resonators of a plasmonic EIT structure, and, with the results, analyzed the coupling effects of the different modes supported by the structure.

In the last chapter, we presented an experimental demonstration of an optical wireless nanoantenna link. It has promising applications in nanoscale integration of photonic chips. A plasmonic nanoantenna link is low-loss compared to nanoscale plasmonic waveguides since information is transferred via free space. It has a nanoscale footprint, which enables high integration density compared to technologies based on dielectric waveguides. It provides a high flexibility because multiple links with crossing paths in the same dimension can be realized with plasmonic nanoantennas, which is not possible with the state-of-the art technologies, e.g., plasmonic or dielectric waveguides. We further demonstrated a reconfigurable optical nanoantenna link based on dynamic beam steering, which is a very beneficial feature for intra- or chip-to-chip optical communication.

BIBLIOGRAPHY

[1] S. A. Maier, M. L. Brongersma, P. G. Kik, S. Meltzer, a. a. G. Requicha, H. a. Atwater, *Plasmonics-A Route to Nanoscale Optical Devices*, Advanced Materials **13**, 1501 (2001) (Cited on page 1.)

[2] E. Ozbay, *Plasmonics: merging photonics and electronics at nanoscale dimensions*, Science **311**, 189 (2006) (Cited on pages 13 and 106.)

[3] S. Lal, S. Link, N. J. Halas, *Nano-Optics from Sensing to Waveguiding.*, Nature Photonics **1**, 641 (2007) (Cited on page 15.)

[4] J. Anker, W. Hall, O. Lyandres, N. Shah, J. Zhao, R. Van Duyne, *Biosensing with plasmonic nanosensors*, Nature Materials **7**, 442 (2008)

[5] J. A. Schuller, E. S. Barnard, W. Cai, Y. C. Jun, J. S. White, M. L. Brongersma, *Plasmonics for extreme light concentration and manipulation*, Nature materials **9**, 193 (2010) (Cited on pages 12 and 106.)

[6] D. K. Gramotnev, S. I. Bozhevolnyi, *Plasmonics beyond the diffraction limit*, Nature Photonics **4**, 83 (2010)

[7] V. Giannini, A. I. Fernández-Domínguez, S. C. Heck, S. a. Maier, *Plasmonic nanoantennas: fundamentals and their use in controlling the radiative properties of nanoemitters.*, Chemical reviews **111**, 3888 (2011) (Cited on page 1.)

[8] R. Feynman, *There's plenty of room at the bottom*, Engineering and Science **23:5**, 22 (1960) (Cited on page 1.)

[9] N. Engheta, A. Salandrino, A. Alù, *Circuit Elements at Optical Frequencies: Nanoinductors, Nanocapacitors, and Nanoresistors*, Physical Review Letters **95**, (2005) (Cited on page 2.)

[10] N. Engheta, *Circuits with Light at Nanoscales: Optical Nanocircuits Inspired by Metamaterials.*, Science **317**, 1698 (2008) (Cited on page 2.)

[11] P. Mühlschlegel, H.-J. Eisler, O. J. F. Martin, B. Hecht, D. W. Pohl, *Resonant optical antennas.*, Science **308**, 1607 (2005) (Cited on pages 2 and 13.)

[12] P. Bharadwaj, B. Deutsch, L. Novotny, *Optical Antennas*, Advances in Optics and Photonics **1**, 438 (2009) (Cited on pages 13 and 15.)

[13] L. Novotny, N. van Hulst, *Antennas for light*, Nature Photonics **5**, 83 (2011) (Cited on page 15.)

[14] P. Biagioni, J.-S. Huang, B. Hecht, *Nanoantennas for visible and infrared radiation*, Reports on Progress in Physics **75**, 024402 (2012) (Cited on pages 2, 13, and 15.)

[15] L. Novotny, *The history of near-field optics*, Progress in Optics **184**, 137 (2007) (Cited on page 2.)

[16] E. H. Synge, *A suggested model for extending microscopic resolution into the ultra-microscopic region*, Philosophical Magazine Series 7 **6**, 356 (1928) (Cited on page 2.)

[17] D. W. Pohl, W. Denk, M. Lanz, *Optical stethoscopy: Image recording with resolution λ/20*, Applied Physics Letters **44**, 651 (1984) (Cited on page 2.)

[18] J. Wessel, *Surface-enhanced optical microscopy*, Journal of the Optical Society of America B **2**, 1538 (1985) (Cited on page 2.)

[19] U. Fischer, D. Pohl, *Observation of single-particle plasmons by near-field optical microscopy*, Physical Review Letters **62**, 2 (1989) (Cited on page 2.)

[20] R. D. Grober, R. J. Schoelkopf, D. E. Prober, *Optical antenna: Towards a unity efficiency near-field optical probe* **70**, 1354 (1997) (Cited on page 2.)

[21] D. W. Pohl, in *Near-Field Optics: Principles and Applications-2nd Asia-Pacific Workshop on Near Field Optics*, p. 9. Singapore: World Scientific, Beijing (1999) (Cited on page 2.)

[22] J.-J. Greffet, *Nanoantennas for Light Emission*, Science **308**, 1561 (2005) (Cited on page 2.)

[23] T. H. Taminiau, F. B. Segerink, R. J. Moerland, L. (Kobus) Kuipers, N. F. van Hulst, *Near-field driving of a optical monopole antenna*, Journal of Optics A: Pure and Applied Optics **9**, S315 (2007) (Cited on page 2.)

[24] T. H. Taminiau, F. B. Segerink, N. F. van Hulst, *A Monopole Antenna at Optical Frequencies: Single-Molecule Near-Field Measurements*, IEEE Transactions on Antennas and Propagation **55**, 3010 (2007) (Cited on page 3.)

[25] T. Taminiau, R. Moerland, F. Segerink, L. Kuipers, N. van Hulst, *[lambda]/4 Resonance of an Optical Monopole Antenna Probed by Single Molecule Fluorescence*, Nano Letters **7**, 28 (2007)

[26] R. Adato, A. A. Yanik, H. Altug, *On chip plasmonic monopole nanoantennas and circuits.*, Nano letters **11**, 5219 (2011) (Cited on pages 2 and 69.)

[27] R. Esteban, T. V. Teperik, J. J. Greffet, *Optical Patch Antennas for Single Photon Emission Using Surface Plasmon Resonances*, Physical Review Letters **104**, 026802 (2010) (Cited on pages 2, 3, and 12.)

[28] C. Belacel, B. Habert, F. Bigourdan, F. Marquier, J.-P. Hugonin, S. M. de Vasconcellos, X. Lafosse, L. Coolen, C. Schwob, C. Javaux, B. Dubertret, J.-J. Greffet, P. Senellart, a. Maitre, *Controlling spontaneous emission with plasmonic optical patch antennas.*, Nano letters **13**, 1516 (2013) (Cited on page 2.)

[29] H. F. Hofmann, T. Kosako, Y. Kadoya, *Design parameters for a nano-optical Yagi-Uda antenna*, New Journal of Physics **9**, 217 (2007) (Cited on pages 2 and 37.)

[30] J. Li, A. Salandrino, N. Engheta, *Shaping light beams in the nanometer scale: A Yagi-Uda nanoantenna in the optical domain*, Physical Review B **76**, 245403 (2007)

[31] T. H. Taminiau, F. D. Stefani, N. F. van Hulst, *Enhanced directional excitation and emission of single emitters by a nano-optical Yagi-Uda antenna*, Optics Express **16**, 10858 (2008)

[32] J. Li, A. Salandrino, N. Engheta, *Optical spectrometer at the nanoscale using optical Yagi-Uda nanoantennas*, Physical Review B **79**, 1 (2009) (Cited on page 37.)

[33] T. Kosako, Y. Kadoya, H. F. Hofmann, *Directional control of light by a nano-optical Yagi-Uda antenna*, Nature Photonics **4**, 312 (2010) (Cited on pages 38 and 137.)

[34] T. Coenen, E. J. R. Vesseur, A. Polman, A. F. Koenderink, *Directional emission from plasmonic Yagi-Uda antennas probed by angle-resolved cathodoluminescence spectroscopy.*, Nano letters **11**, 3779 (2011) (Cited on pages 38 and 106.)

[35] S. Lobanov, T. Weiss, D. Dregely, H. Giessen, N. Gippius, S. Tikhodeev, *Emission properties of an oscillating point dipole from a gold Yagi-Uda nanoantenna array*, Physical Review B **85**, 155137 (2012) (Cited on page 2.)

[36] A. E. Miroshnichenko, I. S. Maksymov, A. R. Davoyan, C. Simovski, P. Belov, Y. S. Kivshar, *An arrayed nanoantenna for broadband light emission and detection*, physica status solidi (RRL) - Rapid Research Letters **5**, 347 (2011) (Cited on page 2.)

[37] R. S. Pavlov, A. G. Curto, N. F. van Hulst, *Log-periodic optical antennas with broadband directivity*, Optics Communications **285**, 3334 (2012)

[38] D. Solís, J. Taboada, M. Araújo, F. Obelleiro, J. Rubiños López, *Design of optical wide-band log-periodic nanoantennas using surface integral equation techniques*, Optics Communications **301-302**, 61 (2013)

[39] H. Aouani, M. Rahmani, H. Šípová, V. Torres, K. Hegnerová, M. Beruete, J. Homola, M. Hong, M. Navarro-Cía, S. A. Maier, *Plasmonic Nanoantennas for Multispectral Surface-Enhanced Spectroscopies*, The Journal of Physical Chemistry C **117**, 18620 (2013) (Cited on page 2.)

[40] P. Schuck, D. Fromm, A. Sundaramurthy, G. Kino, W. Moerner, *Improving the mismatch between light and nanoscale objects with gold bowtie nanoantennas*, Physical Review Letters **94**, 17402 (2005) (Cited on pages 2 and 73.)

[41] A. Kinkhabwala, Z. Yu, S. Fan, Y. Avlasevich, K. Müllen, W. E. Moerner, *Large single-molecule fluorescence enhancements produced by a bowtie nanoantenna*, Nature Photonics **3**, 654 (2009) (Cited on pages 13 and 88.)

[42] Z. Fang, L. Fan, C. Lin, D. Zhang, A. J. Meixner, X. Zhu, *Plasmonic coupling of bow tie antennas with Ag nanowire.*, Nano letters **11**, 1676 (2011) (Cited on page 2.)

[43] J. I. Ziegler, R. F. Haglund, *Plasmonic Response of Nanoscale Spirals*, Nano Letters **10**, 100726152122045 (2010) (Cited on page 2.)

[44] B. Liu, D. Wang, C. Shi, K. Crozier, T. Yang, *Vertical optical antennas integrated with spiral ring gratings for large local electric field enhancement and directional radiation*, Optics Express **19**, 10049 (2011)

[45] K. A. Bachman, J. J. Peltzer, P. D. Flammer, T. E. Furtak, R. T. Collins, R. E. Hollingsworth, *Spiral plasmonic nanoantennas as circular polarization transmission filters*, Optics Express **20**, 1308 (2012)

[46] G. Rui, W. Chen, D. C. Abeysinghe, R. L. Nelson, Q. Zhan, *Beaming circularly polarized photons from quantum dots coupled with plasmonic spiral antenna.*, Optics express **20**, 19297 (2012)

[47] G. Rui, D. C. Abeysinghe, R. L. Nelson, Q. Zhan, *Demonstration of beam steering via dipole-coupled plasmonic spiral antenna*, Scientific Reports **3**, 1 (2013) (Cited on page 2.)

[48] L. Novotny, *Effective wavelength scaling for optical antennas*, Physical Review Letters **98**, 266802 (2007) (Cited on pages 3 and 13.)

[49] J. Dorfmüller, R. Vogelgesang, W. Khunsin, C. Rockstuhl, C. Etrich, K. Kern, *Plasmonic nanowire antennas: experiment, simulation, and theory.*, Nano letters **10**, 3596 (2010) (Cited on page 73.)

[50] T. H. Taminiau, F. D. Stefani, N. F. van Hulst, *Optical nanorod antennas modeled as cavities for dipolar emitters: evolution of sub- and super-radiant modes.*, Nano letters **11**, 1020 (2011) (Cited on page 3.)

[51] A. Alù, N. Engheta, *Tuning the scattering response of optical nanoantennas with nanocircuit loads*, Nature Photonics **2**, 307 (2008) (Cited on pages 3 and 12.)

[52] A. Alù, N. Engheta, *Wireless at the nanoscale: Optical interconnects using matched nanoantennas*, Physical Review Letters **104**, 213902 (2010) (Cited on page 3.)

[53] L. Novotny, B. Hecht, *Principles of Nano-Optics*, Cambridge University Press, Cambridge, 1st edn. (2006) (Cited on pages 10, 11, 12, 40, 41, 112, 113, 114, 115, 117, 118, 119, 121, and 122.)

[54] H. Ditlbacher, A. Hohenau, D. Wagner, U. Kreibig, M. Rogers, F. Hofer, F. Aussenegg, J. Krenn, *Silver nanowires as surface plasmon resonators*, Physical Review Letters **95**, 257403 (2005) (Cited on pages 12 and 106.)

[55] M. González, J.-C. Weeber, A.-L. Baudrion, A. Dereux, A. Stepanov, J. Krenn, E. Devaux, T. Ebbesen, *Design, near-field characterization, and modeling of 45 degree surface-plasmon Bragg mirrors*, Physical Review B **73**, 155416 (2006)

[56] R. Zia, M. Brongersma, *Surface plasmon polariton analogue to Young's double-slit experiment*, Nature Nanotechnology **2**, 426 (2007)

[57] J. Renger, R. Quidant, N. van Hulst, S. Palomba, L. Novotny, *Free-Space Excitation of Propagating Surface Plasmon Polaritons by Nonlinear Four-Wave Mixing*, Physical Review Letters **103**, 1 (2009)

[58] P. Berini, *Long-range surface plasmon polaritons*, Advances in Optics and Photonics **1**, 484 (2009) (Cited on page 106.)

[59] C.-L. Zou, F.-W. Sun, C.-H. Dong, X.-F. Ren, J.-M. Cui, X.-D. Chen, Z.-F. Han, G.-C. Guo, *Broadband integrated polarization beam splitter with surface plasmon.*, Optics letters **36**, 3630 (2011)

[60] Y. Lee, K. Hoshino, A. Alù, X. Zhang, *Tunable directive radiation of surface-plasmon diffraction gratings*, Optics Express **21**, 2748 (2013) (Cited on page 12.)

[61] W. L. Barnes, A. Dereux, T. W. Ebbesen, *Surface plasmon subwavelength optics.*, Nature **424**, 824 (2003) (Cited on page 12.)

[62] S. A. Maier, H. A. Atwater, *Plasmonics: Localization and guiding of electromagnetic energy in metal/dielectric structures*, Journal of Applied Physics **98**, 011101 (2005) (Cited on pages 12 and 15.)

[63] L. J. Sherry, S.-H. Chang, G. C. Schatz, R. P. Van Duyne, B. J. Wiley, Y. Xia, *Localized surface plasmon resonance spectroscopy of single silver nanocubes.*, Nano letters **5**, 2034 (2005) (Cited on page 12.)

[64] S. A. Maier, *Plasmonic field enhancement and SERS in the effective mode volume picture*, Optics Express **14**, 1957 (2006) (Cited on page 59.)

[65] J. Nelayah, M. Kociak, O. Stéphan, F. J. García de Abajo, M. Tencé, L. Henrard, D. Taverna, I. Pastoriza-Santos, L. M. Liz-Marzán, C. Colliex, *Mapping surface plasmons on a single metallic nanoparticle*, Nature Physics **3**, 348 (2007) (Cited on page 73.)

[66] R. Esteban, R. Vogelgesang, J. Dorfmüller, A. Dmitriev, C. Rockstuhl, C. Etrich, K. Kern, *Direct near-field optical imaging of higher order plasmonic resonances.*, Nano letters **8**, 3155 (2008) (Cited on pages 40 and 73.)

[67] T. Davis, K. Vernon, D. Gómez, *Designing Plasmonic Systems Using Optical Coupling Between Nanoparticles.*, Physical Review B **79**, 46 (2009)

[68] N. J. Halas, S. Lal, W.-S. Chang, S. Link, P. Nordlander, *Plasmons in Strongly Coupled Metallic Nanostructures.*, Chemical Reviews **111**, 3913 (2011)

[69] A. Jakab, C. Rosman, Y. Khalavka, J. Becker, A. Trügler, U. Hohenester, C. Sönnichsen, *Highly sensitive plasmonic silver nanorods.*, ACS nano **5**, 6880 (2011) (Cited on page 23.)

[70] T. J. Seok, A. Jamshidi, M. Kim, S. Dhuey, A. Lakhani, H. Choo, P. J. Schuck, S. Cabrini, A. M. Schwartzberg, J. Bokor, E. Yablonovitch, M. C. Wu, *Radiation Engineering of Optical Antennas for Maximum Field Enhancement.*, Nano letters , (2011) (Cited on page 12.)

[71] J.-S. Huang, T. Feichtner, P. Biagioni, B. Hecht, *Impedance matching and emission properties of nanoantennas in an optical nanocircuit.*, Nano letters **9**, 1897 (2009) (Cited on page 12.)

[72] M. Schnell, A. García-Etxarri, A. J. Huber, K. Crozier, J. Aizpurua, R. Hillenbrand, *Controlling the near-field oscillations of loaded plasmonic nanoantennas*, Nature Photonics **3**, 287 (2009) (Cited on page 73.)

[73] J.-J. Greffet, M. Laroche, F. Marquier, *Impedance of a Nanoantenna and a Single Quantum Emitter*, Physical Review Letters **105**, 1 (2010) (Cited on page 12.)

[74] K. Crozier, A. Sundaramurthy, G. Kino, C. Quate, *Optical antennas: resonators for local field enhancement*, Journal of Applied Physics **94**, 4632 (2003) (Cited on page 13.)

[75] R. L. Olmon, P. M. Krenz, A. C. Jones, G. D. Boreman, M. B. Raschke, *Near-field imaging of optical antenna modes in the mid-infrared.*, Optics express **16**, 20295 (2008) (Cited on page 73.)

[76] L. Novotny, *Optical antennas tuned to pitch*, Nature **455**, 2008 (2008) (Cited on page 15.)

[77] M. Agio, *Optical antennas as nanoscale resonators.*, Nanoscale **4**, 692 (2012)

[78] M. Agio, A. Alù, *Optical Antennas*, Cambridge University Press, Cambridge (2013) (Cited on pages 13, 15, 24, 25, 27, 29, 30, and 75.)

[79] M. W. Klein, C. Enkrich, M. Wegener, S. Linden, *Second-harmonic generation from magnetic metamaterials*, Science **313**, 502 (2006) (Cited on page 13.)

[80] S. Nie, S. R. Emory, *Probing single molecules and single nanoparticles by surface-enhanced raman scattering*, Science **275**, 1102 (1997) (Cited on pages 13 and 59.)

[81] P. Zijlstra, P. M. R. Paulo, M. Orrit, *Optical detection of single non-absorbing molecules using the surface plasmon resonance of a gold nanorod*, Nature nanotechnology **7**, 379 (2012)

[82] I. Ament, J. Prasad, A. Henkel, S. Schmachtel, C. Sönnichsen, *Single unlabeled protein detection on individual plasmonic nanoparticles*, Nano letters **12**, 1092 (2012) (Cited on page 13.)

[83] S. Kühn, U. Hå kanson, L. Rogobete, V. Sandoghdar, *Enhancement of Single-Molecule Fluorescence Using a Gold Nanoparticle as an Optical Nanoantenna*, Physical Review Letters **97**, 017402 (2006) (Cited on pages 13, 88, and 103.)

[84] P. Anger, P. Bharadwaj, L. Novotny, *Enhancement and quenching of single-molecule fluorescence*, Physical Review Letters **96**, 113002 (2006) (Cited on page 88.)

[85] A. G. Curto, G. Volpe, T. H. Taminiau, M. P. Kreuzer, R. Quidant, N. F. van Hulst, *Unidirectional emission of a quantum dot coupled to a nanoantenna*, Science **329**, 930 (2010) (Cited on pages 38, 40, 88, 106, and 137.)

[86] Y. C. Jun, K. C. Y. Huang, M. L. Brongersma, *Plasmonic beaming and active control over fluorescent emission*, Nature communications **2**, 283 (2011)

[87] A. G. Curto, T. H. Taminiau, G. Volpe, M. P. Kreuzer, R. Quidant, N. F. van Hulst, *Multipolar radiation of quantum emitters with nanowire optical antennas*, Nature Communications **4**, 1750 (2013) (Cited on pages 13, 88, and 106.)

[88] L. Tang, S. E. Kocabas, S. Latif, A. K. Okyay, D.-S. Ly-Gagnon, K. C. Saraswat, D. A. B. Miller, *Nanometre-scale germanium photodetector enhanced by a near-infrared dipole antenna*, Nature Photonics **2**, 226 (2008) (Cited on pages 13 and 151.)

[89] M. W. Knight, H. Sobhani, P. Nordlander, N. J. Halas, *Photodetection with active optical antennas*, Science **332**, 702 (2011) (Cited on pages 13 and 151.)

[90] A. Alduino, M. Paniccia, *Interconnects: Wiring electronics with light*, Nature Photonics **1**, 153 (2007) (Cited on pages 13 and 105.)

[91] S. A. Maier, *Plasmonics: Fundamentals and Applications*, Springer, New York, USA (2007) (Cited on pages 13, 16, 17, 18, and 23.)

[92] P. Johnson, R. Christy, *Optical Constants of the Noble Metals.*, Physical Review B **6**, 4370 (1972) (Cited on page 14.)

[93] M. Beversluis, A. Bouhelier, L. Novotny, *Continuum generation from single gold nanostructures through near-field mediated intraband transitions*, Physical Review B **68**, 115433 (2003) (Cited on page 14.)

[94] M. Brongersma, *Engineering optical nanoantennas*, Nature Photonics **2**, 4 (2008) (Cited on page 15.)

[95] Q.-H. Park, *Optical antennas and plasmonics*, Contemporary Physics **50**, 407 (2009) (Cited on page 15.)

[96] B. Luk'yanchuk, N. I. Zheludev, S. A. Maier, N. J. Halas, P. Nordlander, H. Giessen, C. T. Chong, *The Fano resonance in plasmonic nanostructures and metamaterials*, Nature Materials **9**, 707 (2010) (Cited on pages 15 and 63.)

[97] G. Mie, *Beiträge zur Optik trüber Medien, speziell kolloidaler Metalllösungen*, Annalen der Physik **25**, 377 (1908) (Cited on page 15.)

[98] C. F. Bohren, D. R. Huffman, *Absorption and Scattering of Light by Small Particles*, Wiley-VCH Verlag GmbH, Weinheim, Germany (1998) (Cited on pages 15, 18, and 20.)

[99] U. Kreibig, M. Vollmer, *Optical Properties of Metal Clusters*, Springer, Berlin (1995) (Cited on page 15.)

[100] J. D. Jackson, *Classical Electrodynamics*, John Wiley & Sons, Weinheim, Germany (1999) (Cited on page 16.)

[101] H. Kuwata, H. Tamaru, K. Esumi, K. Miyano, *Resonant light scattering from metal nanoparticles: Practical analysis beyond Rayleigh approximation*, Applied Physics Letters **83**, 4625 (2003) (Cited on page 18.)

[102] J.-S. Huang, V. Callegari, P. Geisler, C. Brüning, J. Kern, J. C. Prangsma, X. Wu, T. Feichtner, J. Ziegler, P. Weinmann, M. Kamp, A. Forchel, P. Biagioni, U. Sennhauser, B. Hecht, *Atomically flat single-crystalline gold nanostructures for plasmonic nanocircuitry*, Nature Communications **1**, 150 (2010) (Cited on page 19.)

[103] P. Kusar, C. Gruber, A. Hohenau, J. R. Krenn, *Measurement and reduction of damping in plasmonic nanowires*, Nano letters **12**, 661 (2012) (Cited on pages 19, 106, and 107.)

[104] T. G. Habteyes, S. Dhuey, E. Wood, D. Gargas, S. Cabrini, P. J. Schuck, A. P. Alivisatos, S. R. Leone, *Metallic adhesion layer induced plasmon damping and molecular linker as a nondamping alternative.*, ACS nano **6**, 5702 (2012) (Cited on page 19.)

[105] J. Zuloaga, P. Nordlander, *On the energy shift between near-field and far-field peak intensities in localized plasmon systems.*, Nano letters **11**, 1280 (2011) (Cited on page 20.)

[106] S. Zhang, D. A. Genov, Y. Wang, M. Liu, X. Zhang, *Plasmon-Induced Transparency in Metamaterials*, Physical Review Letters **101**, 047401 (2008) (Cited on page 20.)

[107] N. Liu, L. Langguth, T. Weiss, J. Kästel, M. Fleischhauer, T. Pfau, H. Giessen, *Plasmonic analogue of electromagnetically induced transparency at the Drude damping limit.*, Nature Materials **8**, 758 (2009) (Cited on page 65.)

[108] L. Novotny, *Strong coupling, energy splitting, and level crossings: A classical perspective*, American Journal of Physics **78**, 1199 (2010)

[109] R. Taubert, M. Hentschel, J. Kästel, H. Giessen, *Classical analog of electromagnetically induced absorption in plasmonics.*, Nano letters **12**, 1367 (2012) (Cited on pages 20, 66, and 97.)

[110] M. Klein, T. Tritschler, M. Wegener, S. Linden, *Lineshape of harmonic generation by metallic nanoparticles and metallic photonic crystal slabs*, Physical Review B **72**, 115113 (2005) (Cited on page 20.)

[111] M. Hentschel, T. Utikal, H. Giessen, M. Lippitz, *Quantitative modeling of the third harmonic emission spectrum of plasmonic nanoantennas.*, Nano letters **12**, 3778 (2012)

[112] B. Metzger, M. Hentschel, M. Lippitz, H. Giessen, *Third-harmonic spectroscopy and modeling of the nonlinear response of plasmonic nanoantennas.*, Optics letters **37**, 4741 (2012) (Cited on page 20.)

[113] C. Sönnichsen, *Plasmons in metal nanostructures*, Ph.D. thesis, Ludwig-Maximilians University München (2001) (Cited on page 22.)

[114] T. Utikal, *Ultrafast Nonlinear Spectroscopy of Hybrid Plasmonic Systems*, Ph.D. thesis, University of Stuttgart (2011) (Cited on page 22.)

[115] C. Sönnichsen, T. Franzl, T. Wilk, G. von Plessen, J. Feldmann, *Drastic Reduction of Plasmon Damping in Gold Nanorods*, Physical Review Letters **88**, 1 (2002) (Cited on pages 22 and 23.)

[116] N. Liu, T. Weiss, M. Mesch, L. Langguth, U. Eigenthaler, M. Hirscher, C. Sönnichsen, H. Giessen, *Planar Metamaterial Ana-*

logue of Electromagnetically Induced Transparency for Plasmonic Sensing., Nano Letters **10**, 1103 (2010) (Cited on pages 23 and 64.)

[117] C. Balanis, *Antenna theory: a review*, Proceedings of the IEEE **80**, 7 (1992) (Cited on page 26.)

[118] C. A. Balanis, *Antenna theory*, John Wiley & Sons, Hoboken, 3 edn. (2005) (Cited on pages 27 and 106.)

[119] H. Yagi, *Beam transmission of ultra short waves*, Proceedings of the IRE **16**, 715 (1928) (Cited on pages 27 and 37.)

[120] R. Taubert, D. Dregely, T. Stroucken, A. Christ, H. Giessen, *Octave-wide photonic band gap in three-dimensional plasmonic Bragg structures and limitations of radiative coupling.*, Nature communications **3**, 691 (2012) (Cited on pages 35, 73, and 97.)

[121] H. Giessen, M. Lippitz, *Directing light emission from quantum dots.*, Science (New York, N.Y.) **329**, 910 (2010) (Cited on page 38.)

[122] D. Dregely, *Optical nano-antennas*, Diploma thesis, University of Stuttgart (2009) (Cited on page 38.)

[123] J. Dorfmüller, D. Dregely, M. Esslinger, W. Khunsin, R. Vogelgesang, K. Kern, H. Giessen, *Near-field dynamics of optical Yagi-Uda nanoantennas.*, Nano letters **11**, 2819 (2011) (Cited on pages 38, 42, 73, and 106.)

[124] D. Dregely, R. Taubert, J. Dorfmüller, R. Vogelgesang, K. Kern, H. Giessen, *3D optical Yagi-Uda nanoantenna array*, Nature communications **2**, 267 (2011) (Cited on pages 38, 49, 51, 52, 53, 54, 55, 56, 73, 97, and 106.)

[125] T. Zentgraf, J. Dorfmüller, C. Rockstuhl, C. Etrich, R. Vogelgesang, K. Kern, T. Pertsch, F. Lederer, H. Giessen, *Amplitude- and phase-resolved optical near fields of split-ring-resonator-based metamaterials*, Optics Letters **33**, 848 (2008) (Cited on pages 40 and 73.)

[126] J. Dorfmüller, R. Vogelgesang, R. T. Weitz, C. Rockstuhl, C. Etrich, T. Pertsch, F. Lederer, K. Kern, *Fabry-Pérot resonances in one-dimensional plasmonic nanostructures*, Nano letters **9**, 2372 (2009) (Cited on page 40.)

[127] E. Prodan, C. Radloff, N. J. Halas, P. Nordlander, *A Hybridization Model for the Plasmon Response of Complex Nanostructures.*, Science **302**, 419 (2003) (Cited on pages 53 and 65.)

[128] M. Moskovits, *Surface-enhanced spectroscopy*, Reviews of Modern Physics **57**, 783 (1985) (Cited on page 59.)

[129] M. Fleischmann, P. Hendra, A. McQuillan, *Raman spectra of pyridine adsorbed at a silver electrode*, Chemical Physics Letters **26**, 2 (1974) (Cited on page 59.)

[130] D. Jeanmaire, R. V. Duyne, *Surface Raman spectroelectrochemistry: Part I. Heterocyclic, aromatic, and aliphatic amines adsorbed on the anodized silver electrode*, Journal of Electroanalytical Chemistry and ... **84**, (1977) (Cited on page 59.)

[131] M. Albrecht, J. Creighton, *Anomalously intense Raman spectra of pyridine at a silver electrode*, Journal of the American Chemical ... **99**, 5215 (1977) (Cited on page 59.)

[132] K. Kneipp, Y. Wang, H. Kneipp, L. Perelman, I. Itzkan, R. Dasari, M. Feld, *Single Molecule Detection Using Surface-Enhanced Raman Scattering (SERS)*, Physical Review Letters **78**, 1667 (1997) (Cited on page 59.)

[133] S. Lee, Z. Guan, H. Xu, M. Moskovits, *Surface-enhanced raman spectroscopy and nanogeometry: the plasmonic origin of SERS*, Journal of Physical Chemistry C **111**, 17985 (2007) (Cited on page 59.)

[134] F. Le, D. W. Brandl, Y. A. Urzhumov, H. Wang, J. Kundu, N. J. Halas, J. Aizpurua, P. Nordlander, *Metallic Nanoparticle Arrays: A Common Substrate for Both Surface-Enhanced Raman Scattering*

and Surface-Enhanced Infrared Absorption., ACS Nano **2**, 707 (2008) (Cited on page 59.)

[135] E. J. Smythe, M. D. Dickey, J. Bao, G. M. Whitesides, F. Capasso, *Optical antenna arrays on a fiber facet for in situ surface-enhanced Raman scattering detection.*, Nano letters **9**, 1132 (2009)

[136] A. Ahmed, R. Gordon, *Directivity enhanced Raman spectroscopy using nanoantennas.*, Nano letters **11**, 1800 (2011)

[137] W. Zhu, D. Wang, K. B. Crozier, *Direct observation of beamed Raman scattering.*, Nano letters **12**, 6235 (2012) (Cited on page 59.)

[138] A. Hartstein, J. Kirtley, J. Tsang, *Enhancement of the infrared absorption from molecular monolayers with thin metal overlayers*, Physical Review Letters **45**, 201 (1980) (Cited on page 60.)

[139] M. Osawa, M. Ikeda, *Surface-enhanced infrared absorption of p-nitrobenzoic acid deposited on silver island films: contributions of electromagnetic and chemical mechanisms*, The Journal of Physical Chemistry **95**, 9914 (1991) (Cited on page 60.)

[140] D. Enders, A. Pucci, *Surface enhanced infrared absorption of octadecanethiol on wet-chemically prepared Au nanoparticle films*, Applied Physics Letters **88**, 184104 (2006) (Cited on page 60.)

[141] H. Wang, J. Kundu, N. J. Halas, *Plasmonic nanoshell arrays combine surface-enhanced vibrational spectroscopies on a single substrate.*, Angewandte Chemie (International ed. in English) **46**, 9040 (2007) (Cited on page 60.)

[142] F. Neubrech, A. Pucci, T. Cornelius, S. Karim, A. García-Etxarri, J. Aizpurua, *Resonant plasmonic and vibrational coupling in a tailored nanoantenna for infrared detection*, Physical Review Letters **101**, 157403 (2008) (Cited on pages 60, 69, 70, 71, 72, and 87.)

[143] R. Adato, A. a. Yanik, J. J. Amsden, D. L. Kaplan, F. G. Omenetto, M. K. Hong, S. Erramilli, H. Altug, *Ultra-sensitive vibrational spec-*

troscopy of protein monolayers with plasmonic nanoantenna arrays., Proceedings of the National Academy of Sciences of the United States of America **106**, 19227 (2009) (Cited on page 69.)

[144] S. Cataldo, J. Zhao, F. Neubrech, B. Frank, C. Zhang, P. V. Braun, H. Giessen, *Hole-mask colloidal nanolithography for large-area low-cost metamaterials and antenna-assisted surface-enhanced infrared absorption substrates.*, ACS nano **6**, 979 (2012) (Cited on page 60.)

[145] U. Fano, *Effects of configuration interaction on intensities and phase shifts*, Physical Review **124**, 1866 (1961) (Cited on pages 60, 62, and 66.)

[146] H. Haken, H. C. Wolf, *Molecular Physics and Elements of Quantum Chemistry*, Springer, Berlin, 5th edn. (2003) (Cited on pages 62 and 68.)

[147] F. Siebert, P. Hildebrandt, *Vibrational Spectroscopy in Life Science*, Tutorials in Biophysics. Wiley-VCH Verlag GmbH & Co. KGaA, Weinheim, Germany (2007) (Cited on page 62.)

[148] A. Miroshnichenko, S. Flach, Y. Kivshar, *Fano resonances in nanoscale structures*, Reviews of Modern Physics **82**, 2257 (2010) (Cited on pages 62 and 63.)

[149] C. Wu, A. B. Khanikaev, R. Adato, N. Arju, A. A. Yanik, H. Altug, G. Shvets, *Fano-resonant asymmetric metamaterials for ultrasensitive spectroscopy and identification of molecular monolayers.*, Nature materials **11**, 69 (2012) (Cited on pages 63, 67, and 69.)

[150] A. Artar, A. A. Yanik, H. Altug, *Directional Double Fano Resonances in Plasmonic Hetero-Oligomers.*, Nano letters , (2011) (Cited on page 63.)

[151] a. Christ, Y. Ekinci, H. Solak, N. Gippius, S. Tikhodeev, O. Martin, *Controlling the Fano interference in a plasmonic lattice*, Physical Review B **76**, 201405 (2007) (Cited on page 63.)

[152] A. Christ, O. J. F. Martin, Y. Ekinci, N. a. Gippius, S. G. Tikhodeev, *Symmetry breaking in a plasmonic metamaterial at optical wavelength.*, Nano letters **8**, 2171 (2008)

[153] F. Hao, Y. Sonnefraud, P. Van Dorpe, S. a. Maier, N. J. Halas, P. Nordlander, *Symmetry breaking in plasmonic nanocavities: subradiant LSPR sensing and a tunable Fano resonance.*, Nano letters **8**, 3983 (2008)

[154] F. Hao, P. Nordlander, Y. Sonnefraud, P. Van Dorpe, S. a. Maier, *Tunability of subradiant dipolar and fano-type plasmon resonances in metallic ring/disk cavities: implications for nanoscale optical sensing.*, ACS nano **3**, 643 (2009)

[155] N. Verellen, Y. Sonnefraud, H. Sobhani, F. Hao, V. V. Moshchalkov, P. Van Dorpe, P. Nordlander, S. A. Maier, *Fano Resonances in Individual Coherent Plasmonic Nanocavities.*, Nano Letters **9**, 1663 (2009)

[156] Y. Sonnefraud, N. Verellen, H. Sobhani, G. A. E. Vandenbosch, V. V. Moshchalkov, P. Van Dorpe, P. Nordlander, S. A. Maier, *Experimental realization of subradiant, superradiant, and fano resonances in ring/disk plasmonic nanocavities.*, ACS nano **4**, 1664 (2010) (Cited on page 63.)

[157] J. B. Lassiter, H. Sobhani, J. A. Fan, J. Kundu, F. Capasso, P. Nordlander, N. J. Halas, *Fano Resonances in Plasmonic Nanoclusters: Geometrical and Chemical Tunability.*, Nano Letters **10**, 3184 (2010) (Cited on page 63.)

[158] M. Hentschel, M. Saliba, R. Vogelgesang, H. Giessen, A. P. Alivisatos, N. Liu, *Transition from Isolated to Collective Modes in Plasmonic Oligomers.*, Nano Letters **10**, 2721 (2010)

[159] J. A. Fan, K. Bao, C. Wu, J. Bao, R. Bardhan, N. J. Halas, V. N. Manoharan, G. Shvets, P. Nordlander, F. Capasso, *Fano-Like Interference in Self-Assembled Plasmonic Quadrumer Clusters.*, Nano Letters **10**, 4680 (2010)

[160] M. Hentschel, D. Dregely, R. Vogelgesang, H. Giessen, N. Liu, *Plasmonic Oligomers: The Role of Individual Particles in Collective Behavior.*, ACS Nano **5**, 2042 (2011)

[161] D. Dregely, M. Hentschel, H. Giessen, *Excitation and tuning of higher-order Fano resonances in plasmonic oligomer clusters.*, ACS nano **5**, 8202 (2011)

[162] M. Rahmani, B. Lukiyanchuk, B. Ng, A. T. K. G, Y. F. Liew, *Generation of pronounced Fano resonances and tuning of subwavelength spatial light distribution in plasmonic pentamers*, Optics Express **19**, 10856 (2011)

[163] M. Frimmer, T. Coenen, A. Koenderink, *Signature of a Fano resonance in a plasmonic metamolecule's local density of optical states*, Physical Review Letters **108**, 077404 (2012) (Cited on pages 63, 73, and 103.)

[164] G. Bachelier, I. Russier-Antoine, E. Benichou, C. Jonin, N. Del Fatti, F. Vallée, P.-F. Brevet, *Fano Profiles Induced by Near-Field Coupling in Heterogeneous Dimers of Gold and Silver Nanoparticles*, Physical Review Letters **101**, 197401 (2008) (Cited on page 63.)

[165] N. A. Mirin, K. Bao, P. Nordlander, *Fano Resonances in Plasmonic Nanoparticle Aggregates.*, The Journal of Physical Chemistry A **113**, 4028 (2009) (Cited on page 63.)

[166] B. Gallinet, O. Martin, *Ab initio theory of Fano resonances in plasmonic nanostructures and metamaterials*, Physical Review B **83**, 235427 (2011)

[167] B. Gallinet, O. J. F. Martin, *Influence of electromagnetic interactions on the line shape of plasmonic Fano resonances.*, ACS nano **5**, 8999 (2011)

[168] B. Gallinet, O. Martin, *Relation between near-field and far-field properties of plasmonic Fano resonances*, Opt. Express **19**, 1664 (2011)

[169] V. Giannini, Y. Francescato, H. Amrania, C. C. Phillips, S. A. Maier, *Fano resonances in nanoscale plasmonic systems: a parameter-free modeling approach.*, Nano letters **11**, 2835 (2011) (Cited on page 63.)

[170] M. Fleischhauer, A. Imamoglu, J. Marangos, *Electromagnetically induced transparency: Optics in coherent media*, Reviews of Modern Physics **77**, 633 (2005) (Cited on pages 63 and 64.)

[171] R. Taubert, *From near-field to far-field: plasmonic coupling in three-dimensional nanostructures*, Ph.D. thesis, University of Stuttgart (2012) (Cited on page 64.)

[172] A. Litvak, M. Tokman, *Electromagnetically Induced Transparency in Ensembles of Classical Oscillators*, Physical Review Letters **88**, 095003 (2002) (Cited on page 63.)

[173] C. L. Garrido Alzar, M. a. G. Martinez, P. Nussenzveig, *Classical analog of electromagnetically induced transparency*, American Journal of Physics **70**, 37 (2002) (Cited on page 63.)

[174] N. Verellen, P. Van Dorpe, C. Huang, K. Lodewijks, G. A. E. Vandenbosch, L. Lagae, V. V. Moshchalkov, *Plasmon Line Shaping Using Nanocrosses for High Sensitivity Localized Surface Plasmon Resonance Sensing*, Nano Letters , 110125111509056 (2011) (Cited on page 64.)

[175] M. Yanik, W. Suh, Z. Wang, S. Fan, *Stopping Light in a Waveguide with an All-Optical Analog of Electromagnetically Induced Transparency*, Physical Review Letters **93**, 233903 (2004) (Cited on page 64.)

[176] K. Totsuka, N. Kobayashi, M. Tomita, *Slow Light in Coupled-Resonator-Induced Transparency*, Physical Review Letters **98**, 213904 (2007) (Cited on page 64.)

[177] P. Tassin, L. Zhang, T. Koschny, E. Economou, C. Soukoulis, *Low-Loss Metamaterials Based on Classical Electromagnetically Induced Transparency*, Physical Review Letters **102**, 053901 (2009) (Cited on page 64.)

[178] P. Nordlander, C. Oubre, E. Prodan, K. Li, M. Stockman, *Plasmon Hybridization in Nanoparticle Dimers.*, Nano Letters **4**, 899 (2004) (Cited on page 65.)

[179] N. Liu, H. Guo, L. Fu, S. Kaiser, H. Schweizer, H. Giessen, *Plasmon Hybridization in Stacked Cut-Wire Metamaterials*, Advanced Materials **19**, 3628 (2007) (Cited on page 65.)

[180] E. J. Osley, C. G. Biris, P. G. Thompson, R. R. F. Jahromi, P. a. Warburton, N. C. Panoiu, *Fano Resonance Resulting from a Tunable Interaction between Molecular Vibrational Modes and a Double Continuum of a Plasmonic Metamolecule*, Physical Review Letters **110**, 087402 (2013) (Cited on page 66.)

[181] R. Adato, A. Artar, S. Erramilli, H. Altug, *Engineered absorption enhancement and induced transparency in coupled molecular and plasmonic resonator systems.*, Nano letters **13**, 2584 (2013) (Cited on page 66.)

[182] E. C. Le Ru, P. G. Etchegoin, *Principles of Surface-Enhanced Raman Spectroscopy*, Elsevier, Amsterdam, 1st edn. (2009) (Cited on page 67.)

[183] P. Alonso-González, P. Albella, M. Schnell, J. Chen, F. Huth, a. García-Etxarri, F. Casanova, F. Golmar, L. Arzubiaga, L. E. Hueso, J. Aizpurua, R. Hillenbrand, *Resolving the electromagnetic mechanism of surface-enhanced light scattering at single hot spots.*, Nature communications **3**, 684 (2012) (Cited on pages 67, 73, and 88.)

[184] J. Gooding, *The application of alkanethiol self-assembled monolayers to enzyme electrodes*, TrAC Trends in Analytical Chemistry **18**, 525 (1999) (Cited on page 69.)

[185] K. Chen, R. Adato, H. Altug, *Dual-band perfect absorber for multispectral plasmon-enhanced infrared spectroscopy.*, ACS nano **6**, 7998 (2012) (Cited on page 69.)

[186] R. Adato, H. Altug, *In-situ ultra-sensitive infrared absorption spectroscopy of biomolecule interactions in real time with plasmonic nanoantennas.*, Nature communications **4**, 2154 (2013) (Cited on page 69.)

[187] P. Ghenuche, S. Cherukulappurath, T. H. Taminiau, N. F. van Hulst, R. Quidant, *Spectroscopic mode mapping of resonant plasmon nanoantennas*, Physical Review Letters **101**, 116805 (2008) (Cited on page 73.)

[188] G. Boudarham, N. Feth, V. Myroshnychenko, S. Linden, J. García de Abajo, M. Wegener, M. Kociak, *Spectral imaging of individual split-ring resonators*, Physical Review Letters **105**, 255501 (2010) (Cited on page 73.)

[189] E. J. R. Vesseur, R. de Waele, M. Kuttge, A. Polman, *Direct observation of plasmonic modes in au nanowires using high-resolution cathodoluminescence spectroscopy.*, Nano letters **7**, 2843 (2007) (Cited on page 73.)

[190] M. Cinchetti, A. Gloskovskii, S. Nepjiko, G. Schönhense, H. Rochholz, M. Kreiter, *Photoemission electron microscopy as a tool for the investigation of optical near fields*, Physical Review Letters **95**, 047601 (2005) (Cited on page 73.)

[191] L. Douillard, F. Charra, Z. Korczak, R. Bachelot, S. Kostcheev, G. Lerondel, P.-M. Adam, P. Royer, *Short range plasmon resonators probed by photoemission electron microscopy.*, Nano letters **8**, 935 (2008) (Cited on page 73.)

[192] R. Vogelgesang, J. Dorfmüller, R. Esteban, R. T. Weitz, A. Dmitriev, K. Kern, *Plasmonic nanostructures in aperture-less scanning near-field optical microscopy (aSNOM)*, Physica Status Solidi (B) **245**, 2255 (2008) (Cited on page 73.)

[193] M. Schnell, A. Garcia-Etxarri, A. J. Huber, K. B. Crozier, A. Borisov, J. Aizpurua, R. Hillenbrand, *Amplitude- and phase-resolved near-field*

mapping of infrared antenna modes by transmission-mode scattering-type near-field microscopy, The Journal of Physical Chemistry C **114**, 7341 (2010)

[194] M. Schnell, P. Alonso-González, L. Arzubiaga, F. Casanova, L. E. Hueso, A. Chuvilin, R. Hillenbrand, *Nanofocusing of mid-infrared energy with tapered transmission lines*, Nature Photonics , 1 (2011) (Cited on page 73.)

[195] J. K. Gansel, M. Thiel, M. S. Rill, M. Decker, K. Bade, V. Saile, G. von Freymann, S. Linden, M. Wegener, *Gold helix photonic metamaterial as broadband circular polarizer.*, Science **325**, 1513 (2009) (Cited on page 73.)

[196] M. Liu, T.-W. Lee, S. Gray, P. Guyot-Sionnest, M. Pelton, *Excitation of Dark Plasmons in Metal Nanoparticles by a Localized Emitter*, Physical Review Letters **102**, 1 (2009) (Cited on page 73.)

[197] R. Ameling, H. Giessen, *Cavity plasmonics: large normal mode splitting of electric and magnetic particle plasmons induced by a photonic microcavity.*, Nano letters **10**, 4394 (2010) (Cited on page 73.)

[198] R. Ameling, L. Langguth, M. Hentschel, M. Mesch, P. V. Braun, H. Giessen, *Cavity-enhanced localized plasmon resonance sensing*, Applied Physics Letters **97**, 253116 (2010)

[199] R. Ameling, D. Dregely, H. Giessen, *Strong coupling of localized and surface plasmons to microcavity modes.*, Optics letters **36**, 2218 (2011) (Cited on page 73.)

[200] Y. Alaverdyan, N. Vamivakas, J. Barnes, C. Lebouteiller, J. Hare, M. Atatüre, *Spectral tunability of a plasmonic antenna with a dielectric nanocrystal*, Optics Express **19**, 18175 (2011) (Cited on page 74.)

[201] M. Piliarik, P. Kvasnička, N. Galler, J. R. Krenn, J. Homola, *Local refractive index sensitivity of plasmonic nanoparticles.*, Optics express **19**, 9213 (2011) (Cited on page 74.)

[202] C. Hubert, A. Rumyantseva, G. Lerondel, J. Grand, S. Kostcheev, L. Billot, A. Vial, R. Bachelot, P. Royer, S.-h. Chang, S. K. Gray, G. P. Wiederrecht, G. C. Schatz, *Near-field photochemical imaging of noble metal nanostructures.*, Nano letters **5**, 615 (2005) (Cited on page 74.)

[203] G. Volpe, M. Noack, S. S. Aćimović, C. Reinhardt, R. Quidant, *Near-field mapping of plasmonic antennas by multiphoton absorption in poly(methyl methacrylate).*, Nano letters **12**, 4864 (2012) (Cited on page 74.)

[204] P. H. C. Eilers, *A perfect smoother.*, Analytical chemistry **75**, 3631 (2003) (Cited on page 75.)

[205] D. Dregely, F. Neubrech, H. Duan, R. Vogelgesang, H. Giessen, *Vibrational near-field mapping of planar and buried three-dimensional plasmonic nanostructures.*, Nature communications **4**, 2237 (2013) (Cited on pages 75, 81, 82, 83, 85, 92, 95, 96, 99, and 100.)

[206] G. R. Fowles, *Introduction to Modern Optics*, Dover, New York, USA, 2nd editio edn. (1989) (Cited on page 76.)

[207] D. L. Olynick, B. Cord, A. Schipotinin, D. F. Ogletree, P. J. Schuck, *Electron-beam exposure mechanisms in hydrogen silsesquioxane investigated by vibrational spectroscopy and in situ electron-beam-induced desorption*, Journal of Vacuum Science & Technology B: Microelectronics and Nanometer Structures **28**, 581 (2010) (Cited on pages 77 and 79.)

[208] L. V. Brown, K. Zhao, N. King, H. Sobhani, P. Nordlander, N. J. Halas, *Surface-enhanced infrared absorption using individual cross antennas tailored to chemical moieties*, Journal of the American Chemical Society **135**, 3688 (2013) (Cited on page 87.)

[209] D. Dregely, K. Lindfors, J. Dorfmüller, M. Hentschel, M. Becker, J. Wrachtrup, M. Lippitz, R. Vogelgesang, H. Giessen, *Plasmonic antennas, positioning, and coupling of individual quantum systems*, physica status solidi (b) **249**, 666 (2012) (Cited on page 88.)

[210] S. Schietinger, M. Barth, T. Aichele, O. Benson, *Plasmon-enhanced single photon emission from a nanoassembled metal-diamond hybrid structure at room temperature.*, Nano letters **9**, 1694 (2009) (Cited on page 88.)

[211] R. Kolesov, B. Grotz, G. Balasubramanian, R. J. Stöhr, A. A. L. Nicolet, P. R. Hemmer, F. Jelezko, J. Wrachtrup, *Wave-particle duality of single surface plasmon polaritons*, Nature Physics **5**, 470 (2009) (Cited on page 106.)

[212] M. Barth, S. Schietinger, T. Schröder, T. Aichele, O. Benson, *Controlled coupling of NV defect centers to plasmonic and photonic nanostructures*, Journal of Luminescence **130**, 1628 (2010)

[213] A. W. Schell, G. Kewes, T. Hanke, A. Leitenstorfer, R. Bratschitsch, O. Benson, T. Aichele, *Single defect centers in diamond nanocrystals as quantum probes for plasmonic nanostructures*, Optics Express **19**, 7914 (2011)

[214] K. Beha, H. Fedder, M. Wolfer, M. C. Becker, P. Siyushev, M. Jamali, A. Batalov, C. Hinz, J. Hees, L. Kirste, H. Obloh, E. Gheeraert, B. Naydenov, I. Jakobi, F. Dolde, S. Pezzagna, D. Twittchen, M. Markham, D. Dregely, H. Giessen, J. Meijer, F. Jelezko, C. E. Nebel, R. Bratschitsch, A. Leitenstorfer, J. Wrachtrup, *Diamond nanophotonics*, Beilstein Journal of Nanotechnology **3**, 895 (2012) (Cited on page 88.)

[215] P. Bharadwaj, L. Novotny, *Spectral dependence of single molecule fluorescence enhancement.*, Optics express **15**, 14266 (2007) (Cited on page 88.)

[216] M. Celebrano, R. Lettow, P. Kukura, M. Agio, a. Renn, S. Götzinger, V. Sandoghdar, *Efficient coupling of single photons to single plasmons.*, Optics express **18**, 13829 (2010) (Cited on page 88.)

[217] a. J. Huber, F. Keilmann, J. Wittborn, J. Aizpurua, R. Hillenbrand, *Terahertz near-field nanoscopy of mobile carriers in single semiconductor nanodevices.*, Nano letters **8**, 3766 (2008) (Cited on page 88.)

[218] J. M. Stiegler, Y. Abate, A. Cvitkovic, Y. E. Romanyuk, A. J. Huber, S. R. Leone, R. Hillenbrand, *Nanoscale infrared absorption spectroscopy of individual nanoparticles enabled by scattering-type near-field microscopy.*, ACS nano **5**, 6494 (2011)

[219] F. Huth, A. Govyadinov, S. Amarie, W. Nuansing, F. Keilmann, R. Hillenbrand, *Nano-FTIR absorption spectroscopy of molecular fingerprints at 20 nm spatial resolution.*, Nano letters **12**, 3973 (2012)

[220] J. Mattis Hoffmann, B. Hauer, T. Taubner, *Antenna-enhanced infrared near-field nanospectroscopy of a polymer*, Applied Physics Letters **101**, 193105 (2012)

[221] X. G. Xu, M. Rang, I. M. Craig, M. B. Raschke, *Pushing the sample-size limit of infrared vibrational nanospectroscopy: From monolayer toward single molecule sensitivity*, The Journal of Physical Chemistry Letters **3**, 1836 (2012)

[222] X. G. Xu, M. B. Raschke, *Near-field Infrared Vibrational Dynamics and Tip-Enhanced Decoherence.*, Nano letters , (2013) (Cited on page 88.)

[223] R. Stöckle, Y. Suh, V. Deckert, R. Zenobi, *Nanoscale chemical analysis by tip-enhanced Raman spectroscopy*, Chemical Physics Letters **318**, 131 (2000) (Cited on page 88.)

[224] E. Bailo, V. Deckert, *Tip-enhanced Raman scattering.*, Chemical Society reviews **37**, 921 (2008)

[225] M. D. Sonntag, J. M. Klingsporn, L. K. Garibay, J. M. Roberts, J. a. Dieringer, T. Seideman, K. a. Scheidt, L. Jensen, G. C. Schatz, R. P. Van Duyne, *Single-Molecule Tip-Enhanced Raman Spectroscopy*, The Journal of Physical Chemistry C **116**, 478 (2012) (Cited on page 88.)

[226] H. Duan, V. R. Manfrinato, J. K. W. Yang, D. Winston, B. M. Cord, K. K. Berggren, *Metrology for electron-beam lithography and resist contrast at the sub-10 nm scale*, Journal of Vacuum Science & Technology B: Microelectronics and Nanometer Structures **28**, C6H11 (2010) (Cited on page 94.)

[227] H. Duan, D. Winston, J. K. W. Yang, B. M. Cord, V. R. Manfrinato, K. K. Berggren, *Sub-10-nm half-pitch electron-beam lithography by using poly(methyl methacrylate) as a negative resist*, Journal of Vacuum Science & Technology B: Microelectronics and Nanometer Structures **28**, C6C58 (2010)

[228] H. Duan, H. Hu, K. Kumar, Z. Shen, J. K. W. Yang, *Direct and reliable patterning of plasmonic nanostructures with sub-10-nm gaps.*, ACS nano **5**, 7593 (2011) (Cited on page 94.)

[229] M. Thiel, M. Decker, M. Deubel, M. Wegener, S. Linden, G. von Freymann, *Polarization Stop Bands in Chiral Polymeric Three-Dimensional Photonic Crystals*, Advanced Materials **19**, 207 (2007) (Cited on page 97.)

[230] E. Plum, J. Zhou, J. Dong, V. Fedotov, T. Koschny, C. Soukoulis, N. Zheludev, *Metamaterial with negative index due to chirality*, Physical Review B **79**, 035407 (2009)

[231] S. Zhang, Y.-S. Park, J. Li, X. Lu, W. Zhang, X. Zhang, *Negative Refractive Index in Chiral Metamaterials*, Physical Review Letters **102**, 023901 (2009)

[232] A. Guerrero-Martínez, J. L. Alonso-Gómez, B. Auguié, M. M. Cid, L. M. Liz-Marzán, *From individual to collective chirality in metal nanoparticles*, Nano Today **6**, 381 (2011)

[233] A. Guerrero-Martínez, B. Auguié, J. L. Alonso-Gómez, Z. Džolić, S. Gómez-Graña, M. Žinić, M. M. Cid, L. M. Liz-Marzán, *Intense optical activity from three-dimensional chiral ordering of plasmonic nanoantennas.*, Angewandte Chemie **50**, 5499 (2011)

[234] M. Schäferling, D. Dregely, M. Hentschel, H. Giessen, *Tailoring Enhanced Optical Chirality: Design Principles for Chiral Plasmonic Nanostructures*, Physical Review X **2**, 031010 (2012)

[235] A. Kuzyk, R. Schreiber, Z. Fan, G. Pardatscher, E.-M. Roller, A. Högele, F. C. Simmel, A. O. Govorov, T. Liedl, *DNA-based*

self-assembly of chiral plasmonic nanostructures with tailored optical response, Nature **483**, 311 (2012)

[236] M. Hentschel, L. Wu, M. Schäferling, P. Bai, E. P. Li, H. Giessen, *Optical properties of chiral three-dimensional plasmonic oligomers at the onset of charge-transfer plasmons.*, ACS nano **6**, 10355 (2012)

[237] M. Hentschel, M. Schäferling, T. Weiss, N. Liu, H. Giessen, *Three-dimensional chiral plasmonic oligomers.*, Nano letters **12**, 2542 (2012)

[238] M. Hentschel, M. Schäferling, B. Metzger, H. Giessen, *Plasmonic diastereomers: adding up chiral centers.*, Nano letters **13**, 600 (2013) (Cited on page 97.)

[239] R. Krutokhvostov, A. A. Govyadinov, J. M. Stiegler, F. Huth, A. Chuvilin, P. S. Carney, R. Hillenbrand, *Enhanced resolution in subsurface near-field optical microscopy*, Optics Express **20**, 593 (2011) (Cited on page 98.)

[240] M. Frimmer, Y. Chen, A. Koenderink, *Scanning emitter lifetime imaging microscopy for spontaneous emission control*, Physical Review Letters **107**, 123602 (2011) (Cited on page 103.)

[241] R. Sapienza, T. Coenen, J. Renger, M. Kuttge, N. F. van Hulst, A. Polman, *Deep-subwavelength imaging of the modal dispersion of light.*, Nature materials **11**, 781 (2012) (Cited on page 103.)

[242] J. Hwang, M. Pototschnig, R. Lettow, G. Zumofen, A. Renn, S. Götzinger, V. Sandoghdar, *A single-molecule optical transistor.*, Nature **460**, 76 (2009) (Cited on page 105.)

[243] M. Geiselmann, R. Marty, F. J. García de Abajo, R. Quidant, *Fast optical modulation of the fluorescence from a single nitrogen-vacancy centre*, Nature Physics , 1 (2013) (Cited on page 105.)

[244] A. V. Akimov, A. Mukherjee, C. L. Yu, D. E. Chang, a. S. Zibrov, P. R. Hemmer, H. Park, M. D. Lukin, *Generation of single optical plasmons in metallic nanowires coupled to quantum dots*, Nature **450**, 402 (2007) (Cited on page 106.)

[245] Y. Fedutik, V. Temnov, O. Schöps, U. Woggon, M. Artemyev, *Exciton-plasmon-photon conversion in plasmonic nanostructures*, Physical Review Letters **99**, 136802 (2007)

[246] Y. Fang, Z. Li, Y. Huang, S. Zhang, P. Nordlander, N. J. Halas, H. Xu, *Branched silver nanowires as controllable plasmon routers*, Nano letters **10**, 1950 (2010)

[247] P. Berini, I. De Leon, *Surface plasmon-polariton amplifiers and lasers*, Nature Photonics **6**, 16 (2011) (Cited on page 106.)

[248] S. A. Maier, P. G. Kik, H. A. Atwater, S. Meltzer, E. Harel, B. E. Koel, A. A. G. Requicha, *Local detection of electromagnetic energy transport below the diffraction limit in metal nanoparticle plasmon waveguides*, Nature Materials **2**, 229 (2003) (Cited on page 106.)

[249] R. de Waele, A. Koenderink, A. Polman, *Tunable nanoscale localization of energy on plasmon particle arrays*, Nano Letters **7**, 2004 (2007)

[250] A. F. Koenderink, *Plasmon nanoparticle array waveguides for single photon and single plasmon sources.*, Nano letters **9**, 4228 (2009) (Cited on page 106.)

[251] J. Wenger, D. Gérard, J. Dintinger, O. Mahboub, N. Bonod, E. Popov, T. W. Ebbesen, H. Rigneault, *Emission and excitation contributions to enhanced single molecule fluorescence by gold nanometric apertures*, Optics Express **16**, 3008 (2008) (Cited on page 106.)

[252] H. Aouani, O. Mahboub, E. Devaux, H. Rigneault, T. W. Ebbesen, J. Wenger, *Plasmonic antennas for directional sorting of fluorescence emission.*, Nano letters **11**, 2400 (2011)

[253] H. Aouani, O. Mahboub, N. Bonod, E. Devaux, E. Popov, H. Rigneault, T. W. Ebbesen, J. Wenger, *Bright unidirectional fluorescence emission of molecules in a nanoaperture with plasmonic corrugations.*, Nano letters **11**, 637 (2011) (Cited on page 106.)

[254] J. Takahara, S. Yamagishi, H. Taki, A. Morimoto, T. Kobayashi, *Guiding of a one-dimensional optical beam with nanometer diameter*, Optics letters **22**, 475 (1997) (Cited on page 108.)

[255] H. Ditlbacher, J. R. Krenn, N. Felidj, B. Lamprecht, G. Schider, M. Salerno, a. Leitner, F. R. Aussenegg, *Fluorescence imaging of surface plasmon fields*, Applied Physics Letters **80**, 404 (2002) (Cited on page 109.)

[256] D. Solis, W.-S. Chang, B. P. Khanal, K. Bao, P. Nordlander, E. R. Zubarev, S. Link, *Bleach-Imaged Plasmon Propagation (BlIPP) in Single Gold Nanowires.*, Nano letters , 3482 (2010)

[257] T. Zentgraf, Y. Liu, M. H. Mikkelsen, J. Valentine, X. Zhang, *Plasmonic Luneburg and Eaton lenses.*, Nature nanotechnology **6**, 151 (2011)

[258] A. Paul, D. Solis, K. Bao, W.-S. Chang, S. Nauert, L. Vidgerman, E. R. Zubarev, P. Nordlander, S. Link, *Identification of higher order long-propagation-length surface plasmon polariton modes in chemically prepared gold nanowires.*, ACS nano **6**, 8105 (2012) (Cited on page 109.)

[259] T. Christ, F. Kulzer, P. Bordat, T. Basché, *Watching the Photo-Oxidation of a Single Aromatic Hydrocarbon Molecule*, Angewandte Chemie International Edition **40**, 4192 (2001) (Cited on page 121.)

[260] B. T. Draine, P. J. Flatau, *Discrete-dipole approximation for scattering calculations*, Journal of the Optical Society of America A **11**, 1491 (1994) (Cited on page 123.)

[261] Y. H. Fu, A. I. Kuznetsov, A. E. Miroshnichenko, Y. F. Yu, B. Luk'yanchuk, *Directional visible light scattering by silicon nanoparticles.*, Nature communications **4**, 1527 (2013) (Cited on page 137.)

[262] S. Person, M. Jain, Z. Lapin, J. J. Sáenz, G. Wicks, L. Novotny, *Demonstration of zero optical backscattering from single nanoparticles.*, Nano letters **13**, 1806 (2013)

[263] D. Vercruysse, Y. Sonnefraud, N. Verellen, F. B. Fuchs, G. Di Martino, L. Lagae, V. V. Moshchalkov, S. a. Maier, P. Van Dorpe, *Unidirectional side scattering of light by a single-element nanoantenna.*, Nano letters **13**, 3843 (2013) (Cited on page 137.)

[264] M. T. Hill, Y.-S. Oei, B. Smalbrugge, Y. Zhu, T. de Vries, P. J. van Veldhoven, F. W. M. van Otten, T. J. Eijkemans, J. P. Turkiewicz, H. de Waardt, E. J. Geluk, S.-H. Kwon, Y.-H. Lee, R. Nötzel, M. K. Smit, *Lasing in metallic-coated nanocavities*, Nature Photonics **1**, 589 (2007) (Cited on page 151.)

[265] R. F. Oulton, V. J. Sorger, T. Zentgraf, R.-M. Ma, C. Gladden, L. Dai, G. Bartal, X. Zhang, *Plasmon lasers at deep subwavelength scale.*, Nature **461**, 629 (2009)

[266] Y.-J. Lu, J. Kim, H.-Y. Chen, C. Wu, N. Dabidian, C. E. Sanders, C.-Y. Wang, M.-Y. Lu, B.-H. Li, X. Qiu, W.-H. Chang, L.-J. Chen, G. Shvets, C.-K. Shih, S. Gwo, *Plasmonic nanolaser using epitaxially grown silver film.*, Science **337**, 450 (2012) (Cited on page 151.)

ACKNOWLEDGMENTS

Many people contributed to the progress of my PhD thesis and I am very thankful to all of them.

I would like to thank *Prof. Harald Giessen* for supervising my thesis. I am especially thankful to him for giving me the necessary freedom in my research projects and for always being encouraging and motivating. I am furthermore grateful for the numerous stimulating scientific discussions, interesting ideas and all the support I received during these years.

I would like to thank *Prof. Peter Michler*, *Prof. Carsten Sönnichsen* and *Prof. Hans-Rainer Trebin* for being so kind to be the examination committee and for all their support.

Many thanks to *Christine von Rekowski* for solving all kind of administrative problems helping me to focus on my thesis.

I am very thankful to *Klas Lindfors* for all his guidance, long-lasting discussions and phone calls and the fun in the lab and in the cleanroom.

I would like to thank *Prof. Jürgen Weiß* for giving me the access to the cleanroom facilities at the Max-Planck-Institute and *Thomas Reindl* and *Monika Ubl* for helping me with all kind of nanofabrication issues.

I would like to thank all my colleagues at the 4th Physics Institute and the Max Planck Institute who are the reason of the very nice and pleasant working environment.

I owe special thanks to *Jessie Chin*, *Klas Lindfors*, *Bernd Metzger*, and *Frank Neubrech* for proof-reading my thesis and their valuable input, comments and corrections.

I would like to thank *Sven Hein* for the visual support with Pov-Ray.

Many successful ideas would have not been pursued further or would have just been abandoned if I did not have idea-creating and problem-solving discussions with *Jens Dorfmüller*, *Klas Lindfors*, *Bernd Metzger*, *Mario Hentschel*, *Frank Neubrech*, and *Richard Taubert*. Thank you very much! I am also very grateful for working together with you on the successful research projects that evolved out of these ideas.

Besides the cleanroom and the lab, I spent a large amount of time in the office which I always enjoyed because of my office mates *Dominik Flöss* and *Richard Taubert*. Thank you!

Not everything was about work during my PhD thesis and I especially would like to thank *Ralf Ameling*, *Timo Gissibl*, *Mario Hentschel*, *Martin Mesch*, *Bernd Metzger*, *Martin Schäferling*, *Richard Taubert* and *Marius Vieweg* for all the fun we had during our extracurricular activities: running, biking, skiing, hiking, Christmas-market, soccer watching, Columbus, card games, macarons and scones on Sundays at Mario's place, and so on.

Ich möchte mich bei meinen Eltern und meiner Schwester bedanken für 29 Jahre Unterstützung, ohne die diese Arbeit nicht entstanden wäre.

Finally, thank you *Jessie* for all your contribution to our common life project! Without you, this and many many other things would not be possible!

CURRICULUM VITÆ

NAME	Daniel Drégely
BORN	4 July, 1984 in Regensburg
ADDRESS	Dornhaldenstr. 20, 70199 Stuttgart, Germany
PHONE	+49 71168564961
MAIL	d.dregely@physik.uni-stuttgart.de

1994–2003	Abitur: Karl-von-Closen-Gymnasium, Eggenfelden, Germany
2003–2004	Civil service: Kreiskrankenhaus, Eggenfelden, Germany
2004–2006	Vordiplom in physics: University of Stuttgart, Germany
2006–2009	Double-degree program T.I.M.E. *Diplom in physics*: University of Stuttgart, Germany Diploma Thesis: "Optical Nanoantennas" Advisor: Prof. Dr. H. Giessen *Ingénieur École Centrale Paris*: École Centrale Paris, France
2009–2014	*PhD in Physics*: University of Stuttgart, Germany Thesis: "Optical Antennas: Nanoscale Radiation Engineering and Enhanced Light-Matter Interaction" Advisor: Prof. Dr. H. Giessen
SINCE 2012	Peer review for Optics Express, Optics Letters, physica status solidi (RRL)

COLOPHON

This thesis was typeset using the typographical look-and-feel `classicthesis` developed by André Miede. The style was inspired by Robert Bringhurst's seminal book on typography "*The Elements of Typographic Style*". `classicthesis` is available for both LaTeX and LyX:

`http://code.google.com/p/classicthesis/`